AD NUMBER
AD867179
LIMITATION CHANGES

TO:

Approved for public release; distribution is unlimited.

FROM:

Distribution authorized to U.S. Gov't. agencies and their contractors; Critical Technology; JAN 1970. Other requests shall be referred to U.S. Army Aviation Materiel Laboratories, Fort Eustis, VA 23604. This document contains export-controlled technical data.

AUTHORITY

USAAMRDL ltr, 23 Jun 1971

AD

AD 867179

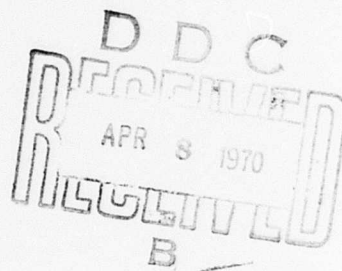# USAAVLABS TECHNICAL REPORT 69-91

AN INVESTIGATION OF TURBINE BLADE/DISK ATTACHMENT METHODS FOR SMALL, COOLED GAS TURBINES

By

J. L. Helmbrecht
R. F. Kirby
F. Weber

January 1970

U. S. ARMY AVIATION MATERIEL LABORATORIES
FORT EUSTIS, VIRGINIA

CONTRACT DAAJ02-68-C-0119
THE AIRESEARCH MANUFACTURING
COMPANY OF ARIZONA
PHOENIX, ARIZONA

D D C
RECEIVED
APR 8 1970
RECEIVED
B

Disclaimers

The findings in this report are not to be construed as an official Department of the Army position unless so designated by other authorized documents.

When Government drawings, specifications, or other data are used for any purpose other than in connection with a definitely related Government procurement operation, the United States Government thereby incurs no responsibility nor any obligation whatsoever; and the fact that the Government may have formulated, furnished, or in any way supplied the said drawings, specifications, or other data is not to be regarded by implication or otherwise as in any manner licensing the holder or any other person or corporation, or conveying any rights or permission, to manufacture, use, or sell any patented invention that may in any way be related thereto.

Trade names cited in this report do not constitute an official endorsement or approval of the use of such commercial hardware or software.

Disposition Instructions

Destroy this report when no longer needed. Do not return it to the originator.

The research described herein was conducted by the AiResearch Manufacturing Company of Arizona under the terms of Contract DAAJ02-68-C-0119. The work was performed under the technical management of Mr Edward T. Johnson, Propulsion Division, U.S. Army Aviation Materiel Laboratories.

The object of this research effort was the investigation, through analytical studies and experimental testing, of several blade-to-disk attachment concepts and airfoil shell-to-strut attachment concepts to determine the optimum concept for use on future small, high-temperature turbine rotors.

Appropriate technical personnel of the U.S. Army Aviation Materiel Laboratories have reviewed this report and concur with the conclusions contained herein.

The findings and recommendations outlined herein will be taken into consideration in the planning of future axial turbine programs.

AN INVESTIGATION OF TURBINE BLADE/DISK ATTACHMENT
METHODS FOR SMALL, COOLED GAS TURBINES

Final Report

By

J. L. Helmbrecht
R. F. Kirby
F. Weber

Prepared by

The AiResearch Manufacturing
Company of Arizona
Phoenix, Arizona

for

U.S. ARMY AVIATION MATERIEL LABORATORIES
FORT EUSTIS, VIRGINIA

ABSTRACT

This report describes the analytical, experimental, and developmental efforts that were conducted to design, fabricate, test, and evaluate turbine-rotor blade to rotor disk (blade/disk) attachment methods for an air-cooled turbine rotor in a small gas turbine engine. This investigation was launched because the combination of factors that are necessary to satisfy the design requirements of a small cooled gas turbine has made it increasingly difficult to utilize conventional blade attachment means. Specifically, the program was directed toward achieving a suitable attachment method for an axial turbine with an inlet temperature of 2400°F, an airflow rate of 4.0 lb/sec, a tip speed of 1500 ft/sec, and matched to a compressor having a 10:1 pressure ratio.

Detailed aerothermodynamic design activities were conducted to determine a turbine design that would provide optimum specific fuel consumption (SFC) and specific horsepower (sp hp). The design included an optimization study to obtain the best compromise of turbine efficiency, cooling geometry, blade and disk stress effects, and fabrication considerations.

Detailed mechanical design activities were conducted in parallel with fabrication technology development efforts to establish the materials, designs, joining methods, and fabrication techniques necessary to determine feasible means of blade/disk attachment. Results of these activities showed that diffusion-bonding, brazing, and electron-beam-welding blade/disk attachment methods possess the greatest potential for application in the subject turbine design.

A secondary purpose of the mechanical design and fabrication development activities was to study the feasibility of developing the strut-supported sheet metal blade (shell/strut attachment) that was revealed by the aerodynamic optimization study to be the most effective blade cooling configuration. Full evaluation of the shell/strut attachment was beyond the scope of this program; however, it was determined that both diffusion-bonding and cast-bonding concepts of joining could be considered as feasible methods to develop for the purpose of shell/strut attachment.

A final fabrication and test activity was conducted to complete evaluations of the three blade/disk attachment methods. Final specimens were designed, fabricated, inspected, and subjected to tensile, stress-rupture, and low-cycle fatigue testing at 1200°F.

Evaluation of the final specimen test results revealed that (a) the diffusion-bonding method of joining was unsatisfactory for blade/disk attachment due to insufficient joint strength, (b) the brazing method of joining produced a joint strength approaching design requirements and could be considered as a candidate method for rotational test evaluation, and (c) the electron-beam-welding method of joining produced a joint strength that exceeded design requirements. Further evaluation will be necessary to resolve microcracking in the weld joint before rotational test evaluations can be considered.

FOREWORD

This final report describes a turbine blade/disk fabrication
investigation that was conducted in fulfillment of Contract
DAAJ02-68-C-0119, Task 1G162203D14413. The investigation was
performed by the AiResearch Manufacturing Company of Arizona,
a division of The Garrett Corporation, under the control of
the United States Army Aviation Materiel Laboratories
(USAAVLABS), Fort Eustis, Virginia.

The engineering project that implemented this program was the
Propulsion-Engine Advanced Technology Project headed by
F. Weber. The program manager, responsible to Mr. Weber, was
J. L. Helmbrecht. Additional investigators were G. W. Bowers,
Dr. R. F. Kirby, J. A. Pyne, R. H. Sargent, Dr. W. F.
Waterman, and A. E. Wilson. In addition, the guidance of
Mr. E. Johnson of USAAVLABS is gratefully acknowledged.

v

TABLE OF CONTENTS

LIST OF ILLUSTRATIONS

xii

xiii

LIST OF TABLES

LIST OF SYMBOLS

A_o	external surface area, sq ft
acr'_2	sonic velocity (abs) rotor inlet, ft/sec
acr'_3	sonic velocity (abs) rotor exit, ft/sec
acr''	sonic velocity (rel) rotor exit, ft/sec
D_s	suction surface diffusion
D_p	pressure surface diffusion
F_{tu}	average ultimate tensile strength of disk material, psi
h_o	external film coefficient of heat transfer, Btu/hr-sq ft-°F
I_p	power moment of inertia, lb/in./sec^2
K	reaction ratio
Kc	tip clearance parameter, in.
N_B	burst speed, ft/sec
N_D	design speed, ft/sec
q_o	surface heat transfer, Btu/hr
T'_1	turbine inlet temperature, °F
T_{aw}	adiabatic wall temperature of gas, °F
T_c	coolant temperature, °F
T_w	wall temperature, °F
U_H	turbine hub speed, ft/sec
V	absolute velocity
V_u	tangential component of absolute velocity
W	compressor bleed flow, lb/sec
W_c	compressor through-flow, lb/sec

W_{hs}	stator hub shroud cooling flow, lb/sec
$\bar{W}_r$	rotor-cooling flow fraction of turbine inlet flow, lb/sec
$\bar{W}_s$	stator-cooling flow fraction of turbine inlet flow, lb/sec
W_{stator}	total stator-cooling flow, lb/sec
W_{ted}	stator trailing-edge discharge flow, lb/sec
W_{ts}	stator tip shroud cooling flow, lb/sec
W_t/W	total stage cooling flow
X	directed fraction of stator cooling
$\alpha_{2,H}$	stator hub exit-flow angle, deg
$\Delta H/\theta$	specific work, Btu/lb
ΔH_t	stage work, Btu/lb
η_{aero}	aerodynamic efficiency
η_{cool}	stage efficiency with cooling penalties
η_i'	stage efficiency
η_T	turbine efficiency
θ_t/lm	momentum thickness loss
λ_s	stage work coefficient
σ_B	blade root centrifugal stress, psi
σ_t	average tangential stress at design speed, psi
ϕ	hub-tip ratio

1. INTRODUCTION

This report describes a USAAVLABS-sponsored program that was
directed to determine a suitable method of turbine blade/disk
attachment. The program comprised four major efforts:

1. Aerothermodynamic Design

2. Mechanical Design and Analysis

3. Fabrication Technology Development

4. Final Specimen Fabrication and Testing

Table I presents a sequential logic flow chart that portrays
the scope of the overall program that was conducted, shows the
interrelationship of the individual activities, and in addi-
tion, lists the section number where appropriate discussion
can be found in this report.

1.1 PROBLEM STATEMENT

The desire to obtain higher performance from small gas turbine
engines has made it necessary to utilize air-cooled turbine
components in order to realize the high cycle temperature
required. Recent development activity in this area has
revealed problems associated with small cooled turbines that
have not been significant in the design of large cooled
turbine components. The problem dealt with in this program
involves the attachment of the turbine blade to the disk.

The high work requirement, the blade design compromises re-
quired to ensure adequate cooling of the small blades, and the
requirement to maintain high efficiency are the basic factors
associated with the attachment problem. These factors create
a condition that requires high solidity, and hence, close
blade spacing, combined with high stress levels in the attach-
ment region.

To provide effective cooling of the blade leading edge, inlet
relative Mach numbers must be reasonably low to lessen heat-
transfer coefficients in the region of the stagnation point.
This requirement dictates a high tip speed, and therefore,
high blade-root and disk stresses in the attachment area.

1

TABLE I.   SEQUENTIAL LOGIC FLOW CHART OF THE CONDUCTED PROGRAM

-----------------------------------AEROTHERMODYNAMIC DESIGN----------------------------------
                                              (2.)

Design Parameters   Variables

• Airflow Rate   4.0 lb/sec   • Stage Work Coefficient

• Compressor Pressure Ratio   Optimization Study   • Reaction Ratio
  10:1   (2.1)   • Disk Stress

• Turbine Inlet Temperature   • Stator-Vane Angle
  2400°F
                                         Aerodynamic Design   • Cooling Scheme
• Turbine Blade Tip Speed   (2.?)
  1500-1900 ft/sec

• Design Stress Rupture Life
  1000 hrs

                                         Literature Search
                                         • Joining Methods
                                         • Attachment Concepts

------ MECHANICAL DESIGN AND ANALYSIS --------   ------- FABRICATION TECHNOLOGY DEVELOPMENT------
                  (3.)   (4.)

       Mechanical Design Objectives   Selection of Materials
                  (3.1)   (4.1)

       Final Design of Blade   Preliminary Test Evaluation
                  (3.2)   (4.2)

       Blade/Disk Attachment Concepts   Diffusion   Braze*   Electron-   Cast Bond
                  (3.3)   Bond*   beam weld

  Mechanical Diffusion   Braze   Electron-   Feasibility
             Bond   beam weld   study to
                                                                                           evaluate
  Feasibility   method of
  study revealed   Turbine Rotor Design   fabricating
  marginal joint   (3.4)   cooled tur-
  strength   bine blade

-----------------------------------FINAL SPECIMEN FABRICATION AND TESTING-----------------------------------

        Diffusion Bond   Braze   Electron-beam weld

                         Final Specimen Design
                                (5.1)

                         Inspection of Specimens
                                (5.2)

                         Final Specimen Testing
                                (5.4)

     Diffusion Bond   Braze   Electron-beam weld

  Joint strength insufficient   Joint strength approaches   Joint strength sufficient
  to meet design requirements   design requirements
                                                                Elimination of micro-
  Joining method determined   Test data consistent   cracking in weld joint
  inadequate   is required
                                 Eligible for rotational
                                 test evaluations

*Also evaluated as a joining method for strut/shell attachment

2

Additionally, relatively large trailing edges are usually required, either because of the geometry of the internal cooling passages, or because of the necessity to provide coolant discharge at the trailing edge or vicinity. The large trailing edges increase passage blockage, and to maintain blockage values at acceptable levels the blade pitch must be increased. This, however, is in opposition to the requirement of high solidity, and the only alternative is to increase the axial chord. Increased axial chord results in reduced blade aspect ratios that increase end wall and secondary flow losses. The relatively large chord and the high stresses in the attachment region combine to create a difficult attachment problem.

Use of a more conventional attachment, such as a fir tree, results in either excessively wide, and hence, heavy disks, or, depending upon the severity of factors involved, unacceptably low stress-rupture life for the attachment.

1.2 APPROACH

In view of the aforementioned difficulties, the technical approach that was taken by this program to evolve a suitable method of blade/disk attachment included:

1. An aerothermodynamic trade-off study to establish an optimized turbine design

2. A literature survey and analytical study to select several candidate turbine blade/disk attachment concepts and joining processes

3. Experimentation to determine and refine the most acceptable attachment method(s) from the selected candidates

4. Testing to substantiate the integrity of the final refined attachment method(s)

3

2.   AEROTHERMODYNAMIC DESIGN

To make a realistic evaluation of the turbine blade/disk attachment, it is first necessary to generate a blade design that incorporates geometry consistent with the aerothermodynamic requirements of the assumed turbine. For the small air-cooled turbine, realization of high efficiency values becomes difficult because of blade design compromises dictated by cooling-geometry requirements.

The objective of the aerothermodynamic design activity was to establish a small air-cooled axial-flow turbine design optimized to obtain the best balance between the lowest possible specific fuel consumption (SFC) and the highest possible specific horsepower (sp hp). To accomplish this goal, an extensive study was conducted to determine the best compromise of (a) turbine efficiency, (b) cooling geometry and hence cooling airflow rate, (c) blade stress, (d) disk stress, and (e) blade/disk fabrication considerations.

The single-stage axial-flow turbine analyzed was assumed to drive the compressor in a small gas turbine engine having a free power turbine. Design-point parameters were as follows:

1. Airflow rate   4.0 lb/sec

2. Compressor pressure ratio   10:1

3. Turbine inlet temperature   2400°F

4. Turbine adiabatic efficiency   0.83 - 0.85
    (goal)

5. Turbine tip speed   1500-1900 ft/sec

6. Stress-rupture life   1000 hr

2.1   OPTIMIZATION STUDY

The optimization study was initiated by a cycle analysis of the engine in which the turbine component was assumed to have application.

2.1.1   Cycle Analysis

The basic turbine configuration assumed for the cycle analysis included a single-stage gas generator turbine with the capability of driving a 10:1 pressure ratio compressor having an airflow rate of 4 lb/sec. (Either a single- or two-stage free-power turbine can be assumed downstream of the gas generator.) It was assumed that the power turbine design would be

4

selected so that no blade or vane cooling would be required.

Specific cycle parameters used in the analysis are shown in Table II. As indicated in Table II, the cycle analysis was undertaken for constant cycle pressure and temperature ratio over a range of compressor bleed fractions and gas generator turbine efficiencies.

TABLE II. PARAMETERS USED IN CYCLE ANALYSIS (SEA-LEVEL STANDARD DAY)	
Type	Value
Turbine inlet temperature, °F	2400
Compressor pressure ratio	10.0
Compressor airflow, lb/sec	4.0
Compressor efficiency	0.80
Compressor bleed flow for turbine cooling, lb/sec	Variable
Combustor efficiency	0.98
Combustor loss - $\Delta P/P$	0.05
Cycle leakage	0.0
Lower heating value of fuel - Btu/lb	18,400
Gas generator turbine efficiency	Variable
Interstage duct loss - $\Delta P/P$	0.02
Power turbine efficiency (total-to-static)	0.87
Mechanical efficiency	0.98
Accessory horsepower	0.0

It was assumed that the compressor bleed air used for cooling the gas generator turbine re-enters the mainstream gas flow ahead of the power turbine.

The relationship of SFC and sp hp versus compressor bleed fraction (W/W_c) for various values of turbine efficiency (η_T) was determined. With the turbine design assumed to be in the region of $\eta_T = 0.84$ and $W/W_c = 0.12$, the following influence coefficients were found to prevail:

$$\frac{\Delta SFC/SFC}{\Delta \eta_T \ \eta_T} \ W/W_c = -0.89 \tag{1}$$

$$\frac{\Delta W/W_c}{\Delta \eta_T \ \eta_T} \ SFC = 1.30 \tag{2}$$

$$\frac{\Delta sp \ hp/sp \ hp}{\Delta \eta_T \ \eta_T} \ W/W_c = 0.95 \tag{3}$$

$$\frac{\Delta W/W_c}{\Delta \eta_T \ \eta_T} \ sp \ hp = 0.51 \tag{4}$$

These partial derivatives indicated the relative importance of gas generator turbine efficiency and cooling flow for maintaining a given SFC or sp hp. Thus, a favorable trade-off in SFC can be achieved if cooling-flow requirements do not increase more rapidly than 1.3 times the turbine efficiency increase for a given design change. Similarly, an increase in sp hp can be realized if the cooling requirement does not increase more rapidly than 0.51 times the turbine efficiency increase.

2.1.2 Cooling Considerations

To perform the optimization study, existing analysis procedures and computer programs were used where available; however, analysis procedures and subroutines had to be written so that turbine cooling-flow requirements could be included in the study. Procedures were written to provide an estimation of cooling-flow requirements for the turbine stage as shown in Figure 1.

6

1. VANE BAND FILM COOLING

2. VANE COOLING, INTERNAL

3. BLADE COOLING, INTERNAL

4. DISK COOLING, IMPINGEMENT
   AND RADIAL FLOW

5. SHROUD COOLING
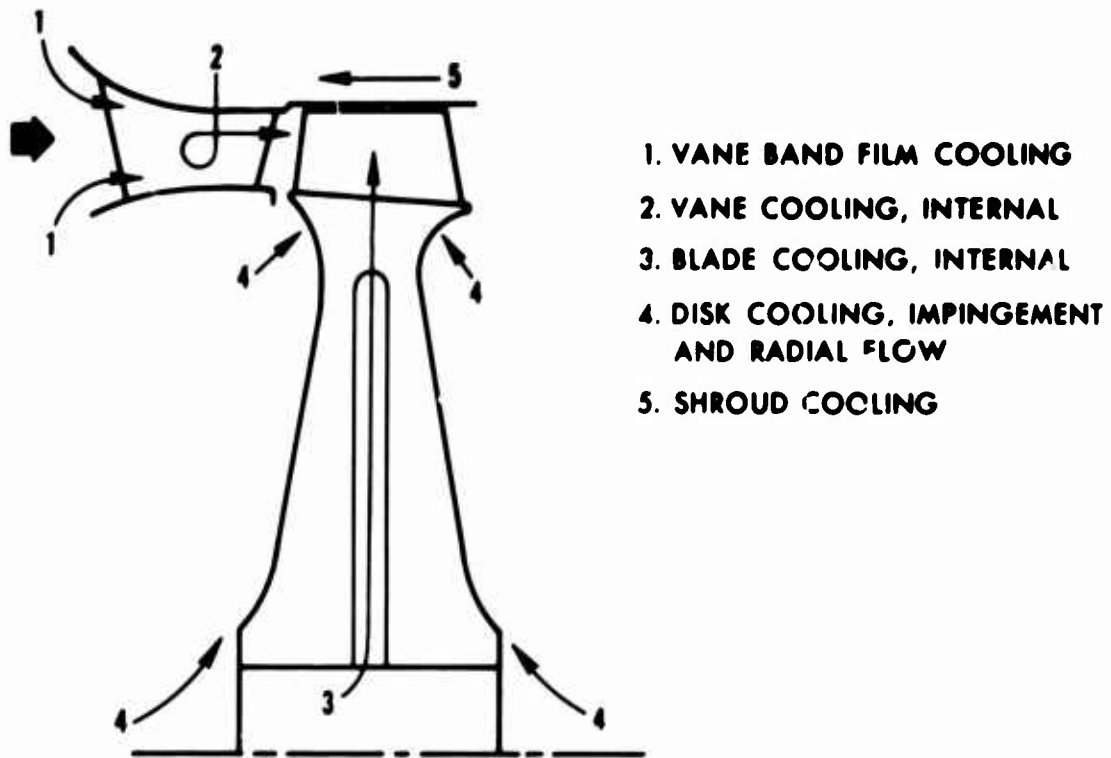
Figure 1. Turbine Stage Cooling.

An adequate description of heat transfer to the surface is
needed to determine the cooled-component coolant flow require-
ment. In general, heat transfer to the surface, q_o, may be
written as

$$q_o = h_o A_o (T_{aw} - T_w) \tag{5}$$

where h_o = the external film coefficient of heat
                    transfer

          A_o = the external surface area

          T_{aw} = the adiabatic wall temperature of the gas

          T_w = the wall temperature

The routines were written such that the coolant flow rate was
determined iteratively by matching desired and actual wall
temperatures. The desired wall temperature was determined
from both stress considerations and material oxidation limits.
The adiabatic wall temperature included the effects of both
radial- and circumferential-temperature profiles, as required.
The external film coefficient and surface area were computed
in the turbine sizing routine. The turbine stage cooling

7

considerations contain approximations which, while believed to be realistic, require detailed design and subsequent experimental confirmation. Brief descriptions of the turbine stage cooling considerations are presented in subsequent paragraphs.

2.1.2.1 Vane Band Film Cooling

Vane bands are most readily cooled to acceptable oxidation limit values by use of film-cooling techniques. In film cooling, the coolant is injected into the main gas stream in a direction essentially tangent to the surface to be cooled.

The required adiabatic wall temperature with film cooling was based upon a relation derived from an equivalence of external and internal heat-transfer rates on the film-cooled surface. Values for internal film coefficients were chosen to be consistent with moderate cold-side cooling. The external film coefficient was computed from the turbulent flat-plate, heat-transfer correlation. The film-cooling flow rate was then computed from these quantities and a film-cooling correlation.

2.1.2.2 Vane Cooling – Internal

Procedures were written and programmed to define four different stator-vane cooling configurations. Those considered are shown schematically in Figure 2. Where possible, realistic geometric approximations for each of the four stator-vane cooling configurations were based on existing designs.

To prevent the occurrence of difficult cooling problems associated with small leading-edge diameters and large values for external film coefficients, a check was incorporated in the program to warn against external film coefficients exceeding 1000 Btu/hr-sq ft-°F. Wall temperature was controlled as a function of the oxidation limit of the selected vane material. The coolant flow rate required was compared with choking conditions at the discharge of the vane.

2.1.2.3 Blade Cooling – Internal

Procedures were written and programmed to define four different rotor-blade cooling configurations. Those considered are shown schematically in Figure 3.

Comments regarding the stator analysis are applicable to the rotor except that the discussion on wall temperature applies to the sheet metal shell at the tip and at the trailing edge in Configuration (a) only. The metal temperatures of the other blade configurations and of the strut of Configuration (a) were controlled by matching wall temperature with allowable temperature consistent with 1000-hour stress-rupture life characteristics of the selected blade material.

8
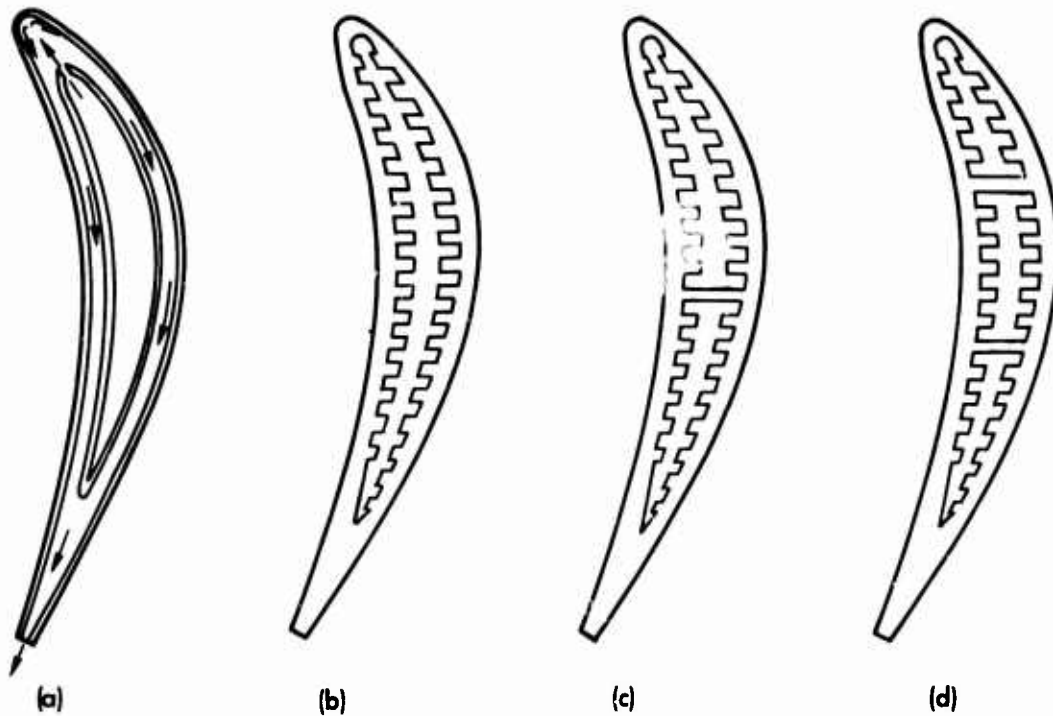
CONFIGURATION (a) :

        IMPINGEMENT-COOLED LEADING EDGE
        CHORDWISE FLOW IN MID-CHORD REGION
        TRAILING-EDGE COOLANT DISCHARGE

CONFIGURATION (b) :

        SINGLE-PASS RADIAL FLOW

CONFIGURATION (c) :

        TWO-PASS RADIAL FLOW
        TIP COOLANT DISCHARGE

CONFIGURATION (d) :

        THREE-PASS RADIAL FLOW
        COOLANT DISCHARGE AT INNER BAND

Figure 2. Candidate Stator-Vane Cooling
             Configurations.

9
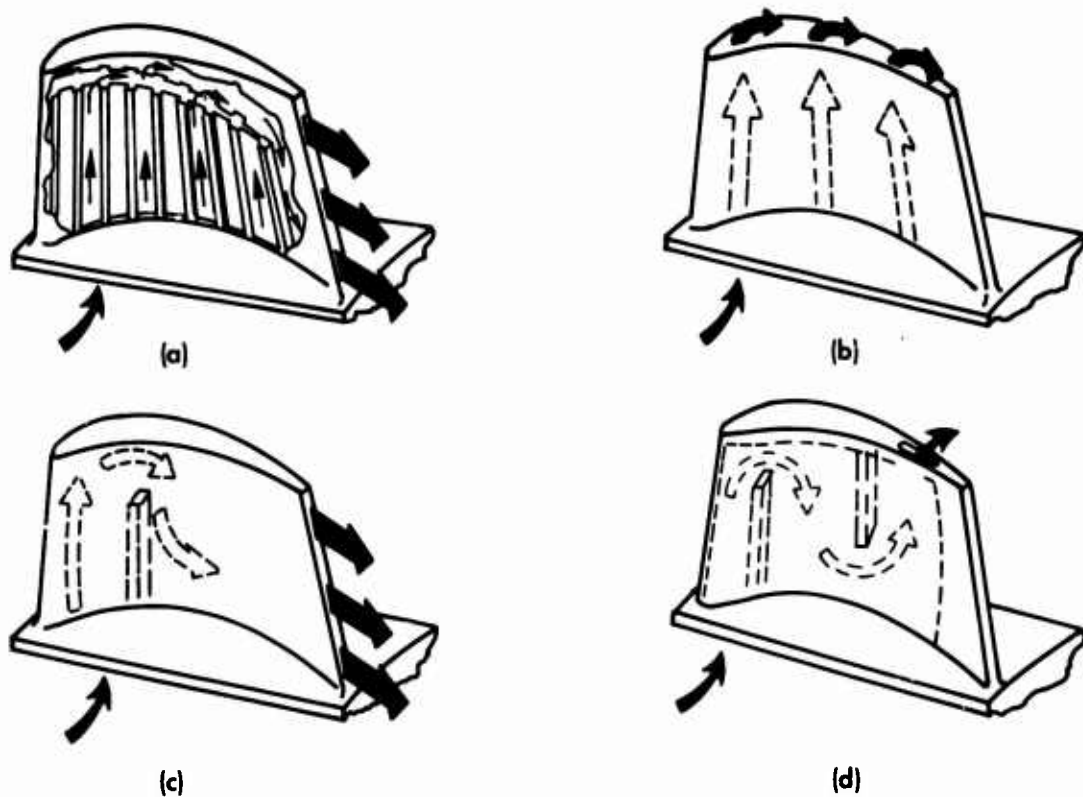
CONFIGURATION (a) :

- STRUT-SUPPORTED SHEET METAL SHELL
- RADIAL FLOW
- TRAILING-EDGE COOLANT DISCHARGE

CONFIGURATION (b) :

- SINGLE-PASS RADIAL FLOW

CONFIGURATION (c) :

- TWO-PASS RADIAL FLOW

CONFIGURATION (d) :

- THREE-PASS RADIAL FLOW

Figure 3. Candidate Rotor-Blade Cooling Configurations.

2.1.2.4 Disk Cooling, Impingement, and Radial Flow

Disk cooling included both impingement cooling at the rim and radial flow. For radial flow cooling, a seal was assumed to exist at 80 percent of the rim radius. The coolant flow rate was taken as equal to the pumping flow for this portion of the disk. This was based on the assumption that these conditions will tend to prevent hot-gas recirculation from the mainstream along the sides of the disk.

2.1.2.5 Shroud Cooling

The blade shroud is exposed to an environment similar to that of the film-cooled outer vane band. Procedures were written to provide geometric approximations of an axial-flow scheme for cooling this component. Wall temperature was controlled as a function of the oxidation limit of the material.

2.1.3 Analysis Technique and Optimization Procedure

The analysis method utilized for the optimization study was developed by combining existing programs with new subroutines that were written to account for the effect of the turbine stage cooling considerations. Table III, the computer program flow diagram, shows (a) the existing programs that were used to determine the basic turbine design parameters necessary to define the performance of an uncooled turbine, and (b) the new subroutines that were added to determine the effect of the turbine stage cooling considerations. Discussions of the new subroutines are presented in subsequent paragraphs.

Allowable metal temperatures in the rotor were computed as a function of radius from the local centrifugal stress level and life requirement by the use of the Larson-Miller curve input to the program. The imposed heating rate was then calculated with the use of the values of external film coefficient, adiabatic wall temperature, and surface area previously determined. The heating load was then used in the internal heat-transfer analysis to determine the cooling airflow required to maintain, at steady state, the required wall temperatures.

Performance penalties resulting from the calculated cooling-flow requirements of stator and rotor were computed to accomplish this. A certain fraction, X, of the stator cooling-flow requirement was considered to be available to do work in the rotor, and hence, behaved as though there were no cooling-flow penalty for this portion of the stage cooling requirement. The fraction X, called the directed fraction of stator-cooling air, was defined as

11

TABLE III. COMPUTER PROGRAM FLOW DIAGRAM FOR COOLED TURBINE DESIGN OPTIMIZATION

Stress rupture data Cycle design-point data Blade taper data Gas properties Disk design data Blade angles Allowable stress and life Work coefficients Cooling geometry parameters Axial chord	
	AiResearch Program No. 5849
Compute turbine overall conditions to satisfy work, flow, and stress or speed requirements.	
Compute detailed turbine vector diagrams at each station through the turbine for free vortex distribution.	AiResearch Program No. 5597
Compute local turbine blading losses, 2 and 3-D efficiency.	AiResearch Program No. 5665
Calculate blade external heat transfer coefficients. Calculate heat flow rates resulting from metal temperature necessary to satisfy life requirements at imposed stress level.	
Calculate stage cooling airflow required to handle imposed heating loads subject to the cooling passage geometry and internal heat transfer correlations specified.	Calculation procedure added for turbine cooling airflow prediction
Compute turbine efficiency penalties (bypass and pumping losses) resulting from predicted cooling air requirements. Compute overall cooled turbine efficiency including 2-D blade losses, aspect ratio losses, tip clearance losses, and cooling-air penalties.	
Compute turbine disk geometry and rotor weights necessary to satisfy imposed blade loads and specified disk stress.	AiResearch Program No. 5849
Print output data	Added printout for combined programs

12

$$X = \frac{W_{ts} + W_{hs} + W_{ted}}{W_{stator}} \frac{T_{c, in}}{T_1'} \qquad (6)$$

where W_{ts} = stator tip shroud cooling flow

W_{hs} = stator hub shroud cooling flow

W_{ted} = stator trailing-edge discharge cooling flow (if applicable)

W_{stator} = total stator-cooling requirement

$T_{c, in}$ = coolant inlet temperature

T_1' = turbine inlet temperature

It was assumed that the remaining fraction (1-X) of the stator-cooling air and all of the rotor-cooling air were not available to do work in the rotor, and that pumping work must be done to enable the cooling air to flow through the rotor.

Applying these concepts to the power output of the cooled stage yielded the following expression:

$$\frac{HP_{cooled}}{HP_{uncooled}} = (1+X\overline{W}_s) - \frac{U_H^2}{gJ\Delta H_t} (1-X) \overline{W}_s + \overline{W}_r \qquad (7)$$

where $\overline{W}_s$ = stator-cooling flow fraction of turbine inlet flow

$\overline{W}_r$ = rotor-cooling flow fraction of turbine inlet flow

ΔH_t = stage work per lb

It was apparent that this ratio may be greater or less than unity, depending on the relative amounts of stator- and rotor-cooling and on the turbine hub speed, U_H. For the purpose of analysis, this power ratio was assumed to be an efficiency ratio. Thus, the cooled turbine efficiency was calculated from

$$\eta_{cool} = \frac{HP_{cooled}}{HP_{uncooled}} \eta_{aero} \qquad (8)$$

13

where η_{aero} = attainable turbine efficiency calculated previously

Note that η_{cool} is not a true efficiency in the thermodynamic sense, since the flow through the turbine is not constant during the expansion process. However, η_{cool} represents the work capacity of a cooled turbine relative to an uncooled turbine having the same inlet equivalent flow.

Calculating η_{cool} and $W/W_c = \overline{W}_s + \overline{W}_r$ is sufficient to determine the engine performance parameters of SFC and sp hp from the cycle study described previously.

As a final step in the calculation, the program computed a turbine disk design subject to the input design parameters and determined the average tangential disk stress and overall rotor weight.

The optimization procedure employed consisted of using the analysis technique described previously to determine η_{cool} and W/W_c for a wide range of turbine designs satisfying the input requirements. The values of cooled turbine efficiency and stage cooling flow fraction uniquely determine values of engine SFC and sp hp according to the cycle analysis. The optimum turbine configuration was considered to be the design that achieves the best balance between minimum SFC and maximum sp hp.

The study was divided into three phases, as summarized in Table IV. The first phase considered the effect of two primary independent variables:

1. Turbine stage work coefficient at the hub,

$$\lambda_s = \frac{V_u}{U_{2H}} - \frac{V_u}{U_{3H}} \tag{9}$$

2. Turbine blade root centrifugal stress based upon turbine exit annular area,

$$\sigma_B$$

In Phase II, the study of Phase 1 was repeated at a higher rotor hub reaction ratio K. Phase III considered the

14

TABLE IV. OPTIMIZATION STUDY PHASES

Phase I

λ_s = 2.0, 2.5, 3.0, 3.5, 4.0

σ_B = 10, 20, 30, 40, 50, 60 ksi

$\alpha_{2,H}$ = 70°

Stator Configuration: (a)
Rotor Configuration: (a)

K = 1.2

Phase II

λ_s = 2.0, 2.5, 3.0, 3.5, 4.0

σ_B = 10, 20, 30, 40, 50, 60 ksi

$\alpha_{2,H}$ = 70°

Stator Configuration: (a)
Rotor Configuration: (a)

K = 1.4

Phase III

Without Stator Cooling

For Optimum of
Phase I
(λ_s = 3.0, σ_B = 35 ksi)

$\alpha_{2,H}$ = 64° to 80°

Without Stator Cooling

For Optimum of
Phase II
(λ_s = 2.5, σ_B = 30 ksi)

$\alpha_{2,H}$ = 64° to 80°

Stator Configurations:
(a), (b), (c), (d)

Rotor Configurations:
(a), (b), (c), (d)

Blade Taper Ratio: Varied

effects of additional variables while holding constant the optimum conditions derived from Phases I and II.

The first step in the optimization procedure was to select a design point with regard to turbine efficiency and compressor bleed flow. It was necessary that this design point lie in the range of the predicted efficiency level and cooling requirement so that the turbine work would match the compressor work. The design point selected was

$$\eta_{cool} = 0.84, \quad W/W_c = 0.10$$

The design-point input parameters that are common to all three phases are listed in Table V. Figure 4 shows the assumed combustor radial profile, and Figure 5 shows the blade cross-section area distribution, which was based upon previous turbine designs.
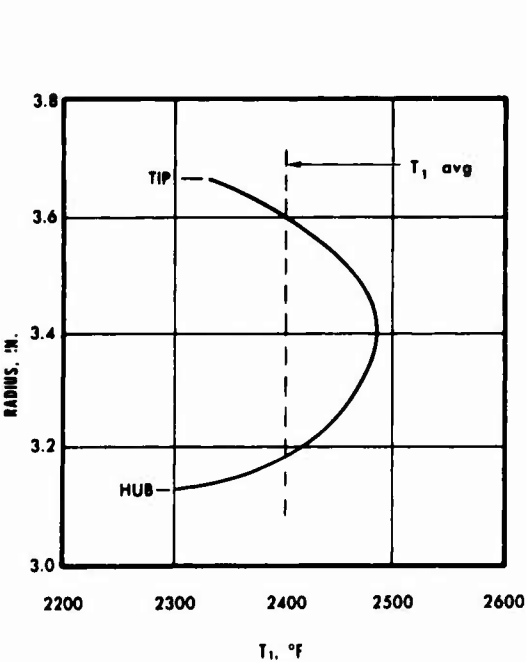
Figure 4. Assumed Combustor Radial Profile.
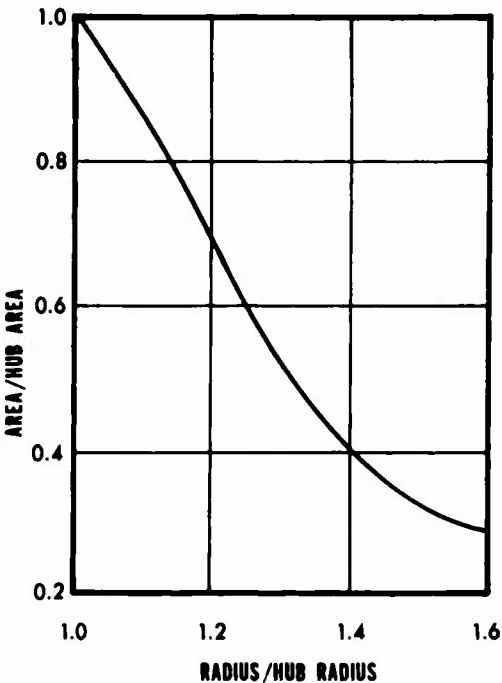
Figure 5. Blade Cross-Section Area Distribution.

16

TABLE V. DESIGN POINT INPUT PARAMETERS COMMON TO ALL THREE STUDY PHASES	
Parameter	Value
Inlet temperature - °F	2400
Specific work - Btu/lb	28.0
Adiabatic efficiency	0.88
Stage entropy split - $\Delta S_{stator}/\Delta S_{stage}$	1/3
Gas constant - Btu/lb-°R	53.399
Prandtl number	0.7
Pressure surface diffusion, stator	0.5
Pressure surface diffusion, rotor	0.5
Disk stress - psi	60,000
Material density, blade and disk - lb/cu ft	527.04
Wall temperature, stator - °F	2000*
Root conduction to disk - °F	-100
Coolant temperature rise (from source) - $\Delta T/T$	0.12
Disk taper angle - deg	15
Disk hole, radius - in.	0
Axial chord, stator vane tip - in.	1.0
Axial chord, rotor blade hub - in.	1.0
Trailing-edge thickness, stator - in.	0.04
Trailing-edge thickness, rotor - in.	0.04

*Except for Phase III (without stator cooling).

Values listed for blade axial chord and trailing-edge thickness resulted basically from fabrication and cooling considerations. As discussed later in the text, the blade and vane sheet metal thickness was selected to be 0.010 inch. To provide for sufficient area to discharge the coolant through the trailing edge, it was found that a passage width of approximately 0.020 inch would be required, including 20 percent blockage for internal structural members. Thus, the trailing-edge thickness becomes 0.040 inch (0.010 + 0.010 + 0.020 inch). Preliminary evaluations indicated that solidity requirements of the turbine design would require an axial chord of approximately 1.0 inch for the selected trailing-edge thickness if reasonable blockage values were maintained. This was verified by the optimization study.

2.1.4 Results of Optimization Study

The results of the optimization study are presented in the following subparagraphs. Twenty-five turbines were analyzed for the specified range of blade stress and hub work coefficients. The predicted values of η_{cool} and W/W_c are plotted on the SFC and sp hp graphs that were determined from the cycle analysis and are discussed and shown on the following pages.

2.1.4.1 Phase I

The first phase of the study as shown in Table IV was run at a reaction ratio, K, of 1.2 and considered hub work coefficient, λ_s, and blade root stress, σ_B, as primary independent variables.

The results of the Phase I study are presented in Figure 6, where λ_s and σ_B are plotted as parameters on the curves of SFC and sp hp versus W/W_c (determined from cycle analysis). Several important trends are apparent from these graphs:

1. The blade centrifugal stress level plays a dominant role in controlling rotor blade height, and, hence, turbine efficiency. This result is due to the strong effect of tip clearance-to-blade height ratio on rotor blade losses for turbines in this design equivalent flow range.

2. Both blade centrifugal stress level and stage work coefficient directly control turbine size (diameter). The curves indicated that turbine size was a significant factor in determining overall stage cooling requirements.

18
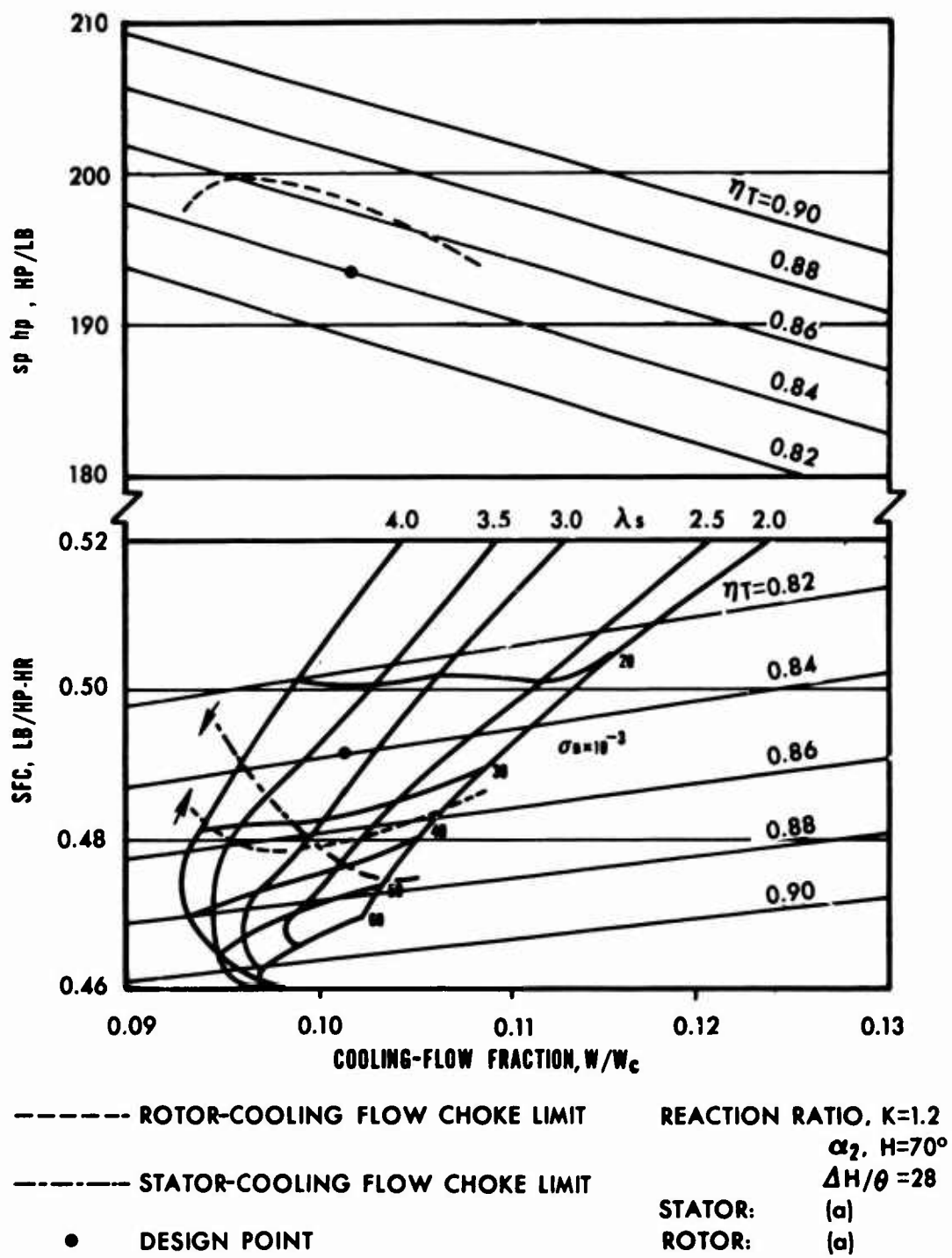
Figure 6. Phase I Results of Optimization Study.

3. As the blade stress level was increased for a
given stage work coefficient, turbine effi-
ciency increased and cooling flows decreased.
However, a point was reached where the rotor-
cooling requirement became dominant due to the
low metal temperatures required. This point
was dependent upon the stage work coefficient,
but was generally in the range from 40,000 to
60,000 psi blade stress. Beyond this stress
level, cooling flows increased, although turbine
efficiency continued to improve. However,
diminishing returns in SFC and sp hp were
realized.

From these considerations alone, the desirability of operating
the turbine at as high a stress level as feasible was apparent.
This limiting stress level was determined by the flow capacity
of the cooling flow passages in the rotor. Thus, as turbine
size was reduced by increasing blade stress, rotor blade cool-
ing requirements increased. A point was reached where the
discharge area of the cooling passage choked. In this study,
it was assumed that sufficient total pressure was available to
choke the cooling-passage discharge area at the downstream
static pressure level. This point represented a limit in
blade stress that cannot be exceeded without major improve-
ments in cooling-passage design and manufacturing capabilities.

The locus of the rotor-blade cooling-flow choke points is
indicated in Figure 6. This figure indicates that an optimum
value of blade stress and hub work coefficient exists both
for SFC and sp hp. Peak sp hp required designs having slightly
higher stage work coefficients and reduced stress levels in
comparison to minimum SFC. However, the differences were not
great, and design levels of σ_B and λ_S can be selected to
provide the best compromise.

For this particular phase of the study, an optimum design con-
dition appeared to be

$$\sigma_B = 35,000, \quad \lambda_S = 3.0$$

However, the turbine vector diagram for the 1.2 reaction ratio
required a rotor inlet critical Mach number of 0.82 at the hub
radius. At the same time, consideration of the rotor leading-
edge cooling problem required a leading-edge diameter of 0.082
inch, which is considerably larger than desired if shock ef-
fects are to be minimized at this high inlet Mach number. This

20

leading-edge diameter, along with the blade pitch required for
optimum passage solidity, resulted in large leading-edge
blockage ratios.

2.1.4.2 Phase II

To reduce the complexities encountered in Phase I, the second
phase of the study considered the effects of an increase in
rotor hub reaction ratio to K = 1.4, with all other input
quantities remaining fixed. The results of repeating the
analysis for K = 1.4 are presented in Figure 7.

The general trends outlined in Phase I for K = 1.2 were pre-
served for this study. It is notable that the higher reaction
blading had a somewhat increased cooling-flow requirement.
However, turbine efficiency levels also increased, so that the
net result, in terms of SFC and sp hp at the optimum point,
was a slight increase in SFC and a slight decrease in sp hp
for the higher reaction case.

The optimum design point for K = 1.4 was also determined by
the flow capacity of the rotor cooling-flow passages. In this
case, the design condition becomes

$$\sigma_B = 30,000, \quad \lambda_S = 2.5$$

It may be noted that no solution actually exists that satis-
fies both stator and rotor. However, since the choke flow
characteristic for the stator is an insensitive function, it
is felt that its significance is of second order. Therefore,
emphasis is placed upon the rotor characteristic for deter-
mination of the optimum design point.

The turbine for this design condition had a rotor inlet crit-
ical Mach number of 0.70 at the hub. The leading-edge diameter
required for cooling this case was 0.076 inch. The combina-
tion of this leading-edge diameter with an increased blade
pitch at optimum passage solidity resulted in a lower leading-
edge blockage ratio at a reduced inlet critical Mach number
compared to the low reaction design.

2.1.4.3 Phase III

The following subparagraphs are concerned with examining the
effects of changing some of the parameters held constant
during the investigations previously described.
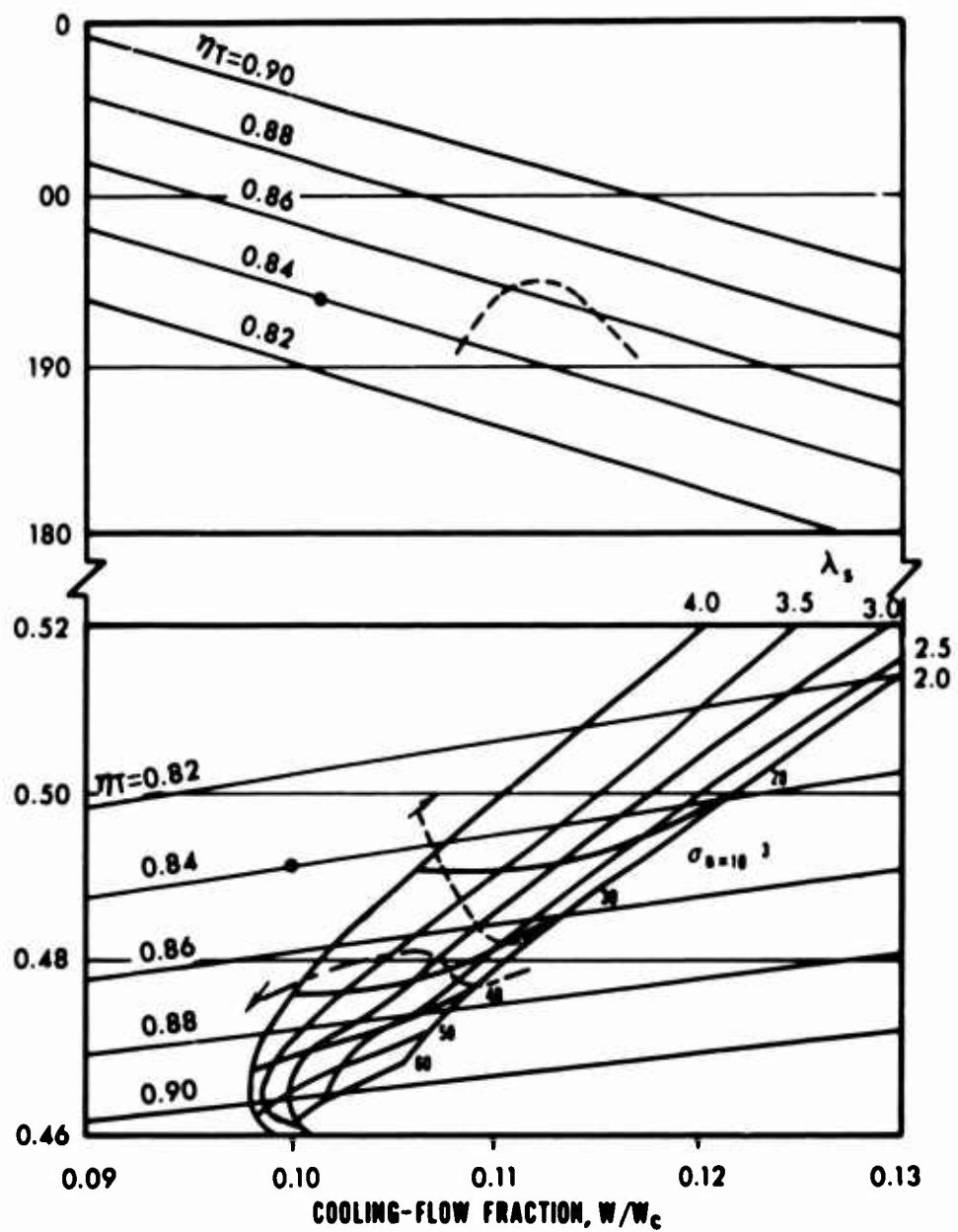
21

Figure 7. Phase II Results of Optimization Study.

No Stator Cooling

Consideration was first given to changes in the optimum design conditions. that resulted from considering only penalties due to rotor cooling. In the program, this was achieved by raising the allowable stator metal temperature above the turbine inlet temperature. Physically, this required that a stator material be found that did not require cooling.

The complete analysis was repeated with the preceding assumptions for both K = 1.2 and K = 1.4. Since the stator no longer required cooling, the turbine design point shifted to a lower $\Delta H/\theta$, which was a reflection of the increased turbine through-flow and reduced turbine pressure ratio required to drive the compressor.

The general trends with respect to changes in λ_s and σ_B previously determined were preserved. It is important to note than an improvement in SFC of about 5 percent and an increase in sp hp of about 10 percent at the optimum design point resulted from the elimination of stator cooling-flow penalties. However, it was believed that the stator cooling-flow penalties employed in the earlier study were more realistic in terms of current materials technology. Therefore, optimization of the turbine design was confined to configurations having cooled stators and cooled rotors.

Effect of Stator Hub Exit-Flow Angle

The effects of changes in stator hub exit-flow angle, $\alpha_{2,H}$ on SFC and sp hp at the turbine design points corresponding to the following were considered (optimum values from Phases I and II):

$$K = 1.2, \quad \lambda_s = 3.0, \quad \sigma_B = 35,000$$

$$K = 1.4, \quad \lambda_s = 2.5, \quad \sigma_B = 30,000$$

For these two design conditions based on $\alpha_{2,H} = 70°$, $\alpha_{2,H}$ was varied from 60° to 80°, while all other variables remain fixed. Results of this analysis are shown in Figure 8. This figure shows that $\alpha_{2,H} = 70°$ was optimum when considering both SFC and sp hp.
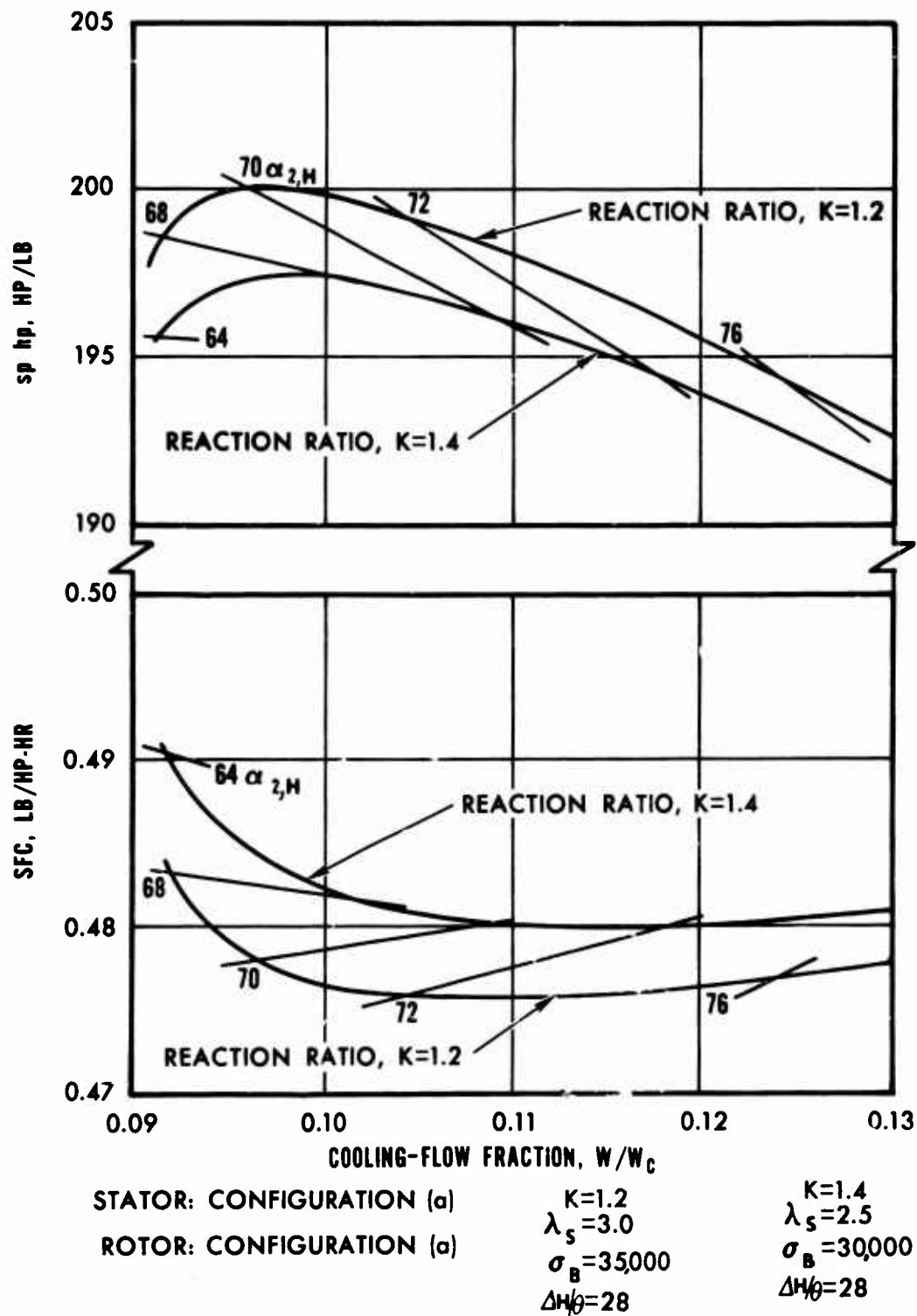
Figure 8. Phase III Results of Optimization Study.

Effect of Stator- and Rotor-Cooling Schemes
(Ref. Figures 2 and 3)

Figure 9 shows the effects of stator- and rotor-cooling con-
figurations (b), (c), and (d) on SFC and sp hp at the optimum
design point for the originally selected cooling configura-
tion, (a). From this investigation, it appeared that the
original cooling configuration (a) provides the best results
in terms of SFC and sp hp, although some of the other con-
figurations required lower overall cooling flows.

The stator-cooling configuration (a) provided the highest per-
formance because of the higher percentage of directed stator-
cooling flow. This result stemmed from the trailing-edge
cooling-air discharge arrangement in contrast to the single-,
double-, and triple-pass radial-discharge stator-cooling con-
figurations.

The selected rotor-cooling configuration (a) provided the best
overall rotor-cooling performance mainly because the load-
carrying member (strut) was somewhat insulated from the full
effect of mainstream gas temperature by the conduction tem-
perature drop through the sheet metal skin.

Varying Blade Taper

Figure 9 also indicates the effect of an increased blade
cross-sectional area taper assumption on overall performance
at the optimum design point for K = 1.4. The increased blade
taper resulted in a 2-percent reduction in SFC, due to reduc-
tion in cooling requirement from 0.11 to 0.10, along with an
efficiency increase of 1-1/2 points. However, it should be
noted that the increased blade taper would be extremely dif-
ficult to achieve in practice, since it would result in severe
compromises in aerodynamic and cooling-passage geometry. It
is believed that the original blade taper curve (normal taper)
represents a realistic approximation to the design of a cooled
turbine blade.

2.1.5 Design Selection

Preliminary investigation of the two candidate designs (K = 1.2
and K = 1.4) indicated that the high-reaction design was the
most favorable. The reasons for selection of the high-reaction
design rather than the low-reaction design are listed below:

1. The high-reaction design had a lower inlet relative
   Mach number. This condition is desirable for
   cooled turbines requiring blunt leading edges.
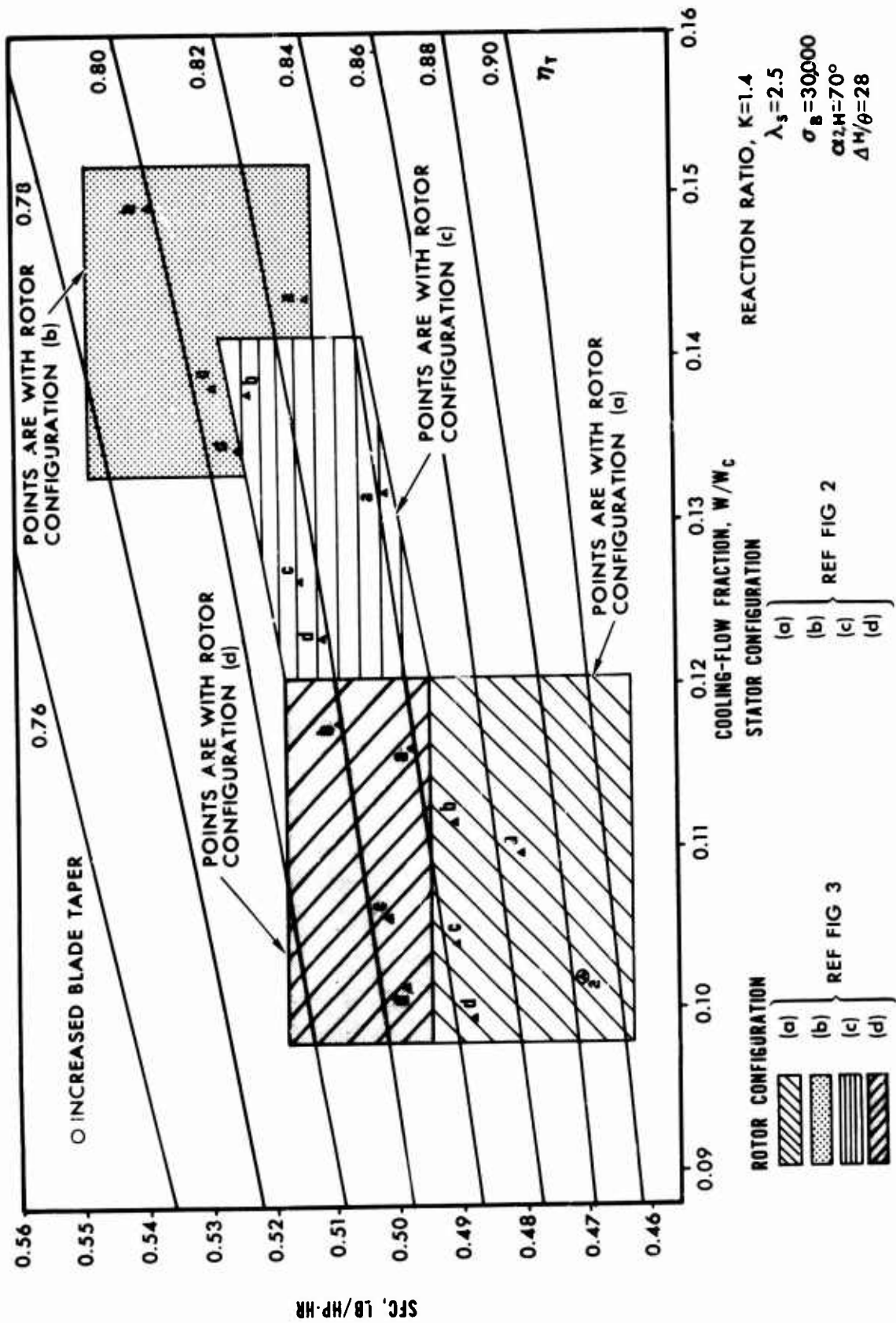
Figure 9. Effects of Stator- and Rotor-Cooling and Increased Blade Taper.

2. The high-reaction design required a smaller physical leading-edge diameter, by virtue of the reduced inlet velocity, to maintain an average leading-edge stagnation point heat-transfer coefficient of 1000 Btu/hr-sq ft-°F.

3. The high-reaction design had a lower optimum solidity requirement which, for the axial chord of 1 inch, results in a larger blade pitch.

4. Larger blade pitch requirements resulted in reduced leading- and trailing-edge blockage ratios. The increased blade pitch also provides greater flexibility in the blade attachment design.

5. Higher rotor hub reaction reduced the possibility of shock-induced boundary-layer separation in the leading-edge region, which may result in complete flow separation in the rotor. Higher reaction provides the favorable pressure gradient necessary to allow the boundary layer to remain attached to the blade surface within the guided channel.

6. Mach number and swirl angle in the downstream duct were lower for the high-reaction design. It should be noted, however, that this trend was caused primarily by the reduction in stage work coefficient, λ_S, from 3.0 to 2.5. For fixed values of λ_S, the Mach number and swirl angle in the downstream duct increase as the reaction increases.

2.2 AERODYNAMIC DESIGN

Although the stator design was not of direct value in generating blade attachment concepts and designs, certain details of the stator are presented for reference purposes. The aerodynamic design of the blade was completed in sufficient detail to provide realistic input for attachment studies.

For the reasons noted in Section 2.1.5, a detailed aerodynamic design is presented for the high-reaction-ratio (K = 1.4) turbine. Detailed turbine vector diagrams with the assumption of free vortex flow and simple radial equilibrium are given in Figure 10 for the rotor exit hub and tip radii. The meridional flow path is presented in Figure 11. Table VI lists the important aerodynamic parameters for the turbine as a function of radius.

2730 2615 1280 1545 775 59.95° 73.56° 1335

HUB
R=3.132 IN.
acr'_2=2355 FT/SEC
acr'_3=2120 FT/SEC
acr''=2215 FT/SEC

−31.67° −63.08° 2100 1115 950 −590 1280 1870

2370 2240 1500 1070 775 43.82° 70.97° 740

TIP
R=3.660 IN.
acr'_2=2355 FT/SEC
acr'_3=2120 FT/SEC
acr''=2230 FT/SEC

−27.82° −64.54° 2215 1075 950 −500 2000 1500
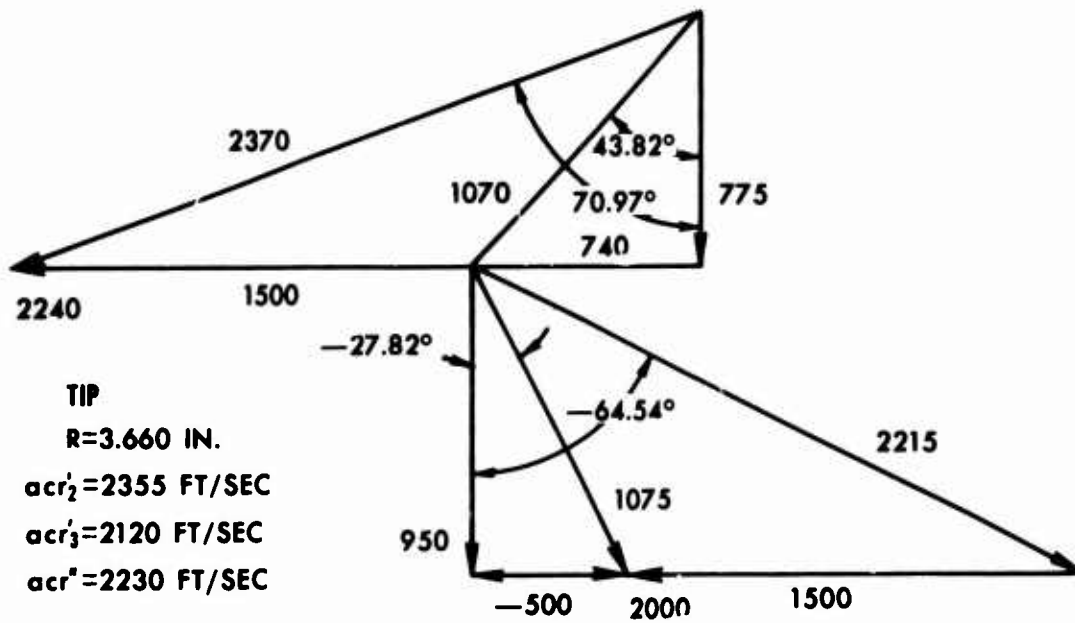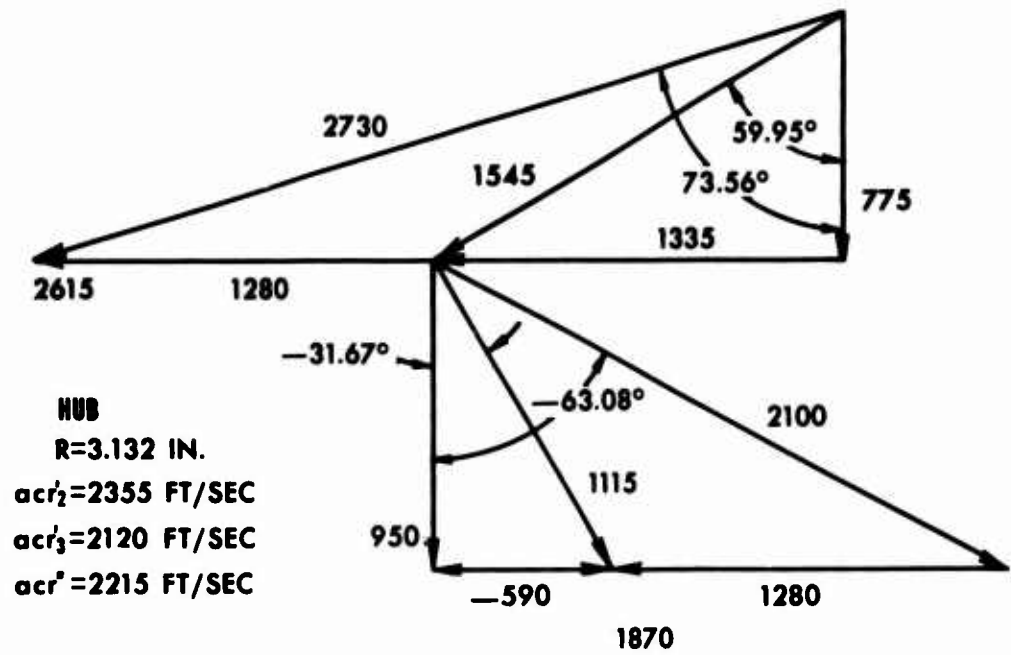
NOTE: ALL VELOCITIES IN FT/SEC

Figure 10. Turbine Vector Diagrams.

28

The results of the optimization study indicated that a rotor
hub axial chord of 1 inch is the smallest size allowable. Re-
duction of this dimension results in reduced cooling-flow
capacity in the rotor for a fixed trailing-edge blockage
ratio. Rotor trailing-edge thickness was set at 0.040 inch
for a 1-inch rotor hub chord. The effect of the resulting
trailing-edge blockage ratio on turbine efficiency is given
in the following section. The stator tip axial chord was also
set at 1 inch, with 0.040-inch trailing-edge thickness.
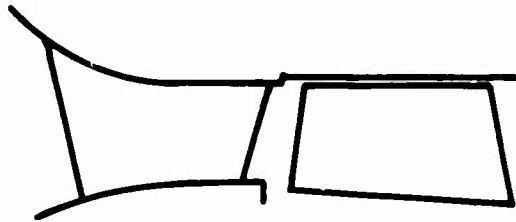
Figure 11. Turbine Meridional Flow Path.

2.2.1 Stage Efficiency Analysis

An analysis of the stage aerodynamic efficiency was carried
out by use of analysis techniques developed at AiResearch that
were based on the work of Stewart, Whitney, and Wong[1] and
Stewart, Glassman, and Vanco.[2]

Results of the aerodynamic efficiency analysis are presented
in Figures 12, 13, and 14. Figure 12 gives the local total
momentum thickness parameters per unit surface length at the
blade trailing edge versus section radius for both the stator
and the rotor. Also plotted is the local stage efficiency for
both zero and design values of stator and rotor trailing-edge
thickness. The effect of trailing-edge thickness was to
reduce the local efficiency about 1.5 points at the hub and
1.0 point at the tip. The efficiency values do not include
the effects of tip clearance.

29

TABLE VI. VECTOR DIAGRAM CONDITIONS			
Parameters	Hub	Mean	Tip
Section radius - in.	3.1316	3.3958	3.6600
Stator inlet flow angle - deg	0.0	0.0	0.0
Stator inlet - Mach no.	0.162	0.162	0.162
Stator exit flow angle - deg	73.56	72.25	70.97
Stator exit - Mach no.	1.158	1.076	1.006
Stator reaction (V_2/V_1)	7.148	6.641	6.209
Rotor inlet flow angle - deg	59.95	52.96	43.82
Rotor inlet - relative Mach no.	0.697	0.577	0.480
Rotor exit flow angle - deg	-63.00	-63.75	-64.54
Rotor exit - relative Mach no.	0.947	0.969	0.993
Rotor reaction (W_3/W_2)	1.359	1.679	2.069
Rotor hub Mach no.	0.544	0.590	0.636
Stator inlet total pressure - psia	139.6	139.6	139.6
Stator inlet static pressure - psia	137.5	137.5	137.5
Stator exit total pressure - psia	133.3	133.3	133.3
Stator exit static pressure - psia	57.94	65.57	72.18
Rotor inlet rel. total pressure - psia	77.12	79.71	82.59
Rotor exit rel. total pressure - psia	70.28	72.64	75.26
Rotor exit static pressure - psia	40.99	41.24	41.44
Stator inlet total temperature - °R	2860.0	2860.0	2860.0
Stator inlet static temperature - °R	2848.0	2848.0	2848.0
Stator exit static temperature - °R	2313.2	2387.2	2445.9
Rotor inlet rel. total temp. - °R	2527.6	2546.6	2567.1
Rotor exit abs. total temp. - °R	2321.0	2321.0	2321.0
Rotor exit static temperature - °R	2023.7	2009.8	1995.1
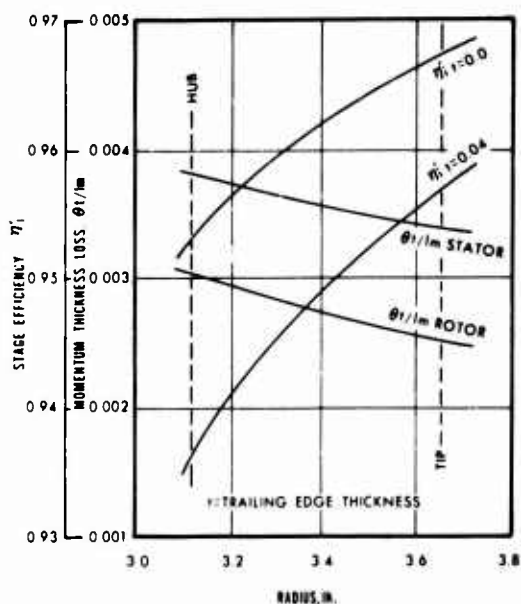
Figure 12.   Local Loss
             Characteristics.
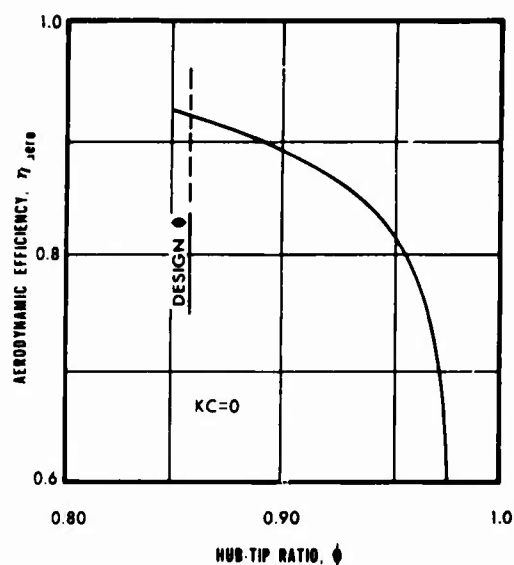
Figure 13.   Stage Efficiency
             Versus Hub-Tip
             Ratio.
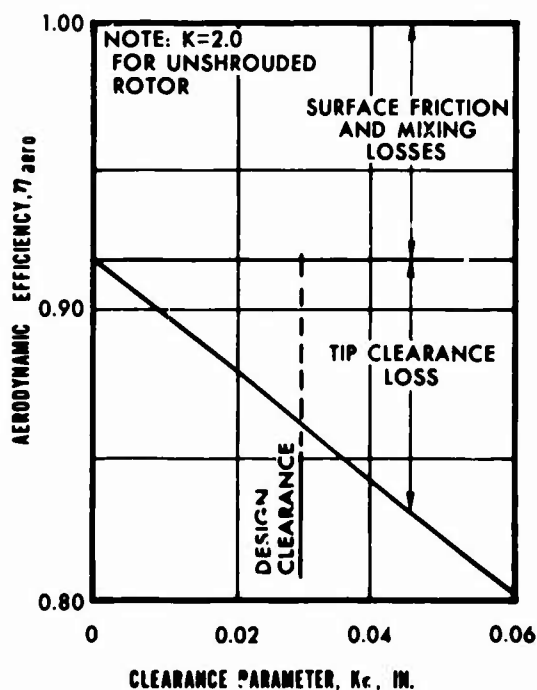
Figure 14.   Overall Stage
             Efficiency.

Figure 13 presents aero-
dynamic stage efficiency at
zero clearance versus stage
hub-tip ratio. This curve
indicates the relative mag-
nitude of the aspect ratio
correction due to end-wall
boundary-layer losses.

Figure 14 gives the overall
aerodynamic stage efficiency
as a function of the tip
clearance parameter Kc. It
is notable that, at the
design radial clearance of
0.015 inch, the loss in effi-
ciency due to clearance is
almost equal to the total of
surface friction and mixing
losses for the entire stage.
The slope of the efficiency

31

curve indicates that stage efficiency is extremely sensitive to changes in tip clearance; therefore, close control of clearance is mandatory for good efficiency.

Since the turbine stage required cooling, the predicted aerodynamic efficiency was modified to include the effects of cooling. The methods by which this correction was made are described in Section 2.1.3.

For the final turbine design, the optimization analysis predicted the following percentage of cooling-flow distributions for the stage:

Stator cooling, $(W/W_c)_S$	=	7.54 percent
Rotor cooling, $(W/W_c)_R$	=	3.44 percent
Total stage cooling, W_t/W	=	10.98 percent
Directed fraction of stator cooling, X =		44.60 percent

With use of the design values of hub speed, stage work, and cooling-flow fractions, the turbine power ratio became

$$\frac{HP_{cooled}}{HP_{uncooled}} = 1.019 \tag{10}$$

The fact that this ratio was greater than unity indicated that the increase in turbine work produced by the directed fraction of stator-cooling air was greater than the deficit in work due to the combined effects of undirected stator-cooling air and pumping work done on the rotor-cooling air. The effective stage efficiency with cooling became

$$\eta'_{aero} = 0.858 \text{ at } Kc = 0.03$$

$$\eta'_{cool} = 0.874 \text{ at } Kc = 0.03$$

It should be noted that the efficiency levels may be somewhat optimistic, since the following factors were not included in the analysis:

1. Stator and rotor shock losses

2. Secondary flow losses

32

3. Nonadiabatic flow effects such as the reduction in rotor total temperature due to stator cooling.

2.2.2 Detailed Blading Design and Analysis

The blade and vane design procedure began with the design of two-dimensional cylindrical sections satisfying the vector diagram. The sections were designed at equal radial increments from hub to tip to facilitate stacking and fairing of the profiles.

The procedure used to design the cylindrical sections followed the steps described below to generate a profile satisfying a given vector triangle.

1. A relative critical Mach number and flow angle in the plane of the trailing edge were calculated from the specified vector triangle downstream of the blade for the required blade spacing and trailing-edge thickness. The calculation assumed one-dimensional flow and satisfied continuity and momentum equations for either subsonic or supersonic flow in the plane of the trailing edge.

2. The blade suction surface was generated by an involute curve that turned from the inlet flow angle specified by the upstream vector triangle to the calculated blade angle. The blade-section stagger angle was a function of the inlet-to-exit curvature ratio of the involute curve, which was an input number. The solidity of the passage was determined from Zweifel's[3] criterion on the basis of an input aerodynamic loading coefficient.

3. The profile pressure surface was specified as input data.

4. The passage velocity distribution was calculated by estimating blade-to-blade velocity gradients and adjusting suction surface velocities until continuity was satisfied. The resulting velocity distribution generated a circulation that was in close agreement with the required value imposed by the vector diagram.

33

5.   A two-dimensional boundary-layer analysis based
     on the methods described by Whitney, Stewart, and
     Miser[4] was calculated by use of the velocity
     distribution, along with the generated blade
     profile.

The procedure that was used for this activity had several
drawbacks. The program did not determine the leading-edge
contour; therefore, the velocity distribution on this portion
of the blade could not be calculated. The effects of three-
dimensional flow within the blade row were accounted for in
an approximate manner in that the specific mass flow was
assumed to vary linearly with axial chord from the inlet to
the exit of the blade row to satisfy the vector diagram at
a given section radius. In addition, the procedure did not
account for the effect of blade wakes downstream of the
throat.

Figures 15 and 16 describe the results of the two-dimensional
cylindrical blade section design and analysis. Each figure
presents a drawing of hub and tip blade profiles in their
correct orientation, along with the calculated velocity dis-
tribution. A brief discussion of the design philosophy of
each blade row follows.

2.2.2.1 Stator

The stator was designed with 25 vanes and a trailing-edge
thickness of 0.040 inch to accommodate the internal cooling
configuration. The resulting blockage ratio of the hub
profile was 0.16, which is extremely large when compared with
uncooled designs. The losses incurred from such high blockage
ratios are difficult to determine with certainty due to inter-
actions of the wake and mainstream flow.

The calculated vane channel velocity distributions are given
in Figure 15. As a result of the high reaction, little suc-
tion or pressure surface diffusion is apparent.

The leading-edge radius of 0.100 inch was selected to minimize
stagnation-point heat-transfer coefficients and to allow suf-
ficient room for good internal cooling.

The complete vane profile was defined by stacking the designed
cylindrical sections on a radial line passing through the
center of the throat of each section. Vane pressure surfaces
were adjusted to ensure a smooth fairing from hub to tip.

34
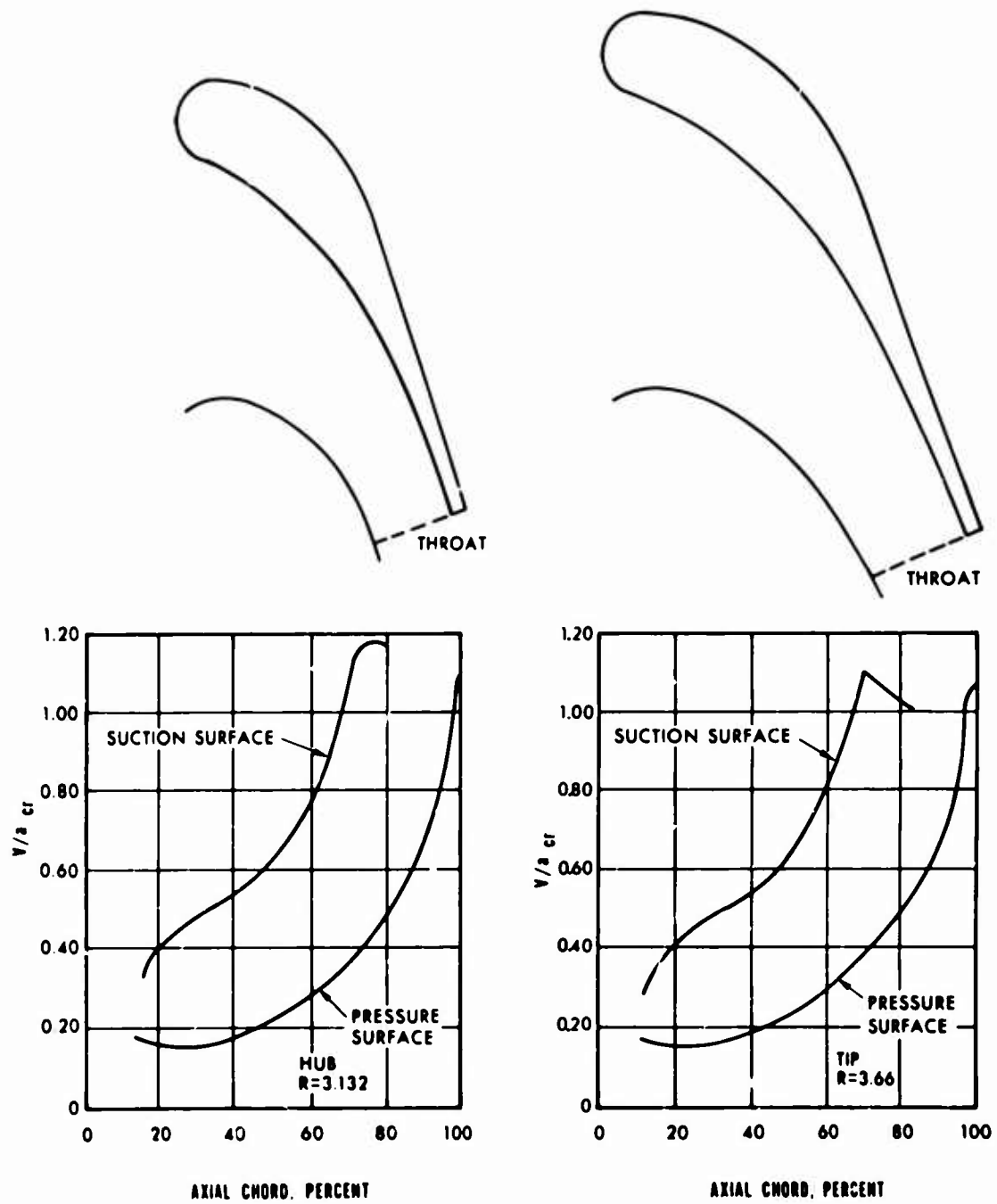
Figure 15. Vane Channel Velocity
Distribution.
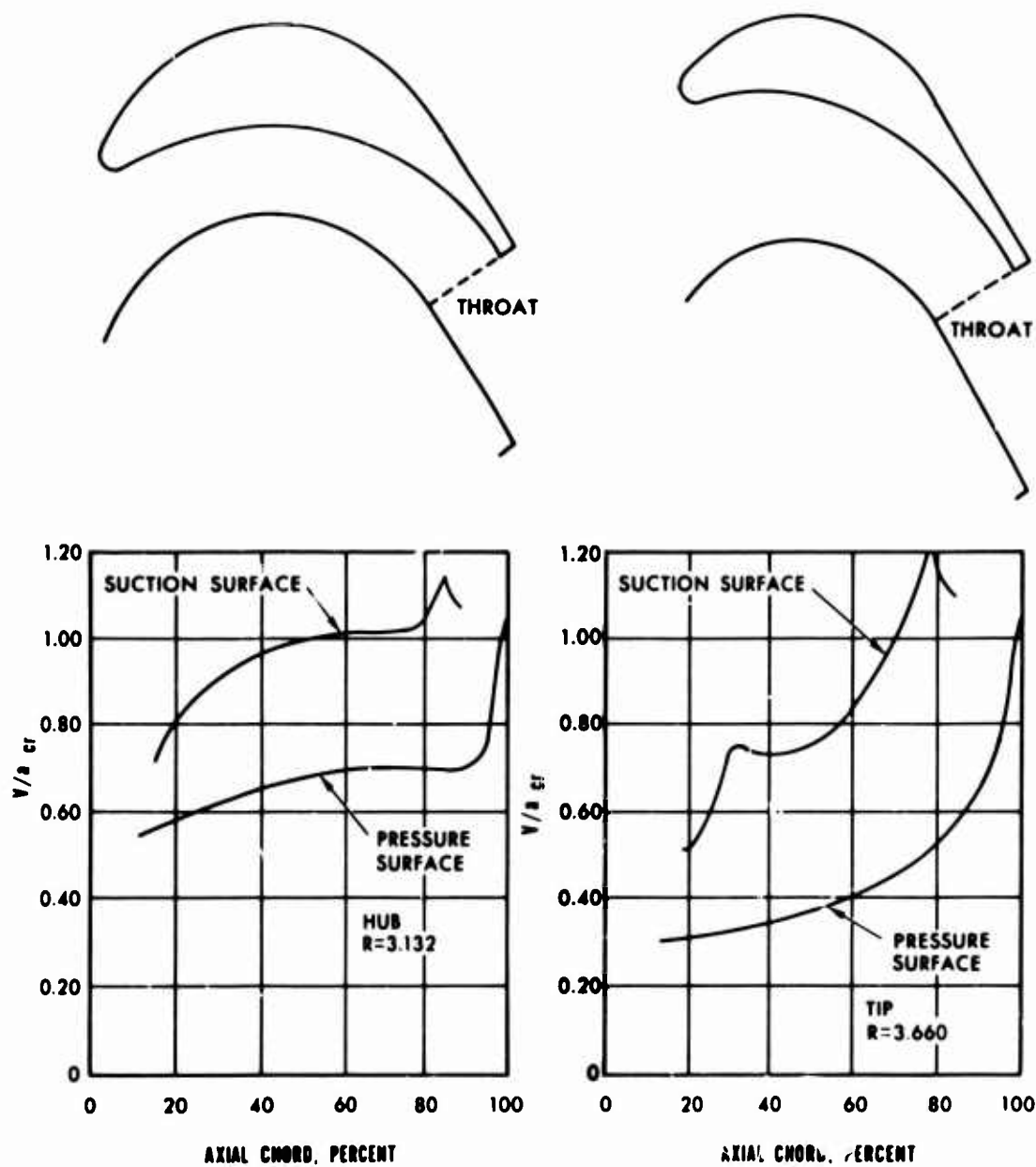
Figure 16. Blade Channel Velocity
Distribution.

2.2.2.2 Rotor

The rotor was designed to have 44 blades and a trailing-edge
thickness of 0.040 inch to accommodate the necessary internal
cooling passages. The resulting blockage ratio at the hub
section was also 0.16. The calculated blade channel velocity
distributions are presented in Figure 16. The hub section
provides a good approximation to the ideal rectangular blade
loading, having minimal suction-surface diffusion and a pres-
sure surface diffusion of 0.24. The tip section has a
slightly increased suction surface diffusion and a pressure
surface diffusion of 0.35. Allowable diffusion values of
0.55 or less were recommended. The surface diffusion is
then defined as

$$\text{Suction surface diffusion, } D_s = 1 - \frac{V_{exit}}{V_{max}} \tag{11}$$

$$\text{Pressure surface diffusion, } D_p = 1 - \frac{V_{min}}{V_{inlet}} \tag{12}$$

To minimize bending stresses in the rotor, the cylindrical
sections were stacked about a radial line passing through the
center of gravity of each section. The blade stacking is
complicated by the presence of the cooling passage--that is,
the design of the cooling passage is dependent on the blade
stacking, since this geometry controls the stresses within
the blade. However, the blade stacking without inclusion of
cooling passages was considered sufficiently accurate for
use in stress calculations required to define the blade at-
tachment concepts.

3. MECHANICAL DESIGN AND ANALYSIS

With the turbine annulus and blade shape defined by the aero-
thermodynamic design activity, the details of determining
feasible blade disk attachment concepts were considered.

While the optimization study indicated that a strut-supported
sheet metal blade--Configuration (a) of Figure 1- resulted in
the best SFC and sp hp combination, it should be immediately
clarified that the blade disk attachment concepts evaluated,
selected, and tested in this program were not restricted to
the use of such a blade design. Of the four blade configura-
tions that were considered in the optimization study, three
could be configured by cast/coring techniques. Though certain
variations in blade weight and, consequently, rotor size may
exist, the geometry of all four blade configurations is ap-
proximately common with respect to the blade pedestal and
cooling-air inlet passages. Therefore, a blade disk attach-
ment method determined to be suitable for any one config-
uration would be sufficient for any of the four.

However, since the optimization study did suggest use of the
strut-supported sheet metal blade, and since this design is
unconventional for rotating blades, a preliminary evaluation
of the joining problems associated with the shell/strut joint
was conducted. This evaluation was conducted in parallel with
the preliminary tests for blade/disk attachments and generally
differed only by material combinations. One exception was
that an evaluation of cast bonding was conducted for the shell/
strut application only.

3.1 MECHANICAL-DESIGN OBJECTIVES

Objectives of the mechanical-design activity were:

1. To further evaluate, modify if necessary, and
    finalize the rotor blade cooling geometry

2. To determine the complete turbine-rotor assembly
    metal-temperature profile

3. To determine the turbine rotor blade load and
    stress-rupture life

4. To select several feasible blade/disk attachment
    concepts for preliminary test evaluation

5. To establish the final turbine rotor designs for
    the three most promising blade/disk attachment
    concepts

38

In addition, a parallel activity (described in Section 4. FABRICATION TECHNOLOGY DEVELOPMENT) was undertaken to support and supplement the mechanical design and analysis. The goals of the parallel activity were:

1. To select several suitable material types for fabrication of the disk, cast/cored blade or strut, and sheet metal blade shell

2. To evaluate and determine by fabrication and joint-property preliminary-type testing the most advantageous material types and blade/disk attachment concepts (also to evaluate shell/strut attachment concepts)

3. To obtain potential joint-strength data that would aid in the design of the final test specimens and in the final turbine rotor designs

While compromising of several factors was involved in establishing the mechanical design, emphasis was placed upon evolving a design such that the rotor could be produced in production quantities at a reasonable cost.

Prior to initiating the mechanical design activity, an extensive literature survey was conducted and a survey of Government agencies was made to review existing blade attachment methods and joining processes that might be applicable to the subject design. Recent activities involving turbine blade attachments were found to be confined mostly to space applications and were not compatible with the subject-design requirements. However, considerable material describing various joining processes was found, some of which appeared to be feasible for use in blade attachment design concepts. A listing of pertinent material deduced during the literature survey is presented in the appendix.

3.2 FINAL DESIGN OF BLADE

For the design conditions under consideration, the optimization study of the aerothermodynamic design activity suggested that the optimum values of SFC and sp hp would be realized by utilization of vane cooling scheme Configuration (a), (Figure 2), and blade cooling scheme Configuration (a), (Figure 3). Details of the vane design will not be included in this report, since they have no direct bearing on the blade/disk attachment study.

As shown in Figure 3, the blade cooling scheme of Configuration (a) is a strut-supported sheet metal shell with radial flow in the leading-edge and centerbody regions, chordwise

flow in the tip region, and trailing-edge discharge. Coolant flows radially outward through passages formed by the strut and sheet metal, turns and flows chordwise in the tip region, flows radially inward in the trailing-edge region, and discharges uniformly through the trailing edge into the main gas stream.

Layout studies of various blade attachment concepts, combined with the radial-flow blade, indicated a serious problem in the definition of a coolant supply plenum in the pedestal region of the design. The prime reason for considering radial flow in the strut, as opposed to chordwise flow, is to eliminate parasitic loads inherent in the chordwise-flow configuration resulting from the non-load-carrying members, and hence, to reduce the blade root loading. To realize full load-carrying ability from the radial-flow "lands," these members must extend into the pedestal region and as a result would complicate the plenum configuration and root region of the sheet metal shell. In view of these complications as they relate to fabrication, it was decided to utilize a chordwise-flow blade configuration and accept the non-load-carrying penalty.

3.2.1 Final Cooling Configuration

The chordwise-flow concept is shown in Figure 17. Coolant flows from the central cavity of the strut through three slots in the nose and impinges against the inside surface of the leading edge. It then turns and flows chordwise along both the suction and the pressure sides in passages formed by the strut and sheet metal, and discharges uniformly through the trailing edge into the main gas stream.

The blade strut is an investment casting incorporating chordwise grooves on both suction and pressure sides for controlling coolant flow and incorporates coring to configure the internal air supply plenum. Impingement slots may be cored or may be machined by the electrical-discharge machining process. The strut is designed to eliminate a separate blade cap by extending the tip land to join the sheet metal, in both the leading-edge and the trailing-edge regions.

The outer sheet metal shell may be brazed, or with sufficient process development may be diffusion-bonded to the strut. Based upon fabrication experience, 0.010-inch-thick sheet metal was selected for the shell as offering the best compromise of the following design considerations:

1. Fabricability

2. Foreign-object damage

40

SHEET METAL SHELL

CORE AT TIP

CORE AT CRITICAL
RADIUS

0.120 0.040   ← 0.015

← 0.015 R

0.020

DIMENSIONS TYPICAL
EXCEPT AS NOTED

0.015

← 0.030

(CENTER HOLE) 0.140

← 0.015

CORE CONTOUR

CRITICAL RADIUS, 3.3 IN.
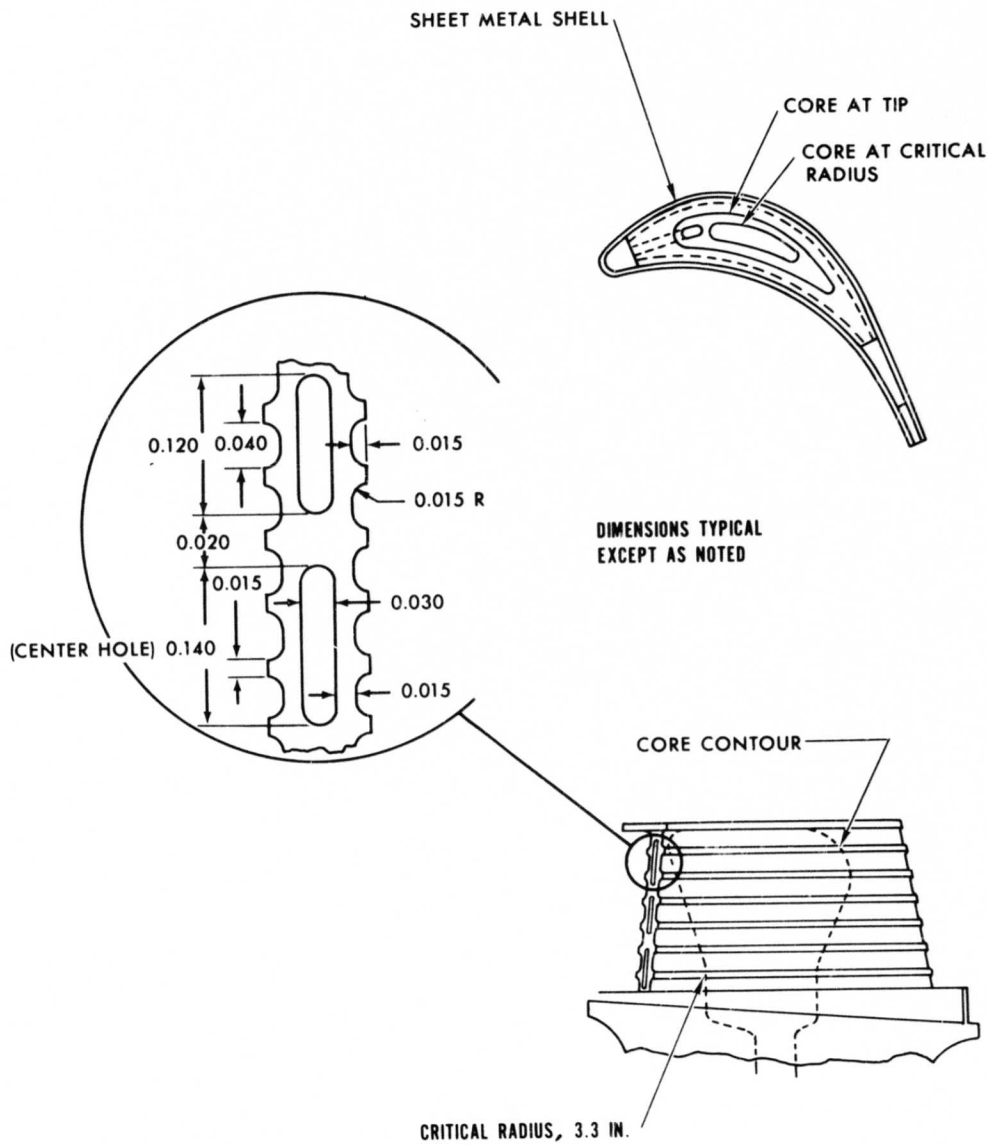
Figure 17.   Chordwise-Flow Blade Configuration.

41

3. Considerations of erosion from brazing

4. Damage in handling

5. Minimum trailing-edge thickness

The shell is supported in shear by the strut "lands" through-
out the mid-chord region. The leading-edge and trailing-edge
regions of the shell are supported in shear at the root land
only, with a portion of the load being transmitted back to
the center section of the strut. The trailing edge contains
a "wiggle strip," which serves to (a) control the coolant
discharge flow area and (b) join the trailing edges struc-
turally. The "wiggle strip," attached by brazing, is con-
figured from 0.004-inch sheet metal and provides flow passages
having the approximate shape of an equilateral triangle. The
resulting trailing-edge thickness is 0.040 inch.

The chordwise-flow design, compared to the radial-flow design,
has several advantages that are believed to more than com-
pensate for the parasitic load caused by the chordwise land
geometry:

1. The coolant supply route is much less complicated,
    and a large supply plenum in the blade attach-
    ment region is not required.

2. The sheet metal shell load may be distributed
    over a larger area, and no sheet metal blade cap
    is required.

3. The sheet metal temperature in the leading-edge
    region can be lowered to values similar to center-
    body region values, since impingement cooling
    has high cooling capacity (however, for the same
    centerbody metal temperature, the coolant flow
    rate must increase slightly).

4. Blade coolant flow-distribution problems are
    expected to be less severe both from a physical
    significance viewpoint and from a computational
    viewpoint.

3.2.2 Blade Heat-Transfer Analysis

An analysis of the strut and sheet metal shell was performed
to determine metal temperatures during steady-state operating
conditions. Transient heat-transfer analysis was not con-
sidered, since it is believed that steady-state conditions
sufficiently define the cooling-flow requirements for realis-
tic blade attachment design. This reasoning also applies to

heat-transfer analysis of the disk and attachment, discussed elsewhere in this section.

Blade metal temperatures based upon the aerodynamic optimization study coolant flow rates were computed for several chordwise locations at about one-third blade height. This location (at R = 3.3 inches) was determined to be the critical radius for the radial-flow strut-supported sheet metal blade concept. No adjustment was made in the critical radius to account for differences in critical radius between the radial-flow and chordwise-flow designs, since the net effect is considered small. The total coolant flow rate determined by the optimization study is 10.96 percent of the compressor discharge flow, of which 2.2 percent is utilized to cool the blades. The blade metal temperatures of the chordwise-flow scheme corresponding to these flow rates are shown in Figure 18.

The sheet metal temperature in the leading-edge region and just aft of the strut is relatively high. These temperatures could be decreased by modifying the coolant flow path and/or increasing the flow rate slightly. However, it was believed that these values provided a sufficient definition of the blade to result in realistic blade attachment designs, and no modifications to the cooling geometry were made. The gas temperature profile and estimated strut temperature variation with radius are shown in Figure 19.

3.2.3 Blade Stress Analysis

With the aid of the blade strut metal temperature distributions presented in Figure 19, the stress-rupture life in the blade was determined and the required strut cross-sectional area distribution was calculated and optimized to obtain maximum life consistent with the various boundary conditions and within the general capabilities of investment casting techniques. The cored center of the blade strut was tapered to reduce the loading at the critical location (r = 3.30 inches) and at the same time to provide the maximum possible load-supporting cross section at this location. In addition, the cored chordwise cooling-flow slots were designed to minimize the centrifugal loading for a given cooling-airflow area.

The stress analysis of the blade was performed with use of the following major considerations:

1. Only centrifugal stresses were calculated (gas bending stresses for this blade will be negligible).

43

T_c=1350 °F

1860 °F

1900 °F

T_c=1310 °F

T_c=1288 °F

SHEET METAL

1720 °F
1708°F
1664 °F
1655 °F
1649 °F

STRUT (T =1637 °F)

1680 °F
1665 °F
1629 °F
1618 °F
1611 °F

T_c=1059 °F

CRITICAL SECTION
(R=3.3 IN.)

T_c=1156 °F

1820 °F

1860 °F

1800 °F
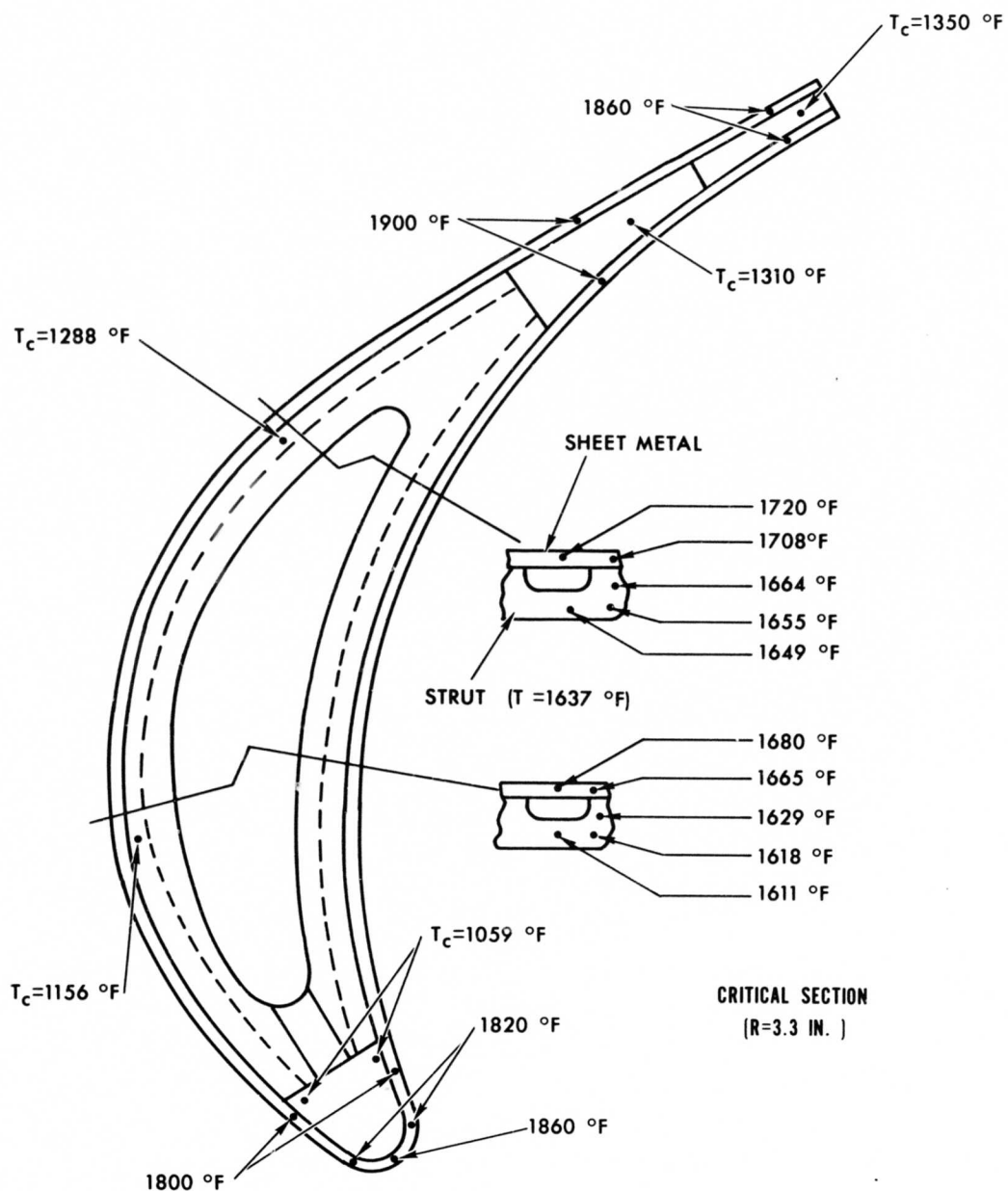
Figure 18.   Blade Metal Temperatures for
Chordwise Flow Configuration.

44

2. The centroids of the blade cross sections were assumed to lie in a radial line, thus minimizing centrifugal bending stresses in the blade.

3. The cast strut material was assumed to carry all of the load, and the shell loading was assumed to be uniformly distributed through each braze joint into the strut.

4. The cast strut material used was MAR-M 246, with a density of 0.305 lb per cubic inch.

5. The shell material used was assumed to have a nominal thickness of 0.010 inch and a density of 0.305 lb per cubic inch.

6. The mass of the braze material was neglected.

The resulting centrifugal stress distribution in the blade at design speed (46,900 rpm) is shown on Figure 20.
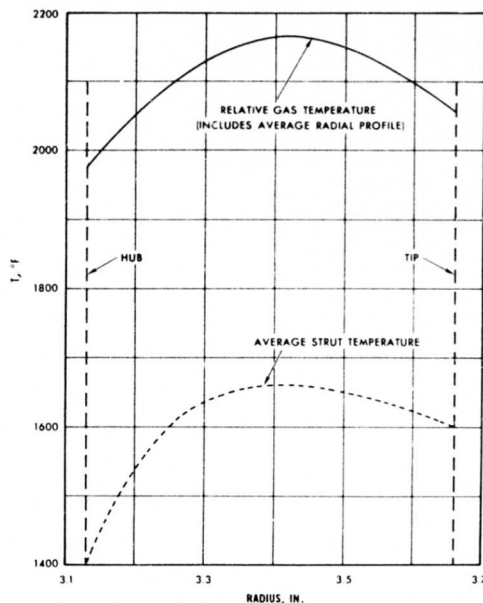
Figure 19. Gas Profile and Estimated Average Strut Temperature.
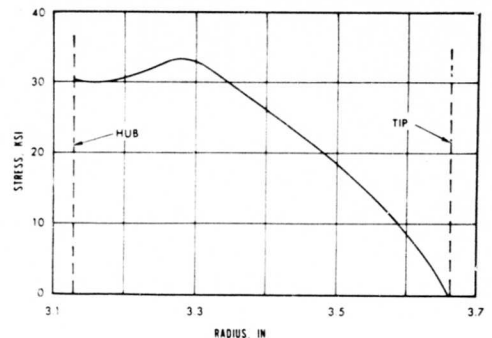
Figure 20. Centrifugal Stress Distribution of Blade.

There is insufficient MAR-M 246 rupture-strength data available to establish design minimum strength levels with any degree of confidence. However, a nominal rupture strength curve is shown on Figure 21 based on a limited amount of testing. Nominal IN-100 data corrected for density is also shown for comparison. The resulting nominal stress-rupture life for MAR-M 246 is shown on Figure 22. The minimum life of about 1800 hours occurs at a radius of approximately 3.3 inches. This exceeds the design objective of 1000 hours.

It is recognized that in any final detailed design analysis, the following additional work would be necessary to optimize the design:

1. Transient and steady-state thermal stresses in the blade at several radial stations would be calculated to determine the low-cycle fatigue life, critical location, and interaction with stress-rupture failure modes.
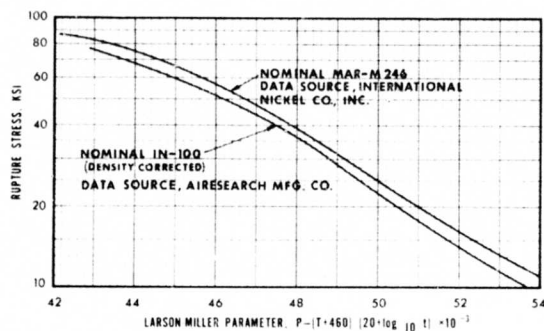
Figure 21. Comparison of MAR-M 246 and IN-100 Rupture Strength.
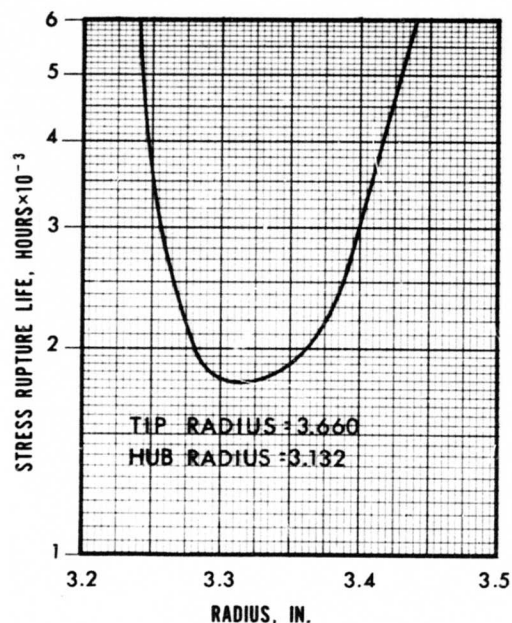
Figure 22. MAR-M 246 Stress-Rupture Life.

2.   The blade cross sections would be stacked on
     a radial line to minimize centrifugal bending
     stress in the blade.

3.3   BLADE/DISK ATTACHMENT CONCEPTS

Knowing the blade loads and design details of the blade and
blade coolant inlet flow passages provided the necessary in-
formation for design of blade attachment concepts. A number
of different methods were considered in an effort to find the
most feasible approach. The following basic criteria were
established for the methods under consideration:

1.   The joining method must attach 44 blade struts
     of cast nickel-base alloy such as MAR-M 246 to
     a disk forged of high-strength nickel-base
     alloy, similar to Waspaloy.

2.   The joint between the blade and the disk should
     be capable of nondestructive testing or inspec-
     tion techniques that would evaluate the sound-
     ness and reliability of the joint for its
     intended service.

3.   The joining technique should be economically
     feasible for normal production quantities.

4.   Strength properties of the joint should be
     sufficient to permit a practical design from
     the standpoints of weight, polar moment of
     inertia, and axial length.

5.   Geometry of the attachment must provide for
     transport of coolant to the blade without
     excessive leakage.

The following paragraphs are devoted to a discussion of
methods considered and give the design details of the selec-
ted attachment concepts. The ideas considered can be grouped
into several broad classifications such as:

1.   Mechanical concepts, which include axial fir trees,
     circumferential dovetails, and pin joints.

2.   Diffusion bonding.

3.   Brazing, primarily vacuum furnace brazing with
     nickel-base braze alloys.

47

4.   Welding, which includes electron beam, inertia, explosive, and laser beam.

3.3.1 Mechanical Concepts

Several mechanical attachment concepts were studied, including axial fir trees, circumferential dovetails, and pin joints. Of all concepts evaluated, the conventional axial fir-tree design promised the most reliable lightweight approach for the subject turbine design.

Pin-joint designs have been used for some compressor blade attachments and offer certain advantages, such as frictional damping of flexural blade vibrations. Because of the small hub diameter of the subject turbine design and the limited space available, it is necessary to put the pin in quadruple shear. In the design considered, the estimated average shear stress is approximately 70,000 psi; thus, a very high strength pin material, such as AF2-1DA, is required. Bending stresses in the pin were not estimated, but would be a major factor in any detailed analysis. Since the pin-joint design resulted in one of the heavier of the concepts studied, it was abandoned.

A circumferential dovetail design in which a split disk was utilized was also considered. In this type of design, very large bending stresses develop in the disk due to the blade loading, and large axial through-bolts are necessary to hold the disk halves together. It is inherently a heavy design and was dropped from further consideration.

Since no other mechanical attachment concepts appeared to be particularly encouraging, the major effort was expended on the axial fir tree. A preliminary design was made and analyzed, although no attempt was made to optimize the configuration, as would be required in a final detailed design analysis. The design selected was a two-lobe configuration. Figure 23 shows the basic design configuration.

Table VII shows a summary of the stresses calculated for the preliminary design, and Figure 23 gives the respective locations of these stresses. No allowance was made for the fact that a cooling-air passage equivalent to a 3/32-inch-diameter hole (0.0069 square inch) is required to feed each blade. This consideration would amount to a small increase to the blade tensile stress in the inner tang and outer tang.

The critical stresses--those most likely to cause failure--are the combined fillet stresses and the maximum combined fillet stresses. The combined fillet stress is the effective Heywood stress combining the tensile and bending stresses in the fillet region. The maximum combined stress includes the effect

48

TABLE VII. FIR-TREE STRESS SUMMARY				
Type of Stress	Blade Stresses, KSI			
	Outer Tang		Inner Tang	
	Nominal	Peak	Nominal	Peak
Tension	23.6	36.7	26.4	40.0
Bending	30.0	34.9	32.7	39.2
Comb. fillet	53.6	71.6	59.2	75.9
Max. comb. fillet	91.1	117.8	98.3	122.1
Shear	20.2	23.5	22.0	24.1
Bearing	41.4	48.1	47.0	51.5
Type of Stress	Disk Stresses, KSI			
	Outer Tang		Inner Tang	
	Nominal	Peak	Nominal	Peak
Tension	49.3	71.7	59.3	66.2
Bending	38.7	45.0	39.6	43.4
Comb. fillet	87.6	116.1	98.5	109.2
Max. comb. fillet	162.9	207.1	202.0	220.0
Shear	16.7	19.4	19.8	21.7
Bearing	41.4	48.1	47.0	51.5

NOTE: Refer to Figure 23 for location of stresses.

NOMINAL STRESSES OCCUR AT POINTS
5 AND 6, WHEREAS PEAK STRESSES
OCCUR AT POINTS 2 AND 4 DUE TO
BROACH ANGLE α

BLADE

SECTION A-A

BLADE PEDESTALS

OUTER TANG
OF FIR TREE

INNER TANG
OF FIR TREE

DISK

OUTER TANG OF DISK
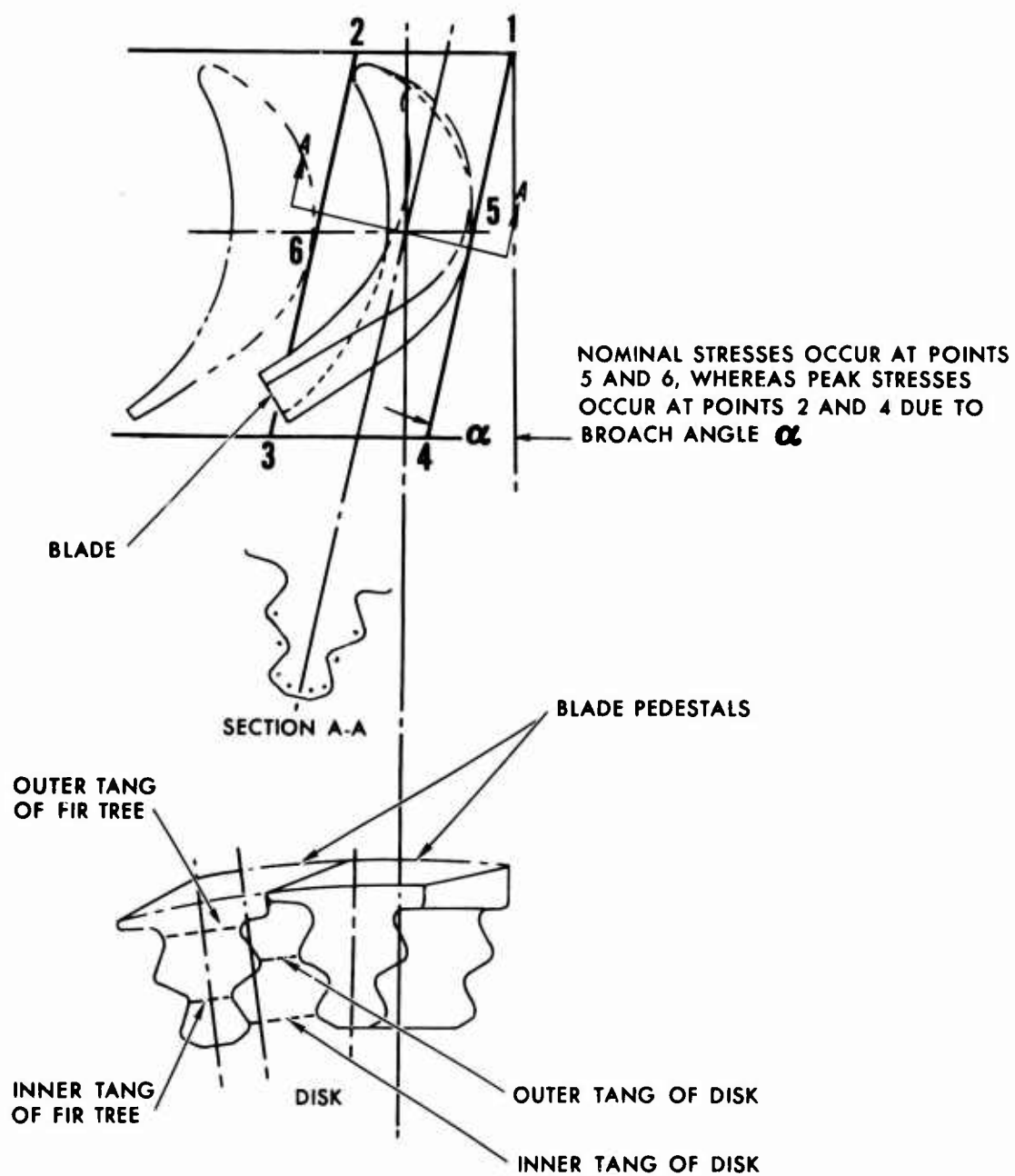
INNER TANG OF DISK

Figure 23.   Stress Locations of Fir-Tree Disk
Attachment Design.

50

of both tensile and bending stress concentration factors.
The combined fillet stress is compared with the allowable
rupture strength of the material, and the maximum combined
fillet stress is compared with the low-cycle fatigue strength
of the material.

Although no heat-transfer calculations of disk steady-state
temperatures were made for this design, a reasonable estimate
based on experience with similar designs would indicate a
metal temperature of 1300° to 1350°F at the disk rim. Typical
gradients in the radial direction are 500° to 700°F per inch,
and the temperature drop from blade to disk is usually about
50°F at a given radius. These assumptions and the use of
MAR-M 246 castings for the blades and Astroloy forgings for
the disk permitted calculation of the safety margins shown in
Table VIII.

Allowable stresses (creep-rupture and low-cycle fatigue) for
the MAR-M 246 were assumed to be the same as for IN-100, since
there is insufficient data available to establish realistic
minimums. In the absence of available data for Astroloy, it
was assumed that the low-cycle fatigue strength is comparable
to that for Waspaloy.

It is apparent from Table VIII that negative margins of safety
exist in the disk, the worst being due to the combined fillet
stress at the outer tang. This is primarily due to the large
tensile stress there. There is very little that can be done
to improve this situation, since the axial length of the fir
tree is the full chord length of the blade. Larger axial
dimensions would only necessitate a larger disk to carry the
load. In view of the prohibitive stress factors, the mechani-
cal attachment evaluation was discontinued. Further investi-
gation was confined to brazing, welding, and diffusion-bonding
techniques.

3.3.2   Diffusion Bonding

As found in the literature survey, recent research efforts
have been conducted to develop methods of solid-state diffu-
sion bonding. These methods all depend on the effects of
pressure, temperature, and time at the joint interface. The
success of the diffusion-bonded joint concept depends strongly
on the ability to maintain intimate contact between very smooth
surfaces during the bonding operation. Methods have been
pursued in an effort to eliminate the need for precisely mated
surfaces and to relax the requirements of surface finish.

51

Location	Stress Type	Estimated Temperature (°F)	Allowable* Stress (KSI)	Peak Stress	M.S.**
Blade outer (MAR-M 246)	Comb. fillet	1300	79.0	71.6	+0.10
	Max. comb. fillet	1300	140.0	117.8	+0.19
Blade inner (MAR-M 246)	Comb. fillet	1200	93.0	75.9	+0.22
	Max. comb. fillet	1200	140.0	122.1	+0.14
Disk outer (Astroloy)	Comb. fillet	1200	100.0	116.1	-0.14
	Max. comb. fillet	1200	205.0	207.1	-0.01
Disk inner (Astroloy)	Comb. fillet	1100	116.0	109.2	+0.06
	Max. comb. fillet	1100	205.0	220.0	-0.07

TABLE VIII. SUMMARY OF SAFETY MARGINS

*Based on 1000-hr stress-rupture strength or 0.2 percent offset yield strength for combination fillet stress and 1000-cycle strength for maximum combination fillet stress.

$$**M.S. = \frac{\text{allowable stress}}{\text{peak stress}} - 1$$

The gas pressure bonding process, which has been developed extensively at Battelle Memorial Institute, provides an isostatic load application and for certain joint geometry, allows the relaxation of surface mating conditions. This is accomplished wherein at least one of the joint elements has compliance under application of the bonding parameters and thus conforms to the mating surface.

The use of interface diffusion aids with certain material combinations shows promise of obtaining higher joint strengths for a given surface condition, or alternatively permits a less precise surface finish for realization of a given joint strength.

In view of these recent advances in technology, the diffusion bonding technique was selected as a candidate joining method. Prior to the preliminary test evaluations of Section 4.2, analyses were performed to determine the temperature distribution and stress levels of a diffusion-bonded rotor design, as reported in Section 3.4.

Figure 24 shows the most attractive concept of those studied for diffusion bonding. Although other lighter weight concepts were considered, this design was chosen because of the ideal geometry that it provides for fixturing and for applying the bonding load. Concepts utilizing diffusion bonding, wherein the load is applied in a direction other than axial, are inherently deficient in bond area and, in the case of a radially applied load, are probably incapable of supporting the required bonding load through the blade and/or pedestal. The chosen concept may be subjected to loads that produce small deformation, if required for bonding strength, without affecting the integrity of the rotor design.

To reduce stress concentration in the rim region, holes and slots are provided as for the other attachment designs. The blade pedestal extensions are spaced 0.003 to 0.005 inch apart during bonding. The disk halves are considered to be slotted and have holes drilled prior to bonding for ease of machining and to provide compliance between disk and blade elements. If bonding load is applied mechanically, it is believed that all blade pedestal extensions must be ground with a common set-up in order to provide for uniform loading of elements during bonding. If gas pressure bonding were utilized, the compliance offered by the slots and holes could allow small variations in the blade pedestal extension dimensions without affecting the bonding characteristics appreciably from blade to blade.

SEQUENCE OF WHEEL
ASSEMBLY VIEWS

COMPONENTS PRIOR
TO DIFFUSION
BONDING

7.32 DIA.
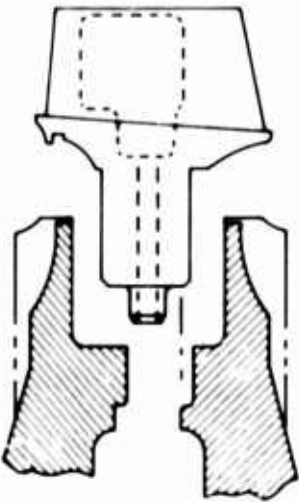
DISC JOINT SURFACES
FINISH MACHINED
AND COMPONENTS
DIFFUSION BONDED

WHEEL ASSEMBLY
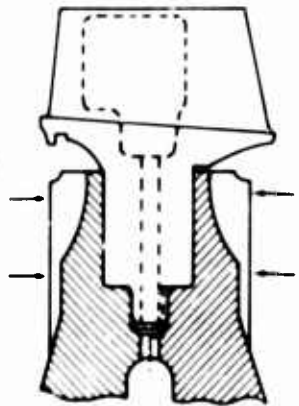
HOLES MACHINED, DISC
FINISH MACHINED AND
SEGMENTED AIR SEAL
INSTALLED

Figure 24.   Diffusion-Bonded Design.

54

Advantages and disadvantages of this design are:

1. Advantages

    (a) Because of the parallel-sided bond surface
        design, fixturing and surface preparation
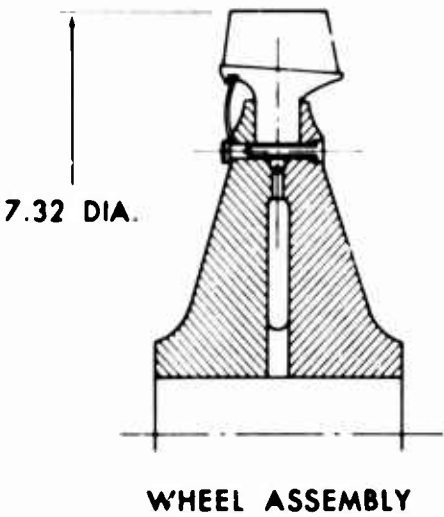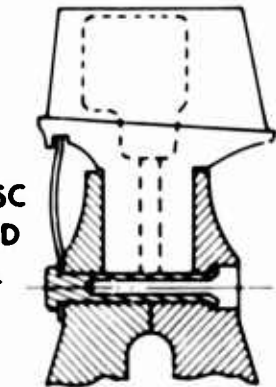   are simple and easy to control.

    (b) Analysis of the joint is simple, since it
        is in pure shear.

    (c) Cooling-air access is simple, since each
        blade can be cored completely prior to
        joining.

2. Disadvantages

    (a) Inspection is difficult, since X-ray,
        ultrasonic, and other nondestructive
        techniques cannot adequately define areas
        of incomplete bonding. Whirlpit testing
        can be used to discover gross defects in
        the bond, but will not reveal the small
        stress concentrations that affect low-
        cycle fatigue behavior and stress-rupture
        life.

    (b) The disk must be slotted and drilled at
        the inner boundary of the joint to prevent
        low-cycle fatigue failures in disk rims.

    (c) The design is relatively heavy.

    (d) To ensure uniform bonding, blade elements
        may have to be ground in matched sets.

The design of a turbine rotor that incorporates the diffusion
bonding attachment concept is described in Section 3.4.

3.3.3   Brazing

Brazing of nickel-base alloys for high-temperature operation
has long been used for static structures such as gas turbine
stators, bearing support frames, and other parts. However,
its use for highly stressed rotor parts has been virtually
nil due to the low rupture-strength and fatigue-strength
properties in most joint designs. Over the past few years,
however, reliable joints have been made with vacuum brazing
techniques with the use of new brazing alloys and close con-
trol of the process variables.

55

Preliminary calculations based upon joint properties reported in the literature and approximate attachment geometry suggested that a satisfactory attachment could be designed with the use of a brazed joint. Thus, brazing was selected as one of the candidate joining techniques. Prior to the preliminary test evaluations of Section 4.2, analyses were performed to determine the temperature distribution and stress levels of a brazed rotor design, as reported in Section 3.4.

The brazed-joint design selected is shown on Figure 25. This design was chosen since it best provides the large joint area required, and additionally provides a natural radius between each blade to mitigate the stress concentration effect at the rim of the disk. The design concept utilizes a split disk, which is joined by electron-beam welding. The depth of this weld is minimized by machining a 0.300-inch-deep groove in the periphery of the disk prior to welding. The bottom of this groove then becomes the maximum diameter of the welded surface. After final machining of the disk, this groove divides the surfaces to be brazed into four separate and essentially equal areas. This has the desirable effect of providing smaller areas over which the alloy must flow, and as such, should reduce the possibility of incomplete bonds due to incomplete wetting of the surfaces. Additionally, this groove simplifies the coolant entry path to the blade. Coring in the blade pedestal may be designed to provide a passage having considerable overlap over the disk groove, and therefore, would require less precise positioning, so that a certain amount of core shift could be tolerated. Coolant enters the groove through holes drilled in each disk attachment projection.

The blade pedestals have thin webs cast at each end, which prevent bypass flow of the working fluid through the cavities between blades. A small gap (0.003 to 0.005 inch) is allowed to exist between each pedestal to prevent undesirable loading from thermal-growth effects. The design shown on Figure 25 would allow excessive leakage at both root and tip of the disk attachment projections. These regions were left undefined because of the uncertainty of fillet effects from excess braze alloy. Sealing of these regions could be resolved by further development.

Advantages and disadvantages of this concert are:

1. Advantages

   (a) The joining process is inherently simple.

56

SECTION B-B
COMPONENTS PRIOR TO BRAZE
(DISCS JOINED BY ELECTRON BEAM WELD)

SLOTS MACHINED AND COOLANT
PASSAGES DRILLED
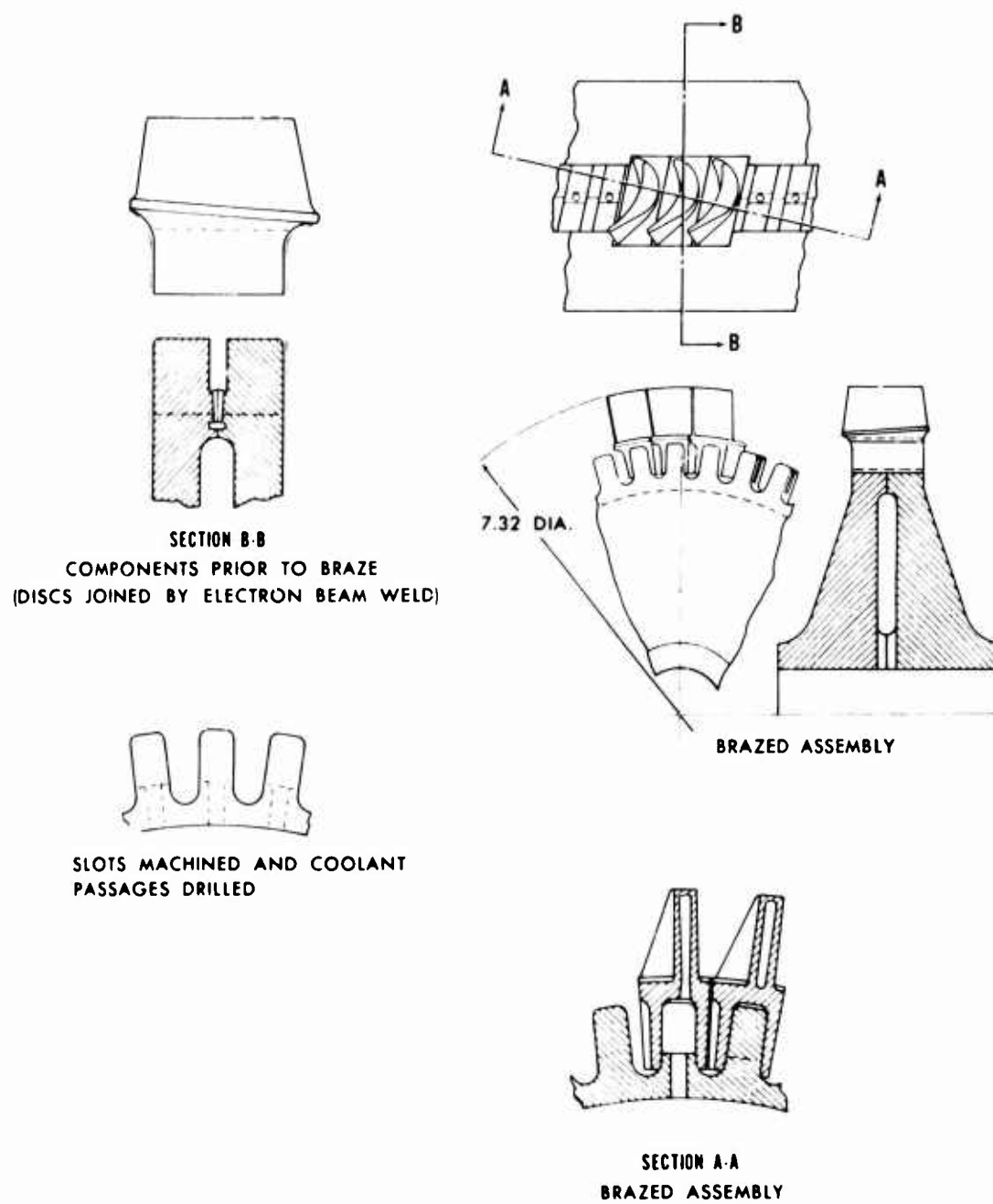
7.32 DIA.

BRAZED ASSEMBLY

SECTION A-A
BRAZED ASSEMBLY

Figure 25. Brazed-Joint Design.

(b)   The brazed joint is in pure shear, which eliminates the "peeling" effect that is inherent with many brazed designs.

(c)   Machining of the attachment on both blade and disk is simplified because of the parallel joining surfaces, and close dimensional control of the braze gap should be feasible at minimum cost.

2.   Disadvantages

(a)   The discovery of small voids and areas that would result in stress concentrations in the joint is not feasible by nondestructive inspection methods such as X-ray and fluorescent-penetrant.

(b)   A relatively heavy disk is required.

The design of a turbine rotor that incorporates the brazed attachment concept is described in Section 3.4.

3.3.4   Electron-Beam Weld

An examination was conducted to evaluate welding processes for use as a joining method in the blade/disk attachment. Of the welding processes evaluated, (electron beam, inertia, explosive, and laser beam), the electron-beam-welding process was considered to be the most effective and was the process selected for use in this program. Reasons for this selection were:

1.   More experience has been obtained on the joining of nickel-base alloys with use of electron-beam welding than for other applicable welding processes.

2.   Less heat input is generated to the welded assembly by electron-beam welding than by other applicable welding processes. This provides an important advantage in minimal distortion, and minimized weld joint cracking should also be obtained.

3.   The minimized weld zone produced by the electron-beam-welding process facilitates joint inspection by radiographic techniques.

4.   Fixturing requirements for the pre-weld assembly are relatively simple in comparison to those required for other applicable welding processes.

58

5.   A considerable amount of experience has been
     accumulated in recent years with the electron-
     beam welding of components having geometry
   similar to that of the turbine rotor designed
     for this program.

Prior to the preliminary test evaluations of Section 4.2,
analyses were performed to determine the temperature distri-
bution and stress levels of an electron-beam-welded rotor
design, as reported in Section 3.4. The electron-beam-
welding concept selected is illustrated in Figure 26.   The
disk halves are first joined by a girth weld.   Then with the
disk and blade pedestals in the premachined condition, the
blades are fixtured around the periphery of the disk and
spaced 0.003 to 0.005 inch apart. A single pass full-
penetration (0.79-inch), circumferential weld is then made.
The disk faces are then finish-machined (0.050-inch cleanup
at weld), and holes are drilled in line with the slots
between blades and centered on the weld.   These holes thus
remove weld flash at the space between blades and reduce the
stress concentration in the same fashion as on integrally
cast wheels.   Bypass of the main gas flow through the holes
is prevented by sealing each hole with a rivet.   The 0.003
to 0.005-inch slots remaining in the disk rim allow only
negligible bypass leakage and are considered to be sufficient
to prevent bending or compressive stresses from developing as
a result of mechanical interference induced by thermal tran-
sients.

This concept facilitates inspection of the weld by providing
a section through the weld zone on both sides and on each end
of each blade attachment.   Flaws in the weld and/or heat-
affected zone are easily detected by fluorescent-penetrant
inspections.

Use of the split-disk design provides a simple flow path for
the blade cooling air from the shaft.   For the blade cooling
scheme utilized in this assembly, the relatively large cored
cavity in the blade permits insertion of electrical-discharge-
machining tooling through the tip of the blade so that a pas-
sage may be machined to connect the cored blade cavity and
the disk cavity and thus complete the cooling-flow circuit.

SEQUENCE OF WHEEL
ASSEMBLY VIEWS

COMPONENTS PRIOR
TO WELD
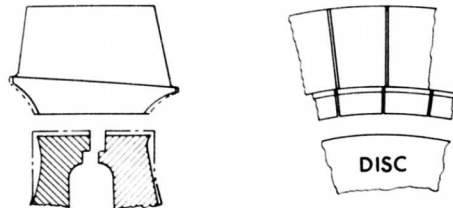
DISC

DISCS JOINED BY
GIRTH WELD AND
FINISH MACHINED
PRIOR TO BLADE
ATTACHMENT
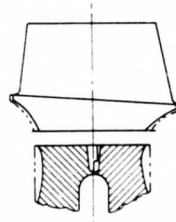
7.32 DIA.

WHEEL ASSEMBLY

BLADES JOINED
TO DISC BY
CIRCUMFERENTIAL
WELD

RIM HOLES MACHINED,
RIVETS INSTALLED, AND
COOLING-AIR PASSAGES
ELECTRICAL-DISCHARGE
MACHINED
DISC FINISH MACHINED
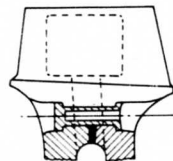
Figure 26.   Electron–Beam–Welded Design.

60

Advantages and disadvantages of this concept are:

1. Advantages

    (a) Fit of blades and disks prior to welding
        is easy to obtain.
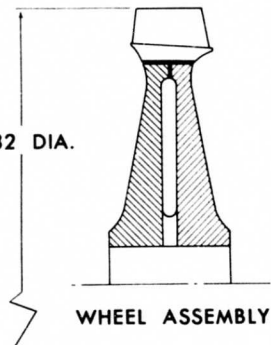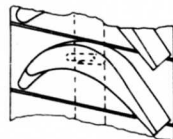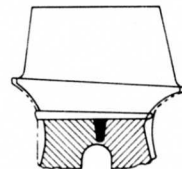
    (b) Analysis of the joint is simple, since
        the weld is in pure tension.

    (c) Inspection of the joint by X-ray with
        a single film exposure, plus a fluorescent-
        penetrant inspection of all four sides of
        each blade attachment, ensures quality
        control.

    (d) Weld joint strength is potentially
        equal to that of the weakest member being
        joined.

    (e) Past experience with use of similar
        design configurations for the blade
        pedestals was successful.

2. Disadvantages

        Access of cooling air is difficult to
        obtain, since the weld must be opened
        by inserting an Elox tool through each
        blade core.

The design of a turbine rotor that incorporates the electron
beam welding attachment concept is described in the following
section.

3.4 TURBINE ROTOR DESIGN

Three rotor designs were selected for evaluation with
diffusion-bonding, brazing, and electron-beam-welding attach-
ment methods to a split disk. The split-disk approach offers
an ideal method of supplying cooling air to the blades. For
each design, the attachment cross sections were designed to
minimize the radial load on the disks while maintaining the
design stress level in the joint.

61

3.4.1 Rotor Temperature Distribution

Rotor temperature distributions were computed for the three selected rotor designs. The analytical model for each design was an equivalent disk with accurate geometric approximations for the attachment area, blade strut area, and blade pedestal. At the time of this analysis, the disk contour and thickness were not yet defined. For this reason, a common typical disk design was used for each of the three design configurations analyzed. The isotherms were not corrected to the final disk shapes, since the effect on the attachment temperature is considered to be insignificant.

Neglecting the disks, the three design configurations differ primarily in the blade/disk attachment region. Therefore, the analytical models also differed primarily in the blade attachment region to obtain a valid approximation for the particular geometry under consideration. The analysis for each design configuration was two-dimensional (axial and radial); thus, the small circumferential temperature variations in the attachment region were not considered. This axisymmetric geometric assumption is not considered an analysis deficiency, since all geometric characteristics and blade coolant channels are accurately approximated with the equivalent axisymmetric disk analytical model.

Rotor isotherms for diffusion-bonded, brazed, and electron-beam-welded design configurations are shown in Figures 27, 28, and 29, respectively. General observations for all three isotherm patterns are similar. At small radii, rotor temperatures are only slightly above cooling-air inlet temperature, which was assumed to be 800°F. As radius increases, both rotor temperature level and temperature gradient increase, as can be expected. The strut isotherms agree with the strut temperatures presented in Section 2.

The coolant flow rates shown correspond to the disk pumping and blade coolant flow rates defined in the trade-off study. All three analyses included a heat balance on each of these cooling flows. Disk film coefficients were computed from conventional rotating disk heat-transfer correlations.
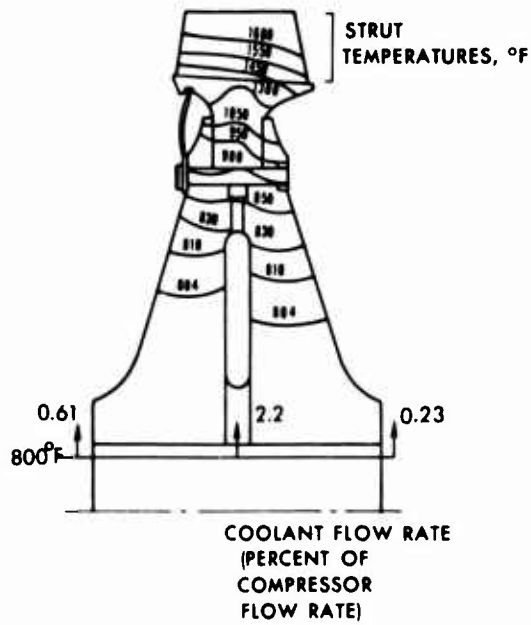
Figure 27.   Rotor Isotherms,
             Diffusion-
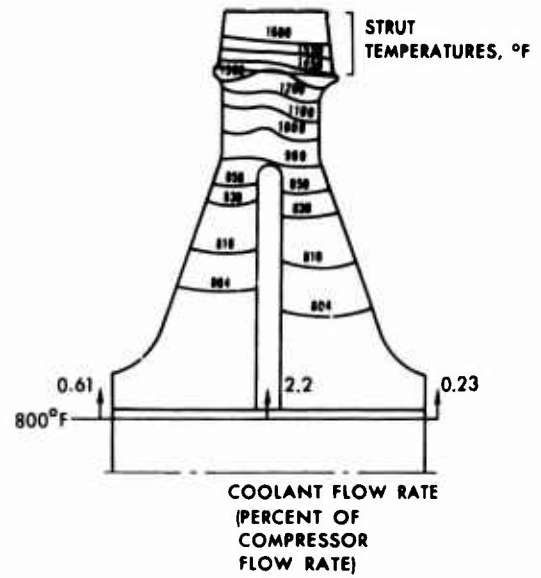   Bonded Design.
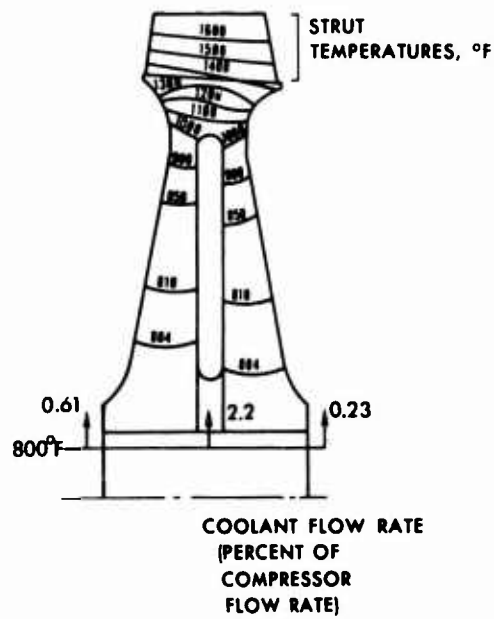

Figure 28.   Rotor Isotherms,
             Brazed Design.

Figure 29.   Rotor Isotherms,
             Electron-Beam-
             Welded Design.

63

3.4.2 Stress Analysis

The radial stresses in the attachment region were calculated as if the centroids of the sections lie on a radial line. Use of this approach minimized the centrifugal bending stresses. The nominal centrifugal stress distributions for each design are shown on Figures 30, 31, and 32, together with the disk stresses. The peak stresses in the electron-beam-welded design and diffusion-bonded design occur at the center of the rivet holes, whereas the radial stress in the brazed-joint design peaks at the root of the joint. The radial rim stress at the disk boundary is seen to be 60,000 psi for both the brazed-joint design and the diffusion-bonded design. The radial rim stress for the electron-beam-welded design is only 38,000 psi.

In each design configuration, the governing factor is the design stress level in the joint. These were chosen to be:

Diffusion bond	35,000 psi (shear)	MAR-M 246 to INCO 718
Braze	17,500 psi (shear)	MAR-M 246 to Waspaloy
Electron-beam weld	58,000 psi (tension)	MAR-M 246 to Waspaloy

The choice of these stress levels was based primarily on the results obtained from preliminary test evaluations modified by an estimate of changes expected in the final test results. The values used for design reflect not only the mean strength levels determined, but also the spread or variance observed.

At this time, a rotating disk design computer program, based on the work of Monson,[6] was used to determine the thickness of the split-disk designs. This program uses a plane stress analysis to determine the optimum disk thickness distribution that satisfies the desired equivalent stress distribution (based on the maximum strain energy of distortion theory) for the radial temperature gradient and radial rim loading imposed. A bore diameter of 1.0 inch was arbitrarily selected for the study.

64
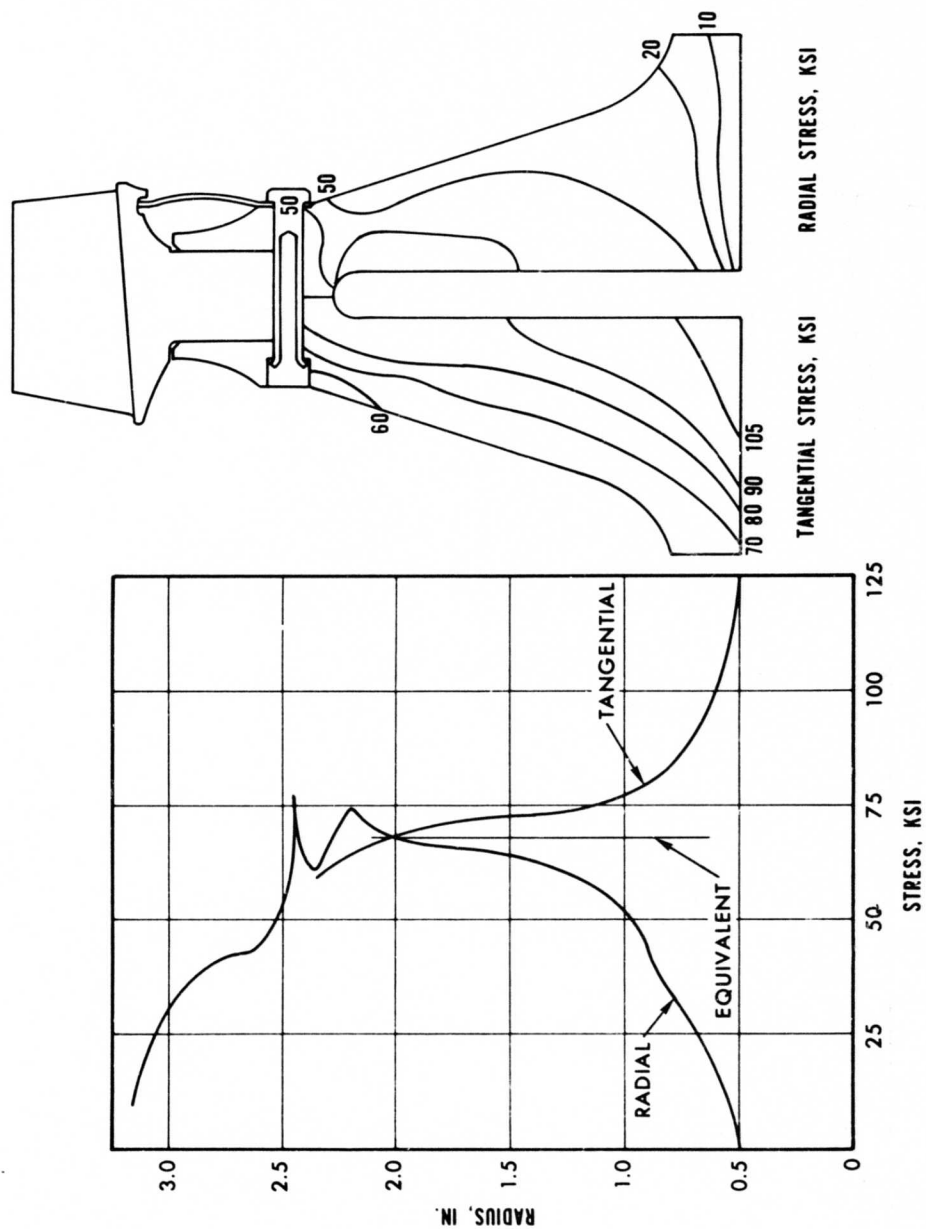
Figure 30. Nominal Centrifugal Stress Distribution
for Diffusion-Bonded Design.

65
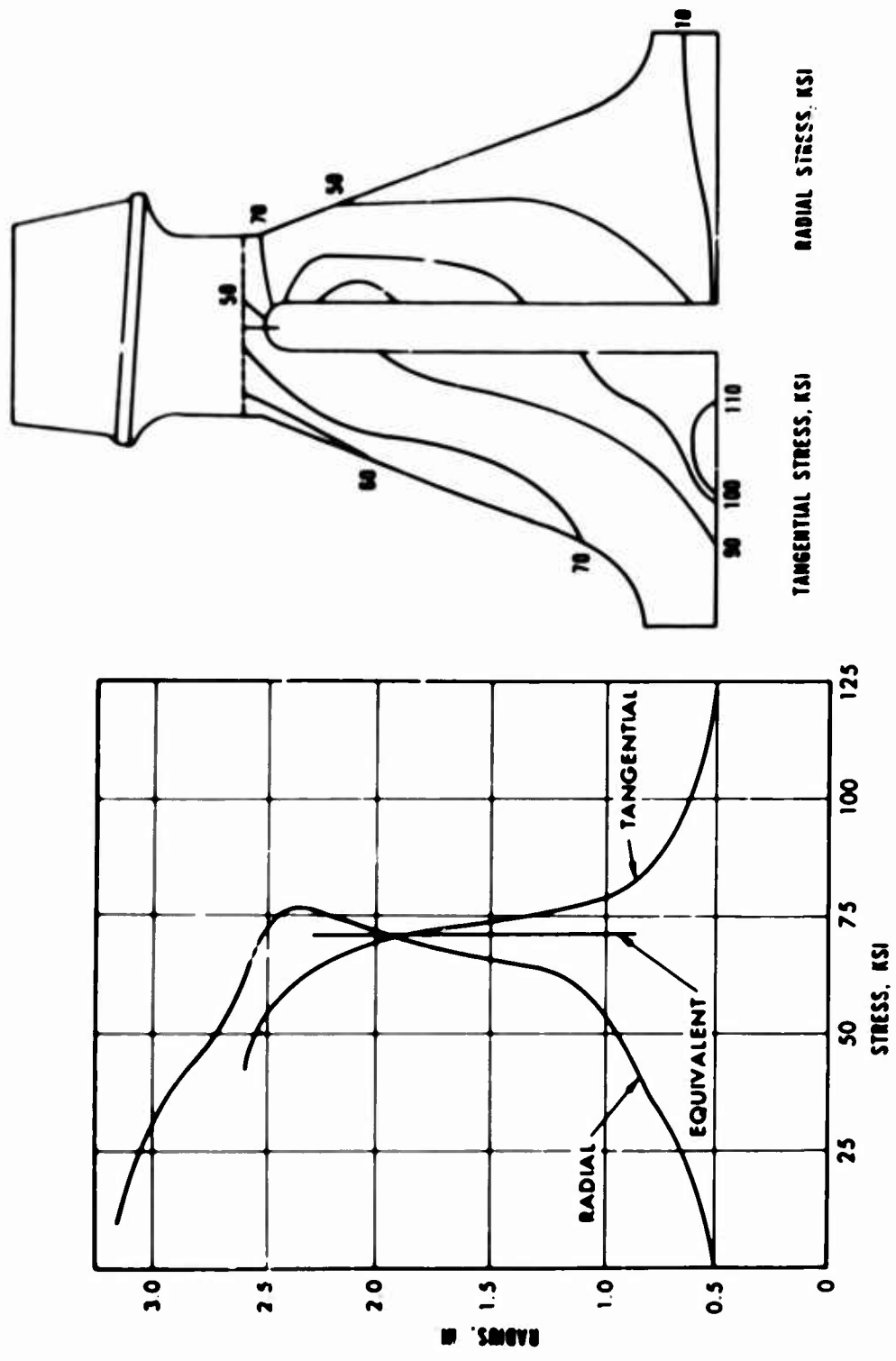
Figure 31. Nominal Centrifugal Stress Distribution
for Brazed-Joint Design.
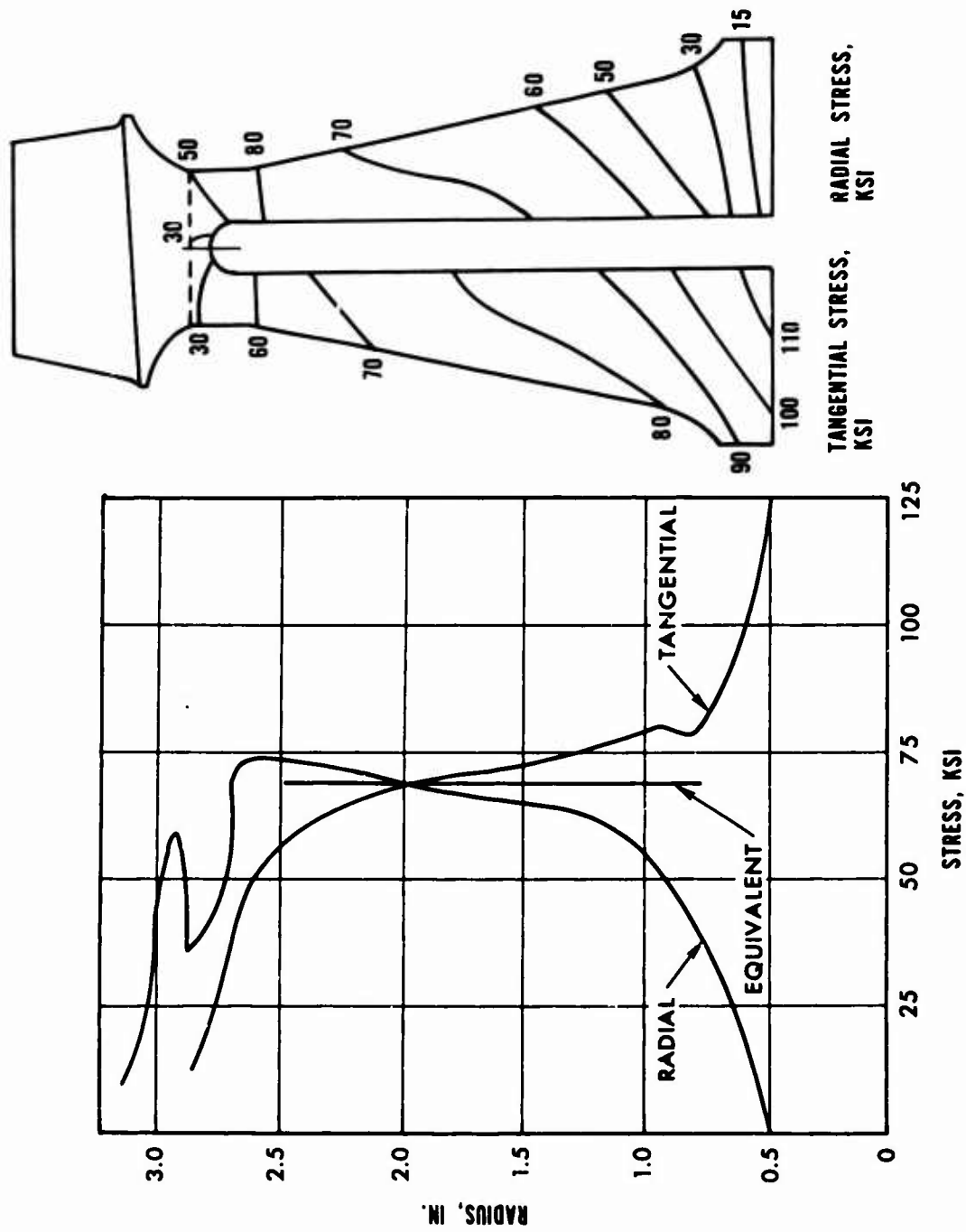
Figure 32. Nominal Centrifugal Stress Distribution
for Electron-Beam-Welded Design.

The allowable stresses at design speed (46,900 rpm) used for the analysis were based on the following criteria:

1. Except at the bore, all equivalent stresses based on the maximum energy of distortion theory of failure were not to exceed the lowest value determined from

    (a) 77 percent of the minimum* 0.2-percent offset yield strength.

    (b) 100 percent of the minimum stress-rupture strength of the material at twice the required overhaul life (2 x 1000, or 2000 hours).

2. At the bore, the tangential stress could not exceed 125 percent of the minimum 0.2-percent offset yield strength.

3. The average tangential stress in the disk could not exceed a value calculated to provide a minimum disk burst speed of 125 percent. This is obtained from the following relationship:

$$N_B/N_D = \sqrt{\frac{F_{tu}}{\sigma_t}} \quad \text{(burst factor)} \qquad (13)$$

where N_B = burst speed

  N_D = design speed

  F_{tu} = average ultimate tensile strength of disk material

  σ_t = average tangential stress at design speed

4. The burst factor is determined from burst tests of similar disk designs of the same material.

---

*All minimum-strength values are taken as three standard deviations below nominal.

From the radial loading and radial temperature gradients used, it became apparent that the average tangential stress in the disk (burst-speed criteria) governs the design rather than the equivalent stress in the disk.

Each of the three disk designs was analyzed by a finite-element computer program to determine the three-dimensional stress and deflection of each element. The radial and tangential stress distributions from this analysis are also shown in Figures 30, 31, and 32. The weights, polar moments of inertia, and bore widths for the three designs are compared in Table IX.

It can be seen from the data presented in Table IX that the electron-beam-welded design is by far the lightest and has the lowest polar moment of inertia. The diffusion-bonded design appears superior to the brazed-joint design in this regard. However, the brazed-joint design stress levels selected may be subject to change in some cases as a result of the final test data.

TABLE IX. WEIGHTS, POLAR MOMENTS OF INERTIA, AND BORE WIDTHS FOR THE THREE ROTOR DESIGNS				
Design	Airfoils (44)	Attachment (44)	Disk	Total
Electron Beam				
Weight, lb	0.67	1.63	5.02	7.32
I_p, lb-in-sec^2	0.0202	0.038	0.0448	0.1030
Axial width, in.			1.60	
Diffusion Bond				
Weight, lb	0.67	3.17	5.73	9.57
I_p, lb-in-sec^2	0.0202	0.062	0.0358	0.1190
Axial width, in.			2.20	
Braze Joint				
Weight, lb	0.67	3.28	6.93	10.88
I_p, lb-in-sec^2	0.0202	0.0705	0.0507	0.1414
Axial width, in.			2.60	

4. FABRICATION TECHNOLOGY DEVELOPMENT

This section describes a fabrication technology development effort that was conducted in parallel with the mechanical design and analyses described in Section 3. The objectives of this parallel activity were:

1. To select several suitable material types that could be utilized for fabrication of a disk, cast/cored blade or strut, and sheet metal blade shell.

2. To conduct preliminary testing in order to determine the most advantageous material types and blade/disk joining methods **and to evaluate** shell/strut joining methods.

3. To obtain potential joint-strength data that would aid in the design and fabrication of the final test specimens and in the design of the turbine rotors.

As stated in the introductory remarks of Section 3, even though this program was directed toward development of blade/disk attachment methods, some consideration was given to shell/strut joining, since the aerodynamic optimization study suggested the use of a strut-supported sheet metal blade. Therefore, preliminary testing was conducted to evaluate both the blade/disk and shell/strut attachments.

It should be noted that in the text of this section, all references to the strut or strut/disk attachment are directly applicable to a cast/cored blade or blade/disk attachment. A cast/cored counterpart of the subject sheet metal blade may result in (a) a slight increase in total blade weight, and (b) for the same coolant flow rate, a slight increase in metal temperature compared to that of the subject sheet-metal-blade supporting strut. For the same attachment configuration, these minor differences compound to reduce stress-rupture life in the attachment by (a) increasing the attachment metal temperature and (b) increasing the stress in the attachment to carry the additional blade load. For the same stress-rupture life, the rotor assembly would increase in size. However, the technology gained from the material selection evaluations and preliminary attachment test data for the sheet-metal-blade supporting strut is directly applicable to the fabrication and disk attachment of a cast/cored blade.

71

4.1 SELECTION OF MATERIALS

An investigation was conducted to select suitable materials for fabrication of the disk, strut, and sheet metal blade. The primary consideration for the disk material was adequate tensile strength up to 1200°F. Strut materials were required to have good stress-rupture properties along with tensile properties, and the sheet metal blade material was required to have hot-corrosion resistance, to be coatable, and to have reasonably good tensile and creep properties. In addition, materials for each of the three components were required to be compatible with selected joining processes.

A number of materials were considered for each component, with the final decision being made on the basis of design requirements and fabrication parameters. The chemical compositions for the selected materials are given in Table X.

4.1.1 Disk Materials

Three materials were considered for the disk application: Inconel 718, Waspaloy, and AF2-1DA. All three are wrought nickel-base alloys that maintain good tensile properties up to at least 1200°F. The relative tensile strengths as a function of temperature for these alloys are shown in Figures 33 and 34. Both Inconel 718 and Waspaloy are commercially available alloys. The alloy AF2-1DA, however, is a more recently developed alloy, on which fabrication and property data is more limited. This alloy was selected for further evaluation, since it offers an apparent property advantage over the other two alloys.

4.1.2 Strut Materials

The material given primary consideration for the strut application was the alloy MAR-M 246. This is a cast nickel-base alloy having stress-rupture properties superior to other commercially available alloys, as indicated in Figure 35.

4.1.3 Sheet Metal Blade Materials

Three materials were considered for the blade application: René 41, AF2-1DA, and AiResist 213. The first two of these alloys are high-strength wrought nickel-base alloys. AiResist 213 is a wrought cobalt-base alloy, which has superior hot-corrosion resistance, although its mechanical properties are inferior to those of René 41 and AF2-1DA. Mechanical properties for these alloys are indicated in Figures 33, 34, and 35.

72

TABLE X. NOMINAL CHEMICAL COMPOSITIONS FOR CANDIDATE ALLOYS

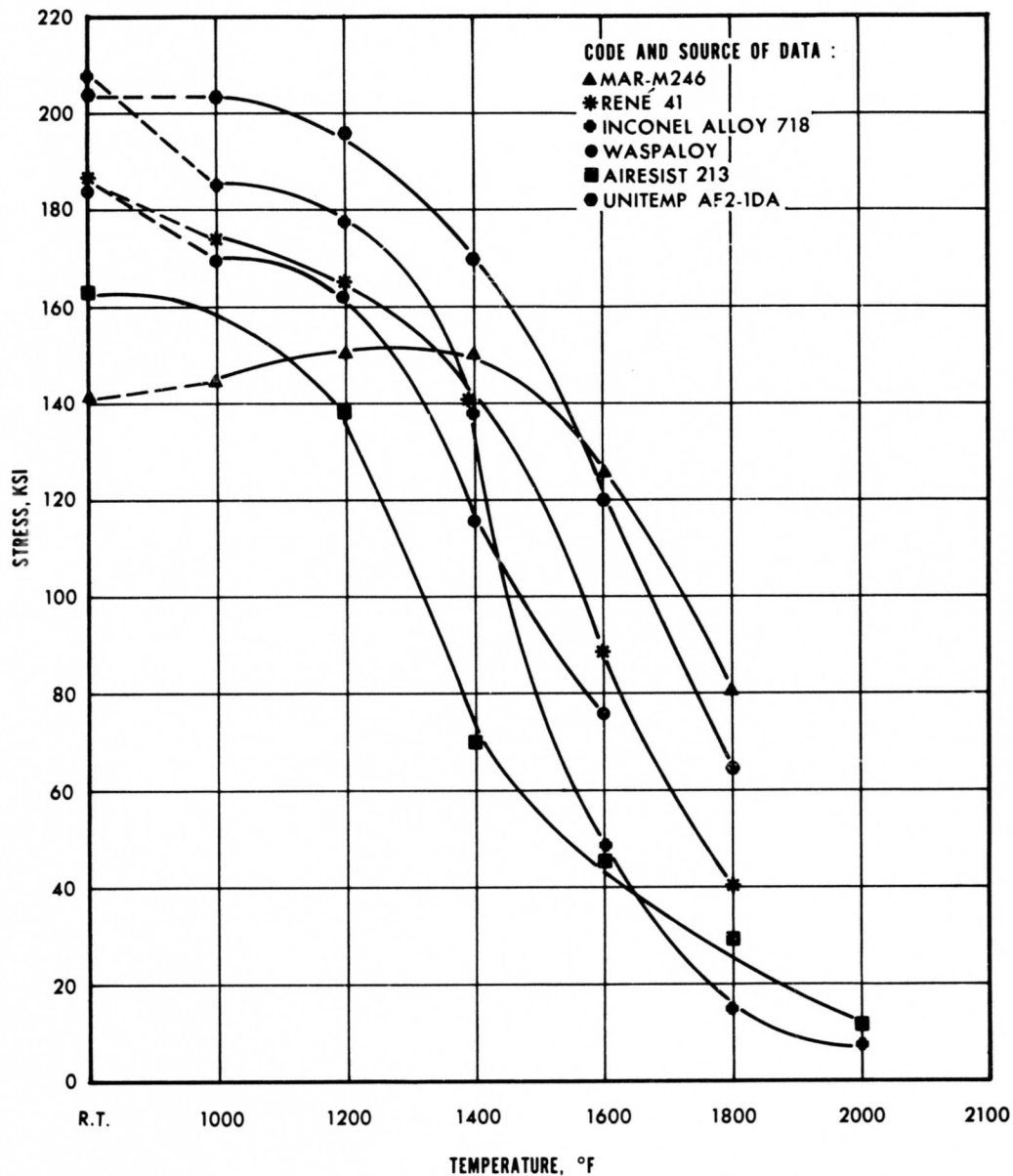| Element	ALLOYS					
	Inconel 718	Waspaloy	AF2-1DA	René 41	MAR-M 246	AiResist 213
Ni	Bal	Bal	Bal	Bal	Bal	0.5 max
Co	-	13.5	10.0	11.0	10.0	Bal
C	0.04	0.8	0.35	0.09	0.15	0.17
Mn	0.20	-	-	-	-	0.10 max
Si	0.30	-	-	-	-	0.20 max
Cr	18.6	19.5	12.0	19.0	9.0	18.0-20.0
Mo	3.1	4.3	3.0	10.0	2.5	-
W	-	-	6.0	-	10.0	4.7
Cb	5.0	-	-	-	-	-
Fe	18.5	-	1.00 max	-	-	0.5 max
Ti	0.9	3.0	3.0	3.1	1.5	-
Al	0.4	1.3	4.60	1.5	5.5	3.5
B	-	0.006	0.015	0.005	0.015	-
Zr	-	0.06	0.10	-	0.05	0.15
Ta	-	-	1.50	-	1.5	6.5
Y	-	-	-	-	-	0.07
Cu	-	-	-	-	-	0.30 max
S	-	-	-	-	-	0.015 max
P	-	-	-	-	-	0.015 max

73

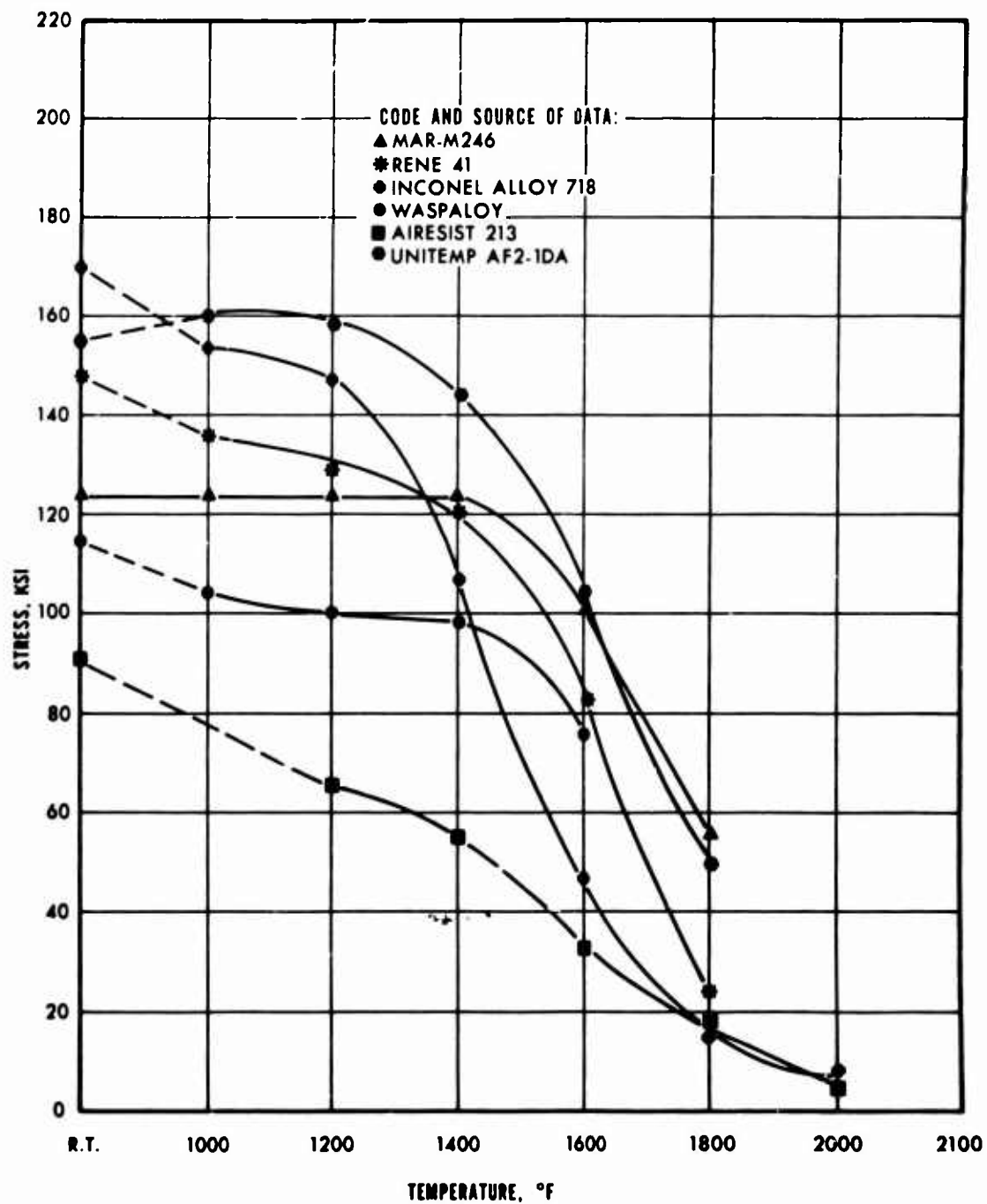Figure 33. Ultimate Tensile Strengths for Candidate Materials.

74

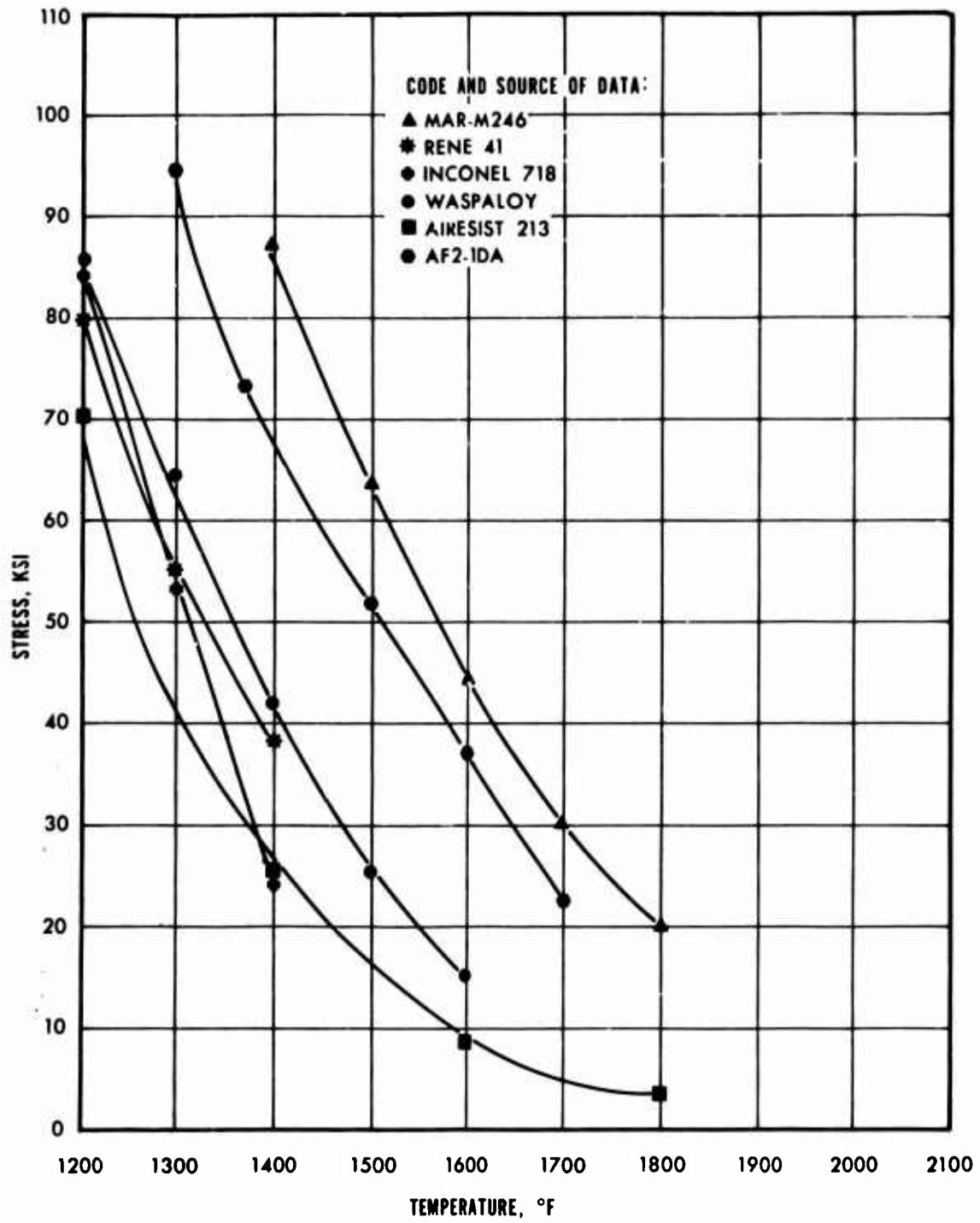Figure 34. Yield Strengths (0.2% Offset) for Candidate Materials.

Figure 35. 1000-Hr Stress-Rupture Strengths
for Candidate Materials.

76

4.2 PRELIMINARY TEST EVALUATIONS

For each selected strut/disk joining technique (diffusion bonding, brazing, and electron-beam welding), a series of preliminary fabrication and joint property tests was performed. In addition, an evaluation of cast bonding for the shell/strut application was conducted. Subsequent subparagraphs detail the results of these preliminary tests.

4.2.1 Diffusion Bonding

Diffusion bonding was considered for both the strut/disk and shell/strut joints. This joining technique offers some potential advantages over other methods, but is somewhat limited as to configurations which can be readily bonded. A design for the strut/disk joint was considered which would allow unidirectional loading to form the bond. The shell/strut joint, however, would likely require isostatic pressure to collapse the sheet metal shell against the strut and maintain sufficient pressure to form the bond. In either case, preliminary information was required on bond strengths which could be expected from the alloys of interest.

4.2.1.1 Experimental Procedure

In order to develop data for the preliminary screening of materials and bonding parameters, an overlap specimen and a pressing die in which to form it were designed as shown in Figure 36. The specimens were prepared from 0.050-inch-thick sheet materials and were polished to approximately a No. 3 rms finish on the surfaces to be bonded. The die was made of graphite and was heated by induction in the vacuum hot press furnace shown in Figure 37. Temperature was measured by a thermocouple placed in the die wall. A vacuum of less than 1 micron was maintained during the heating and pressing operation. The bonding procedure consisted of placing the assembled die (Figure 36) in the pressing furnace, evacuating the chamber to less than 1 micron, heating to the required temperature, and applying the load for the desired time. Bonded specimens were shear-tested by use of the test apparatus shown in Figure 38.

Three bonding parameters with bonding temperature maintained at 1800°F were evaluated: interface material, bonding pressure, and bonding time. Previously reported data had shown that bond strength could be improved by the use of a dissimilar interface material to serve as a "diffusion activator." Specimens were prepared with no interface material, with a 0.0005-inch nickel plate, and with a 0.001-inch-thick foil of a nickel plus 3-percent beryllium alloy. Bonding pressures were varied between 11,500 psi and 40,000 psi,

77

and bonding times were varied between 15 and 45 minutes. Two shear stresses were reported for each specimen. The "apparent shear stress" is that stress calculated on the basis of the total specimen overlap area. However, as a result of imperfect matching of surfaces, this total area was not completely bonded, in most cases. The "estimated actual shear stress" is therefore reported and is based on the estimated area of actual bond as determined by examination of the sheared surfaces. Material combinations evaluated initially are given in Table XI.

4.2.1.2 Test Results and Conclusions

Results of shear testing of the overlap specimens are given in Table XII. Material combinations of primary interest for the strut/disk joint included Waspaloy, Inconel 718, and AF2-1DA as disk materials joined to MAR-M 246 as a strut material. A summary of results of these combinations is given in Table XIII.

Difficulty in obtaining AF2-1DA in the required geometries precluded further material-combination evaluations utilizing this material type. Bonding data indicated the joint strengths of the Inconel 718/MAR-M 246 combination to be better than those between Waspaloy and MAR-M 246. The use of a thin nickel strike (0.0005-inch-thick) as an interface material gave consistently good strengths and a high percentage of bonded area, which indicates a tolerance for surface irregularities. This is an important consideration in the bonding of more complex geometries.

For these reasons, the final selection for diffusion-bonding evaluation was Inconel 718 joined to MAR-M 246 with a 0.0005-inch-thick nickel interface material. With use of these materials, the process was scaled up to specimens of a size similar to that required for the final test specimens. Figure 39 shows the larger specimen, and Figure 40 shows the die used to form it. These specimens were then further scaled up to the geometry shown in Figure 41, which exactly simulates the final specimen geometry. A typical bond produced in the final geometry is shown in Figure 42.

In order to develop full mechanical properties in the Inconel 718 disk material, the proper heat treatment was required. The fabrication procedure therefore consisted of bonding the specimens with the MAR-M 246 in the as-cast condition and the Inconel 718 in the solutioned condition. After bonding, the specimen was then given the proper heat treatment for the Inconel 718 material.

SHEET METAL

GRAPHITE DIE

GRAPHITE PLUNGERS

0.05

0.10 OVERLAP

0.20

0.50

FINAL SPECIMEN

(DIMENSIONS, IN.)
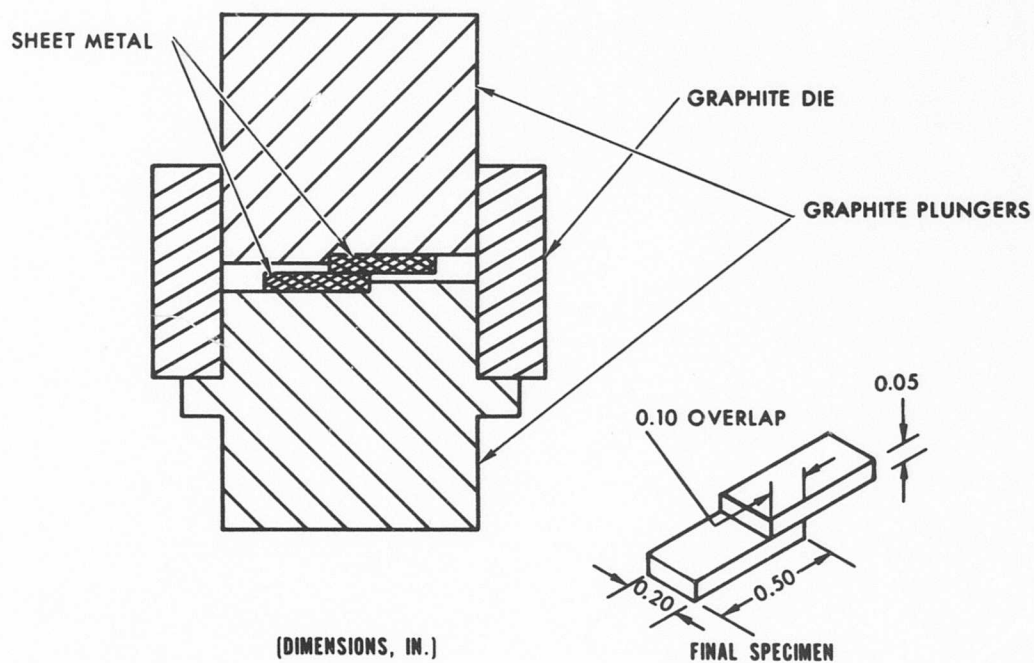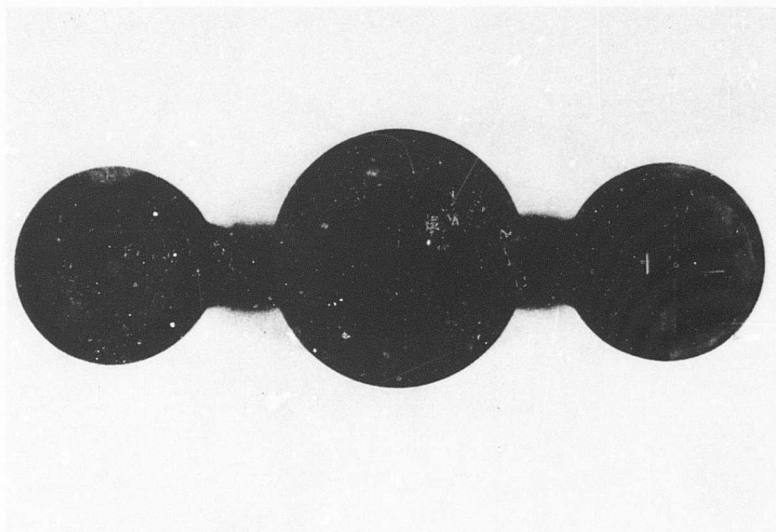
Figure 36. Pressing Die and Plunger Arrangement Used
for Diffusion Bonding of Sheet Specimens.

79

Figure 37.   Vacuum Hot Press Furnace Used for Fabrication
             of Diffusion-Bonded Specimens.
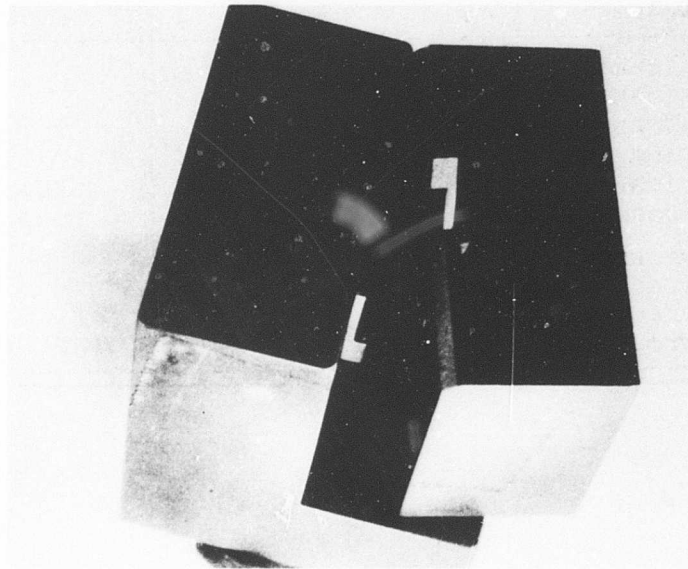
THIS BLOCK IS HELD
AGAINST THE L-SHAPED
BLOCK WITH 4 BOLTS,
FINGER TIGHT
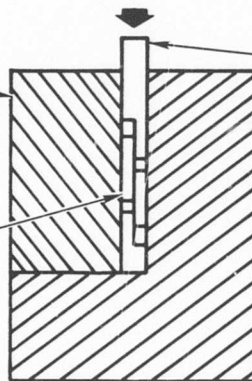
HARDENED STEEL
PUSHER PLATES (2)

SPECIMEN

0.10 OVERLAP   0.05

0.20   0.50
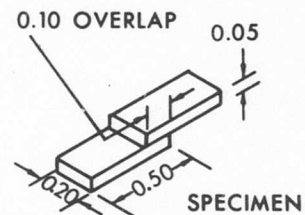
SPECIMEN

(DIMENSIONS, IN.)

Figure 38. Test Fixture Used to Shear Test
Diffusion-Bonded and Cast-Bonded
Overlap Specimens.

81

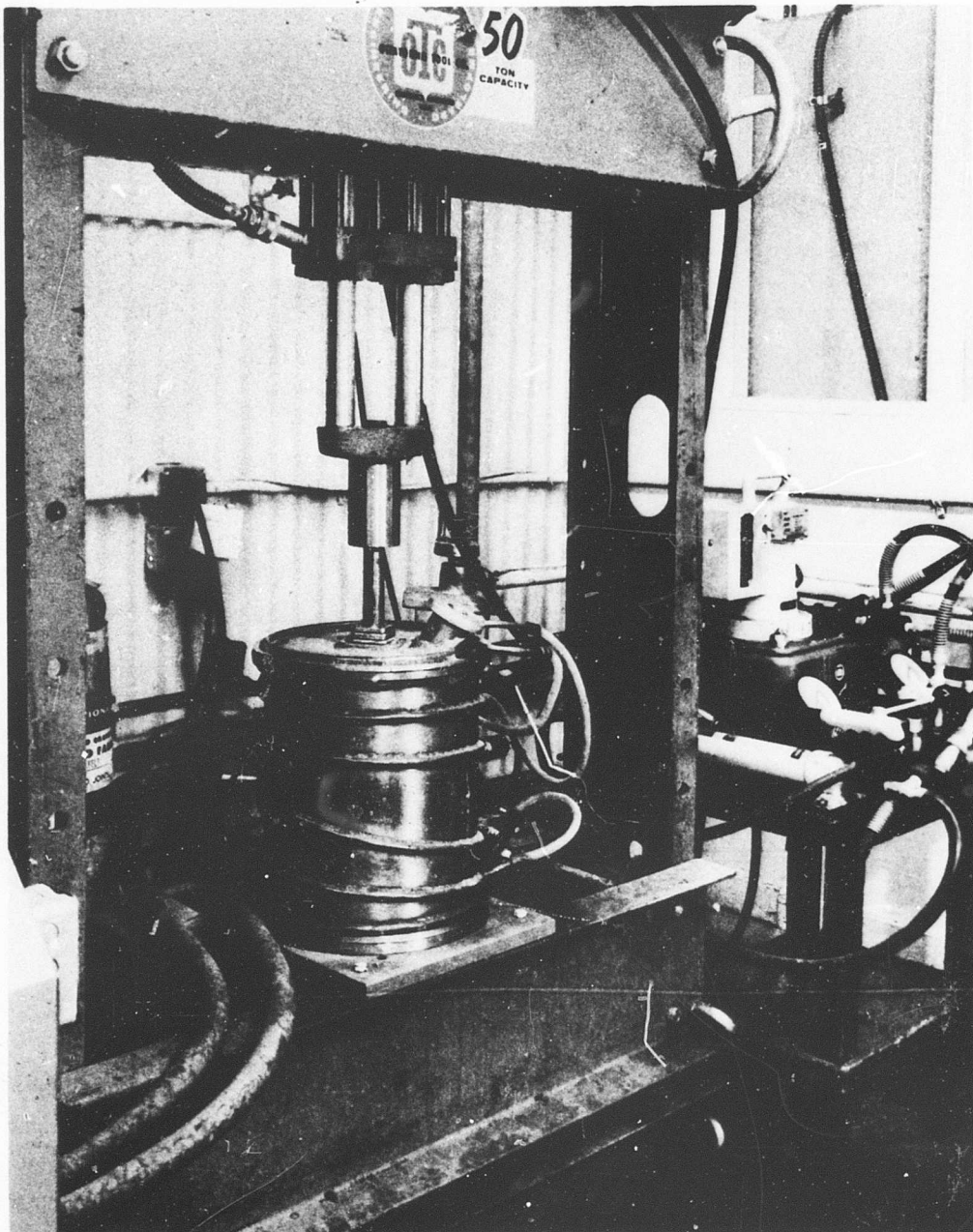| TABLE XI. MATERIAL COMBINATIONS EVALUATED INITIALLY FOR DIFFUSION-BONDED JOINTS		
Candidate Strut Material	Sheet Material (Strut/Shell Bond)	Disk Material (Strut/Disk Bond)
MAR-M 246 (cast)	AiResist 213	
MAR-M 246 (cast)	René 41	
MAR-M 246 (cast)	AF2-1DA	
MAR-M 246 (cast)		AF2-1DA
MAR-M 246 (cast)		Waspaloy
MAR-M 246 (cast)		Inconel 718
AF2-1DA (wrought)	AiResist 213	
AF2-1DA (wrought)	René 41	
AF2-1DA (wrought)	AF2-1DA	
AF2-1DA (wrought)		AF2-1DA

TABLE XII. LAP/SHEAR TESTS OF DIFFUSION-BONDED SPECIMENS					
Speci-men No.	Material Combination	Interface Material	Bonding Conditions Temp/Time/Pressure	Apparent Shear Stress (psi)	Estimated Actual Shear Stress (psi)
D-1	MAR-M 246/AiR 213	None	1800°F/15 min /11,600 psi	23,800	39,100
D-2				22,300	38,400
D-3				25,400	42,800
D-14	MAR-M 246/AiR 213	None	1800°F/15 min /29,500 psi	53,000	90,000
D-15				26,000	46,800
D-16				51,500	81,900
D-7	MAR-M 246/AiR 213	Ni	1800°F/15 min /11,600 psi	-	-
D-8				48,900	76,700
D-9				40,600	87,800
8-1A	MAR-M 246/AiR 213	Ni + 3% Be (0.001 in.)	1800°F/45 min /11,600 psi	23,300	54,200
8-2A				54,200	39,600
8-3A				19,500	41,000
8-1B	MAR-M 246/AiR 213	Ni + 3% Be (0.001 in.)	1800°F/15 min /29,500 psi	36,900	48,600
8-2B				47,200	50,100
8-3B				47,200	49,200
D-4-1	MAR-M 246/Rene' 41	None	1800°F/15 min /11,600 psi	31,100	68,500
D-4-2				30,600	54,600
D-4-3				16,700	43,500
D-4-10	MAR-M 246/Rene' 41	None	1800°F/15 min /29,500 psi	32,700	63,400
D-4-11				5700	11,100
D-4-12				10,000	16,500
D-4-7	MAR-M 246/Rene' 41	Ni	1800°F/15 min /11,600 psi	16,900	45,400
D-4-8				29,700	54,500
D-4-9				12,500	23,000
4-1	MAR-M 246/Rene' 41	Ni + 3% Be (0.001 in.)	1800°F/45 min /11,600 psi	17,800	22,300
4-2				30,600	31,300
4-3				21,700	24,000
13-1	AF2-1DA/AiR 213	None	1800°F/15 min /29,500 psi	34,200	42,700
13-2				21,300	28,400
13-3				36,700	43,200
14-1	AF2-1DA/AiR 213	None	1800°F/15 min /29,500 psi	46,800	52,100
14-2				53,700	57,200
14-3				62,800	64,100
15-1	AF2-1DA/AiR 213	Ni	1800°F/15 min /11,600 psi	33,100	27,100
15-2				32,100	36,900
15-3				19,200	27,400
16-1	AF2-1DA/AiR 213	Ni + 3% Be (0.001 in.)	1800°F/45 min /11,600 psi	23,500	26,200
16-2				20,200	31,000
16-3				37,100	39,000
9-1	AF2-1DA/Rene' 41	None	1800°F/15 min /11,600 psi	47,030	42,500
9-2				8400	62,600
9-3				37,800	51,500
10-1	AF2-1DA/Rene' 41	None	1800°F/15 min /29,500 psi	67,200	83,800
10-2				90,000	94,800
10-3				66,000	73,700
11-1	AF2-1DA/Rene' 41	Ni	1800°F/15 min /11,600 psi	34,600	40,800
11-2				47,700	53,900
11-3				18,100	27,700
12-1	AF2-1DA/Rene' 41	Ni + 3% Be (0.001 in.)	1800°F/45 min /11,600 psi	20,000	23,600
12-2				35,900	36,100
12-3				41,500	42,300

Speci-men No.	Material Combination	Interface Material	Bonding Conditions Temp/Time/Pressure	Apparent Shear Stress (psi)	Estimated Actual Shear Stress (psi)
17-1 17-2 17-3	AF2-1DA/AF2-1DA	None	1800°F/15 min /11,600 psi	36,800 25,100 30,100	38,900 28,900 33,500
18-1 18-2 18-3	AF2-1DA/AF2-1DA	None	1800°F/15 min /29,500 psi	62,600 65,000 72,200	64,500 66,400 72,800
19-1 19-2 19-3	AF2-1DA/AF2-1DA	Ni	1800°F/15 min /11,600 psi	25,400 27,200 25,600	30,200 30,200 30,100
20-1 20-2 20-3	AF2-1DA/AF2-1DA	Ni + 3% Be (0.001 in.)	1800°F/15 min /11,600 psi	42,000 31,100 46,400	44,400 34,600 47,700
21-1 21-2 21-3	AiR 213/Rene 41	Ni + 3% Be (0.001 in.)	1800°F/45 min /29,500 psi	58,300 58,000 53,000	61,400 61,100 57,200
1 2 3	MAR-M 246/AF2-1DA	None	1800°F/15 min /40,600 psi	67,200 74,500 63,200	67,200 74,500 63,200
10 11 12	MAR-M 246/AF2-1DA	None	1800°F/15 min /29,500 psi	41,600 51,000 36,000	55,500 59,400 59,400
19 20 21	MAR-M 246/AF2-1DA	Ni (0.0005-in.)	1800°F/15 min /29,500 psi	96,800 95,200 91,000	96,800 95,200 91,000
28 29 30	MAR-M 246/AF2-1DA	Ni + 3% Be (0.001-in.)	1800°F/45 min /29,500 psi	88,200 156,000 148,500	104,000 156,000 148,500
4 5 6	MAR-M 246/Waspaloy	None	1800°F/15 min /40,600 psi	74,200 68,200 75,700	82,500 80,000 84,000
13 14 15	MAR-M 246/Waspaloy	None	1800°F/15 min /29,500 psi	72,200 55,000 30,700	72,200 69,000 51,200
22 23 24	MAR-M 246/Waspaloy	Ni (0.0005 in.)	1800°F/15 min /29,500 psi	70,800 67,900 70,200	70,800 67,900 70,200
31 32 33	MAR-M 246/Waspaloy	Ni + 3% Be (0.001-in.)	1800°F/45 min /29,500 psi	74,000 81,000 68,000	74,000 81,000 68,000
7 8 9	MAR-M 246/ Inconel 718	None	1800°F/15 min /40,600 psi	95,600 59,500 95,800	106,200 91,500 100,500
16 17 18	MAR-M 246/ Inconel 718	None	1800°F/15 min /29,500 psi	67,300 103,200 99,000	75,000 103,200 99,000
25 26 27	MAR-M 246/ Inconel 718	Ni (0.0005-in.)	1800°F/15 min /29,500 psi	94,900 93,700 100,000	94,900 93,700 100,000
34 35 36	MAR-M 246/ Inconel 718	Ni + 3% Be (0.001-in.)	1800°F/45 min /29,500 psi	83,800 88,500 81,500	83,800 88,500 81,500

TABLE XII – Continued

84

TABLE XIII. SUMMARY OF SHEAR-TEST RESULTS ON DIFFUSION-BONDED SPECIMENS

| Material Combination	Interface Material	Bonding Conditions Time/Temp/Pressure	Apparent Shear Stress (psi)	Estimated Actual Shear Stress (psi)
AF2-1DA/MAR-M 246	None	15 min/1800°F/40,600 psi	68,300	68,300
AF2-1DA/MAR-M 246	None	15 min/1800°F/29,500 psi	42,866	58,100
AF2-1DA/MAR-M 246	Ni	15 min/1800°F/29,500 psi	94,333	94,333
AF2-1DA/MAR-M 246	Ni + Be sheet	45 min/1800°F/29,500 psi	130,900	136,166
Waspaloy/MAR-M 246	None	15 min/1800°F/40,600 psi	72,700	82,166
Waspaloy/MAR-M 246	None	15 min/1800°C/29,500 psi	52,633	64,133
Waspaloy/MAR-M 246	Ni	15 min/1800°F/29,500 psi	69,633	69,633
Waspaloy/MAR-M 246	Ni + Be sheet	45 min/1800°F/29,500 psi	74,333	74,333
Inconel 718/ MAR-M 246	None	15 min/1800°F/40,600 psi	83,633	99,400
Inconel 718/ MAR-M 246	None	15 min/1800°F/29,500 psi	89,833	92,400
Inconel 718/ MAR-M 246	Ni	15 min/1800°F/29,500 psi	96,200	96,200
Inconel 718/ MAR-M 246	Ni + Be sheet	45 min/1800°F/29,500 psi	84,600	84,600
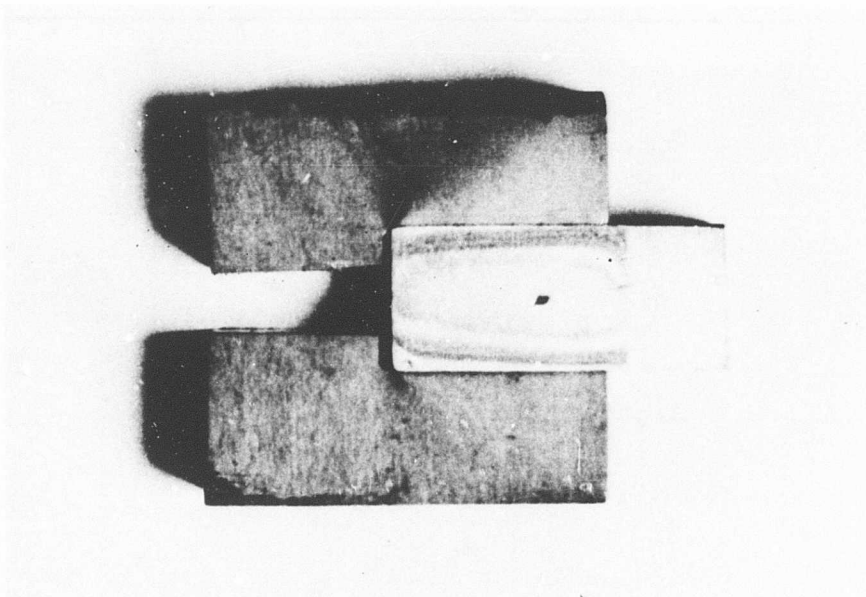
Figure 39. Diffusion-Bonding Specimen
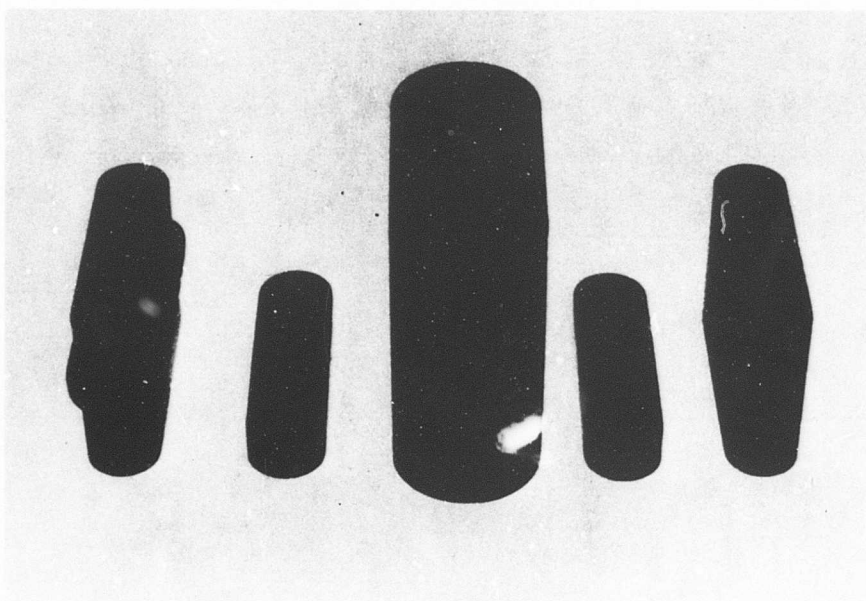(Final Test Size).

Figure 40. Die Used for Diffusion
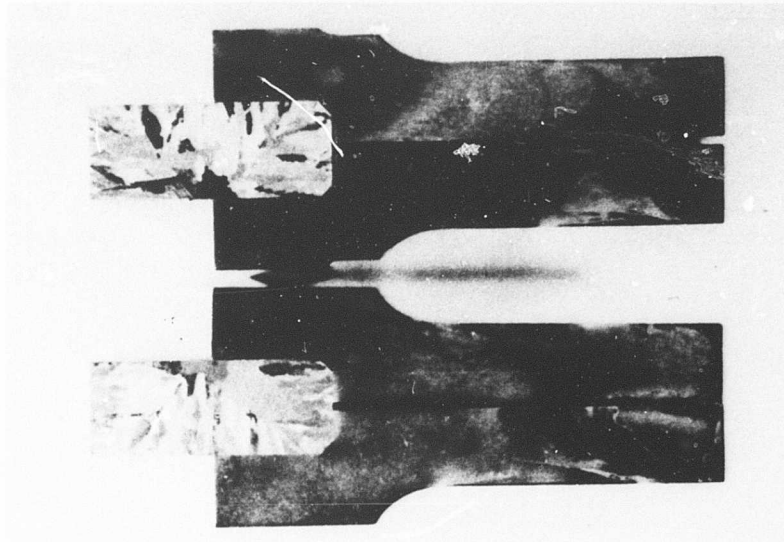Bonding of Figure 39
Specimen.

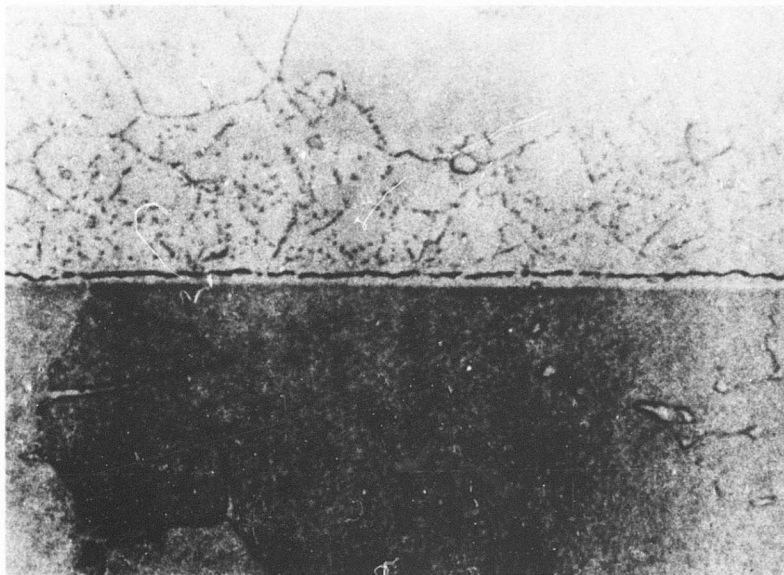Figure 41. Diffusion-Bonded Specimens Simulating
the Final Test Design.

Figure 42. Typical Diffusion-Bonded Joint
Produced With Parameters Selected
for Final Test Specimens.

87

4.2.2 Brazing

Brazing was considered as a joining technique for both the strut/disk and the strut/shell joints. Primary consideration, however, was given to the strut/disk joint, since this region of the rotor can be designed such that temperatures and stresses are sufficiently low to permit reasonably high values for the stress-rupture life of the brazing alloy. Materials that were evaluated included AF2-1DA, Waspaloy, and Inconel 718 as disk materials, MAR-M 246 as strut material, and René 41 and AiResist 213 as shell materials.

4.2.2.1 Experimental Procedure

Three candidate brazing alloys were selected for evaluation: Nicrobraz 30, Nicrobraz 150, and Palniro 49TX. Compositions for each of these alloys are given in Table XIV. Selection of these alloys were based upon reported high-temperature stress-rupture properties.

Test specimens as shown in Figure 43 were prepared for preliminary testing. Specimens were machined from 0.050-inch thick sheet material, and the overlap surfaces were nickel-plated to a thickness of 0.0002 to 0.0005 inch. The specimens were positioned and tack-welded in the fixture shown in Figure 44. In each case, the braze gap clearance was controlled by shimming (to 0.002 inch) prior to tack welding. Both of the Nicrobraz alloys were placed in powder form in an amount to fill the gap adequately during the brazing operation. The Palniro 49TX alloy was preplaced in foil form (0.002-inch-thick) prior to tack welding.

Brazing was performed in a vacuum furnace at a vacuum of 0.5 micron and with a cycle of 2150° ±10°F for 20 minutes. Final machining of the specimens, as shown in Figure 45, removed the tack weld. All testing was by stress-rupture, since this is, in general, the limiting strength property of a brazed joint.

### 4.2.2.2 Test Results and Conclusions

Stress-rupture test results are listed in Table XV. Data for the strut/disk material combinations of Waspaloy to MAR-M 246 and Inconel 718 to MAR-M 246 indicated that the Nicrobraz 150 brazing alloy potentially offers the greatest stress-rupture strength. However, this alloy was eliminated from further consideration because of excessive erosion (base-metal attack) as indicated by Figure 46.

In most cases, the Nicrobraz 150 specimens failed through the
bare metal at the brazing fillet area rather than through the
brazing material. An example of such a failure is shown in
Figure 46. Most of the specimens on which testing was ter-
minated after approximately 100 hours failed at the fillet
area upon removal from the testing fixtures. This indicated
the extent of the embrittling effect of the braze. Examples
of typical failed joints for specimens brazed with Nicrobraz
30 and Palniro 49TX are shown in Figures 47 and 48, respec-
tively. In both of these cases, the small amount of erosion
and the failure through the brazing material are evident.

The Palniro 49TX alloy behaved quite well during brazing
and produced a sound joint. However, the stress-rupture
strength of this alloy was somewhat less than for Nicrobraz 30
at the higher temperatures. As a result, Nicrobraz 30 alloy
was selected for use in the final test specimens.

Figure 49 shows stress-rupture data for Nicrobraz 30 joints
with the two material combinations of Waspaloy/MAR-M 246 and
Inconel 718/ MAR-M 246. The combination of Waspaloy with
MAR-M 246 gave the better stress-rupture properties. Specimens
from which these data were obtained were given a post-braze
heat treatment to correspond to the required treatment for
either Inconel 718 or Waspaloy, as applicable. Examination of
failed specimens indicated that the Inconel 718/MAR-M 246
specimens had a tendency to shear at the interface between the
braze and the Inconel 718 rather than through the braze. For
these reasons, the Waspaloy/MAR-M 246 combination was selected
for further testing.

TABLE XIV. NOMINAL COMPOSITIONS OF THE BRAZING ALLOYS SELECTED FOR EVALUATION								
NOMINAL COMPOSITION								
Material	Cr	Si	C	Ni	B	Ta	Pd	Au
Nicrobraz 30	19.0	10.0	0.10	Bal	–	–	–	–
Nicrobraz 150	15.0	–	0.10	Bal	3.5	–	–	–
Palniro 49TX	9.0	–		29.0		1.0	27.5	33.5

3T (0.075")

T

0.050"

—1 AS BRAZED

4"

1"
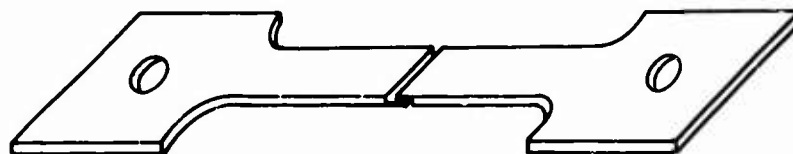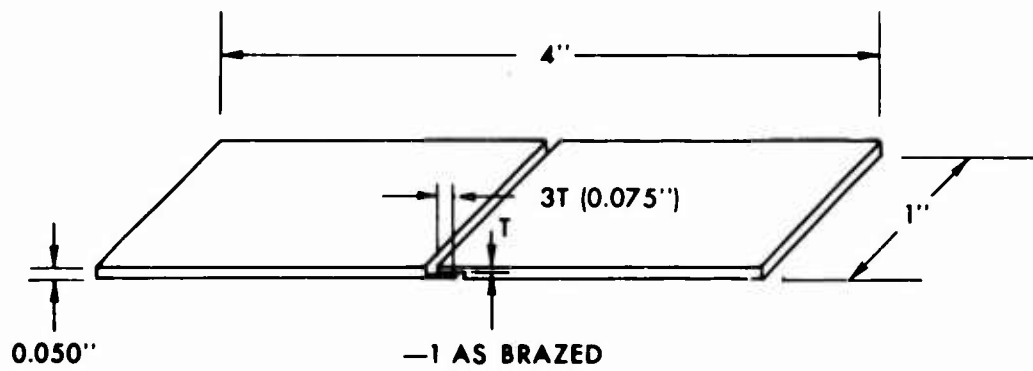
—2 READY FOR TEST

BRAZE TEST SPECIMEN
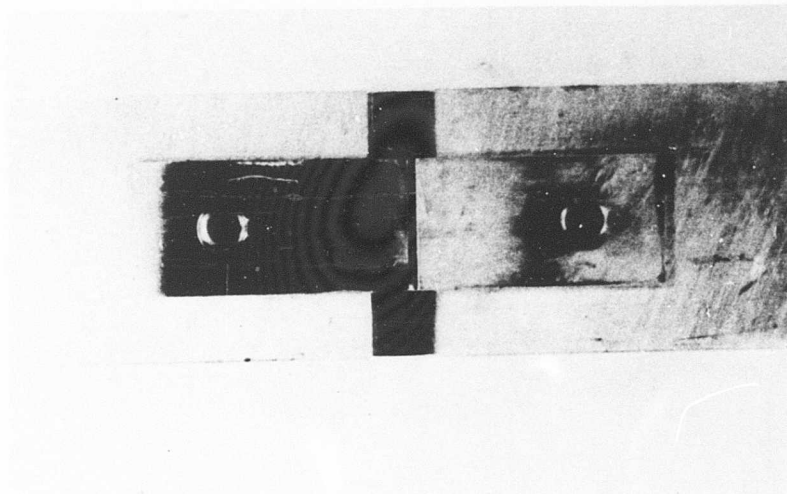
Figure 43. Brazing Test Specimen.

90

Figure 44.   Fixture Used During Tack Welding of
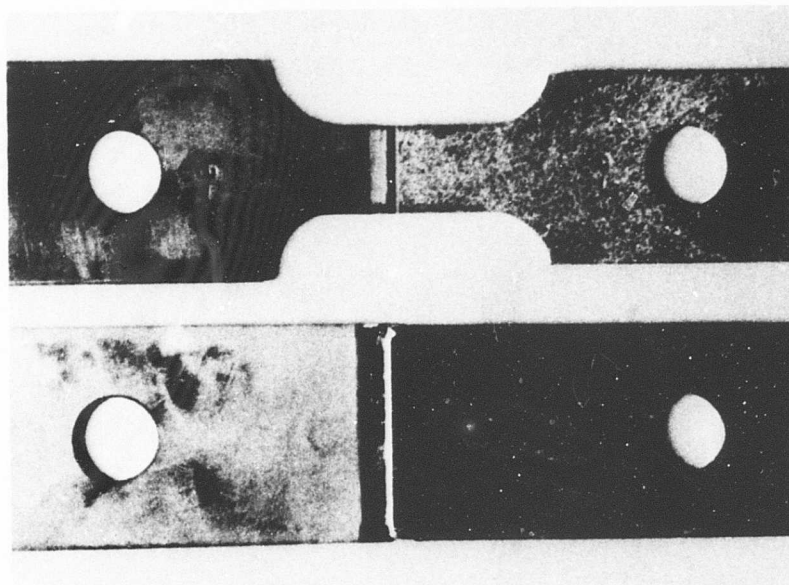the Brazing Specimens.

Figure 45.   Brazing Specimens Before (Top) and
After (Bottom) Final Machining.

91

TABLE XV. STRESS-RUPTURE DATA
ON BRAZING SPECIMENS

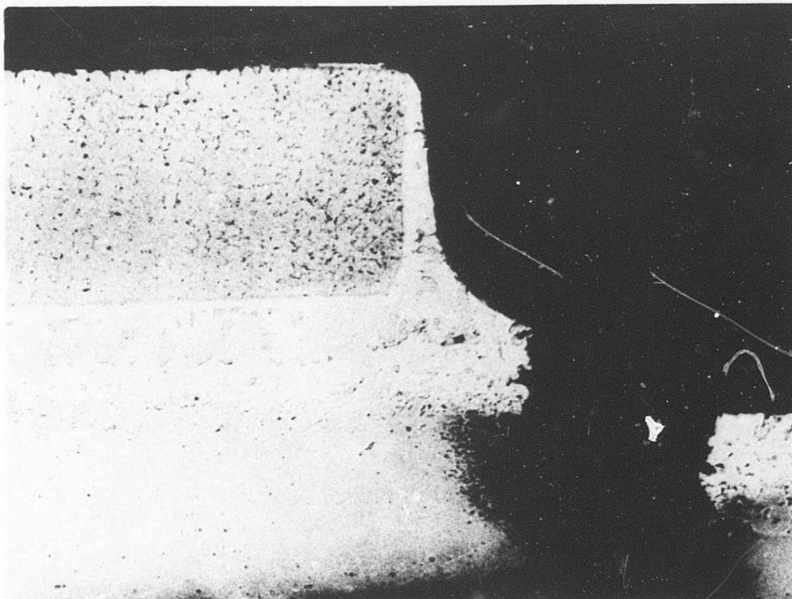| Specimen No.	Material Combination	Braze Alloy	Temp (°F)	Stress (psi)	Time (Hours)	Fracture Location	Comments	Specimen Heat Treatment
1-0	AF2-1DA/	Nicrobraz	1200	10,000	100.0	No fracture	Test discontinued	
1-1	AF2-1DA	30	1200	20,000	0.2	Through braze		
1-2			1200	15,000	1.2	Same as above		None
1-3			1400	8000	1.6	Same as above		
1-4			1400	5000	40.7	Same as above		
1-5			1400	6500	13.1	Same as above		
2-0	MAR-M 246/	Nicrobraz	1200	30,000	–	Through MAR-M 246	Broke on loading	
2-1	AiR 213	30	1200	15,000	–	Through braze	Broke on loading	
2-2			1200	7500	100.0	No fracture	Test discontinued	None
2-3			1400	20,000	–	Through braze	Broke on loading	
2-4			1400	10,000	0.5	Through braze		
2-5			1400	7500	–	Through braze	Broke on loading	
3-0	AF2-1DA/	Nicrobraz	1200	10,000	14.0	Through AF2-1DA		
3-1	AiR 213	30	1200	8000	100.0	No fracture	Test discontinued	
3-2			1200	9000	100.0	No fracture	Test discontinued	None
3-3			1400	9000	0.7	Through braze		
3-4			1400	5000	4.6	Through braze		
3-5			1400	2500	100.0	No fracture	Test discontinued	
4-1	MAR-M 246/	Palniro	1200	11,000	19.0	Through braze		
4-2	INCO 718	49TX	1200	10,000	23.1	Through braze		
4-3			1200	9000	36.5	Through braze		Inconel 718 age
4-4			1400	9500	0.3	Through braze		
4-5			1400	8000	0.7	Through braze		
5-1	MAR-M 246/	Nicrobraz	1200	10,000	19.1	Through braze		
5-2	INCO 718	30	1200	9000	20.8	Through braze		
5-3			1200	6000	101.0	No fracture	Test discontinued	
5-4			1400	10,000	2.3	Through braze		
5-5			1400	8000	3.9	Through braze		Inconel 718 age
6-1	MAR-M 246/	Nicrobraz	1200	8000	100.3	Braze fillet	Broke on removal	
6-2	INCO 718	150	1200	10,000	114.0	Braze fillet	Broke on removal	
6-3			1200	20,000	122.1	Braze fillet		Inconel 718 age
6-4			1400	9000	114.0	No fracture	Test discontinued	
6-5			1400	12,000	13.3	Braze fillet		
7-1	AF2-1DA/	Palniro	1200	12,000	5.2	Through braze		
7-2	René 41	49TX	1200	10,000	14.3	Through braze		
7-3			1200	8000	33.3	Through braze		None
7-4			1400	10,000	–	Overtemp	Broke on loading	
7-5			1400	9000	1.4	Through braze		
7-6			1400	6000	6.4	Through braze		
8-1	René 41/	Nicrobraz	1200	8000	100.0	No fracture	Test discontinued	
8-2	AF2-1DA	30	1200	20,000	–	Through braze	Broke on loading	None
8-3			1200	12,000	84.7	Through braze		
8-4			1400	8000	–	Through braze	Broke on loading	
8-5			1400	15,000	–	Through braze	Broke on loading	
8-6					–	Through braze	Broke in machining	
9-1	René 41/	Nicrobraz	1200	12,000	114.0	No fracture	Test discontinued	
9-2	MAR-M 246	30	1200	15,000	109.0	No fracture	Test discontinued	
9-3			1200	10,000	7.4	Through braze		
9-4			1400	8000	30.6	Through braze		
9-5					–	Through braze	Broke in machining	
9-6					–	Through braze	Broke in machining	
10-1	René 41/	Nicrobraz	1200	13,000	108.8	Through braze		
10-2	MAR-M 246	150	1200	16,000	42.0	Braze fillet		None
10-3			1400	11,000	15.8	Through braze		
10-4			–	–	–	Through braze	Broke in machining	
10-5			–	–	–	Through braze	Broke in machining	
10-6			–	–	–	Through braze	Broke in machining	
11-1	Waspaloy/	Nicrobraz	1200	15,000	111.0	No fracture	Test discontinued	
11-2	MAR-M 246	30	1200	20,000	0.8	Braze fillet		
11-3			1200	17,500	0.2	Braze fillet		Waspaloy age
11-4			1400	7000	92.4	Through braze		
11-5			1400	12,000	2.1	Through braze		

Figure 46.   Typical Failed Joint Between
Inconel 718 and MAR-M 246 with
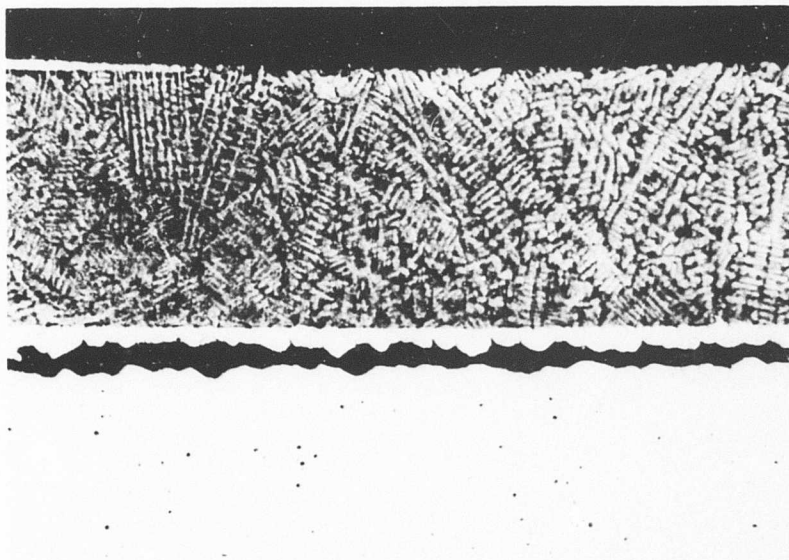Nicrobraz 150 Brazing Alloy (X50).

Figure 47.   Typical Failed Joint Between
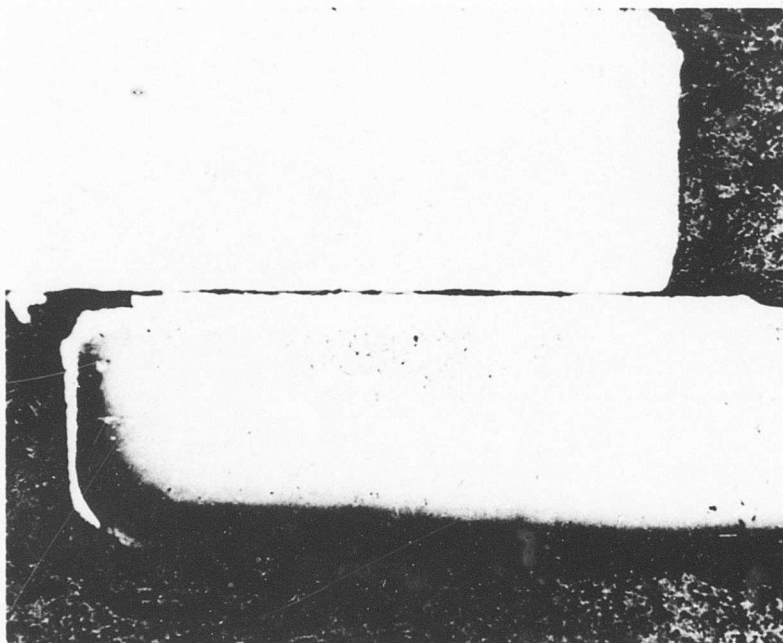Inconel 718 and MAR-M 246 With
Nicrobraz 30 Brazing Alloy (X50).

93

Figure 48. Typical Failed Joint Between
Inconel 718 and MAR-M 246 With
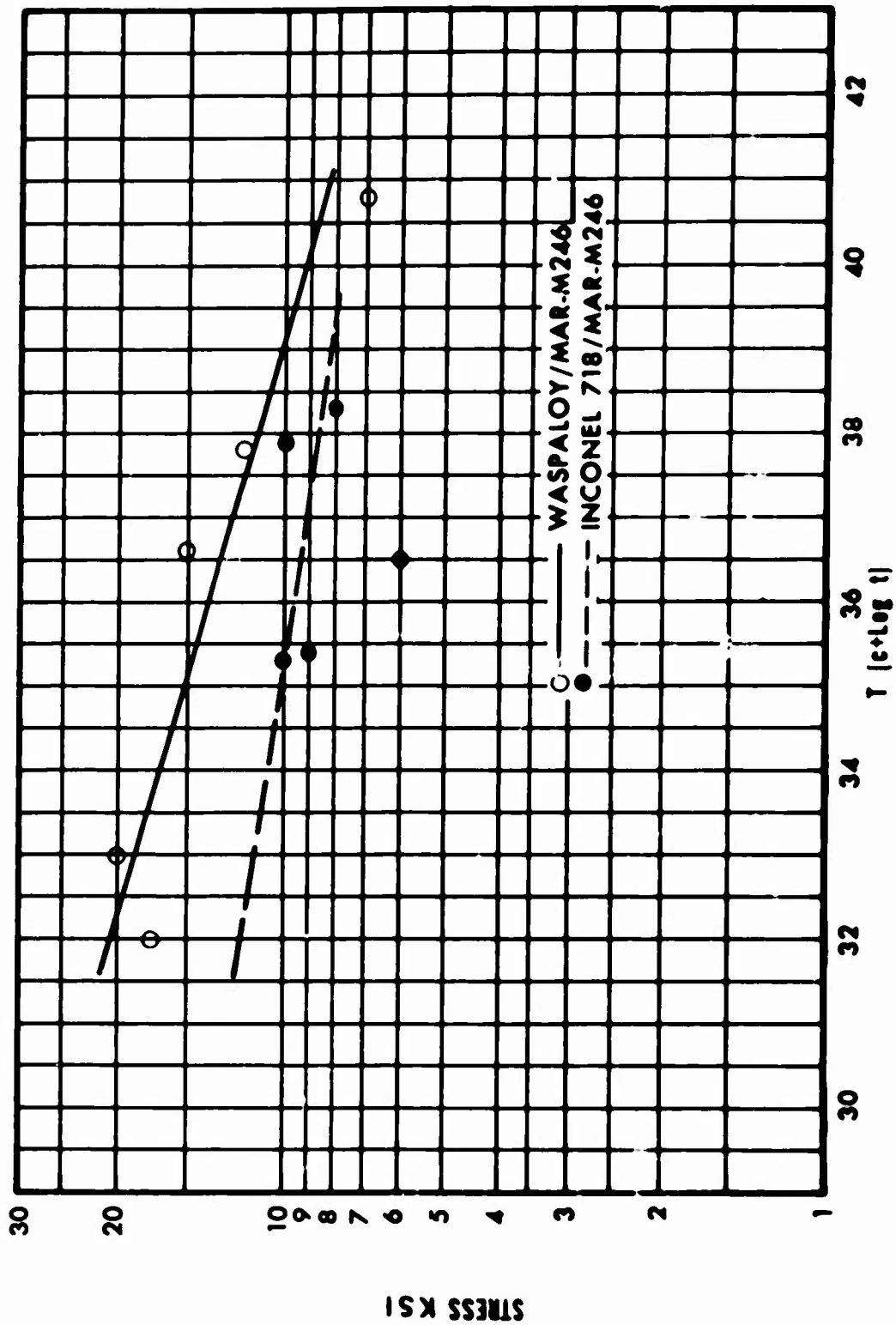Palniro 49TX Brazing Alloy (X50).

Figure 49.   Stress-Rupture Data for
Nicrobraz 30 Brazed Joints.

4.2.3 Electron-Beam Welding

Electron-beam welding was considered for the strut/disk joint.
Preliminary evaluations and testing were performed to estab-
lish materials and welding parameters required to optimize the
weld joint. Materials given initial consideration included
MAR-M 246 and AF2-lDA as strut materials and Waspaloy, Inconel
718, and AF2-lDA as disk materials.

4.2.3.1 Experimental Procedure

Preliminary weld evaluations were performed on the specimens
shown in Figures 50 and 51. These specimens were prepared by
butt welding two pieces of 0.050-inch-thick dissimilar sheet
material together and subsequently machining to form a tensile
specimen. The MAR-M 246 specimens were selected from cast-to-
size flats and were welded in the as-cast condition and also
in the 2000°F/2-hour heat-treated condition. For the remainder
of the alloys, specimens were cut from sheet material and were
welded in the solutioned condition. Post-weld heat treatments
were given the specimens to simulate the required heat treat-
ments for the age-hardenable materials.

Evaluation of the strip specimens was by metallographic ex-
amination and by tensile testing. Results indicate the mate-
rial combinations that offered the greatest promise for further
testing. These combinations were further evaluated by welding
together blocks which simulated the thickness required for
the final strut/disk weld joint. Welding parameters were
varied and specimens examined to determine the parameters to
be used for the final test specimens.

4.2.3.2 Test Results and Conclusions

Examination of the preliminary weld specimens (Figure 52)
indicated a tendency toward weld cracking, which is confirmed
in Figure 53, in combinations including the alloy AF2-lDA.
Variations made in welding parameters in an attempt to elimi-
nate this cracking were successful only in reducing the extent
of cracking. Because of this problem, AF2-lDA was eliminated
from further consideration. This left two possible material
combinations: MAR-M 246/Waspaloy and MAR-M 246/Inconel 718.

Results of tensile tests are given in Table XVI. A summary of
results is given in Table XVII and indicates that tensile
failures occurred in the cast material (MAR-M 246) in all cases
after the specimens were given a post-weld heat treatment to
develop full properties in the heat-treatable material. Limit-
ing properties, therefore, were those of the MAR-M 246 mate-
rial.

The welding procedure was then scaled up to specimen sizes
simulating the sizes required for the final test specimens.
Welding was performed on blocks of the two material combina-
tions MAR-M 246/Inconel 718 and MAR-M 246/Waspaloy. A total
weld penetration distance of 0.790 inch was required. Two
methods of achieving this penetration were investigated. The
first consisted of welding from each side of the specimen with
weld settings such that the two weld spikes would merge. Prob-
lems were encountered with use of this technique in that mis-
alignment of weld spikes occurred, as shown in Figure 54. Also,
in some cases, voids were formed in weld overlap areas, as
shown in Figure 55. The weld spike appearing in the figures
on one side of the joint was included prior to the joining
weld to simulate the initial welding required to join the disk
halves together. Because of the problems with the double-
spike joint, a single-pass joint was developed as shown in
Figure 56. Some cracking was encountered with this technique,
as shown in Figure 57. By adjustment of welding parameters,
this cracking was minimized and appeared to be less severe
when joining Waspaloy to MAR-M 246 than when joining Inconel
718 to MAR-M 246. In addition, a preweld stabilization treat-
ment of the MAR-M 246 consisting of 2000°F for 2 hours was
found to reduce the cracking tendencies.

As a result of the development efforts outlined above, the
material combination selected for final testing was MAR-M 246
to Waspaloy. The electron-beam-welding parameters selected
for fabrication of the final test specimens are detailed in
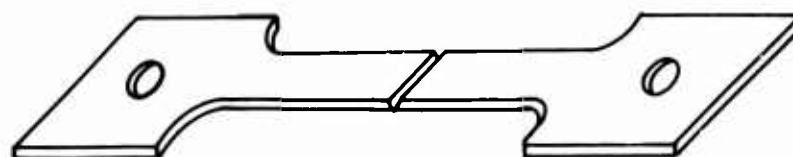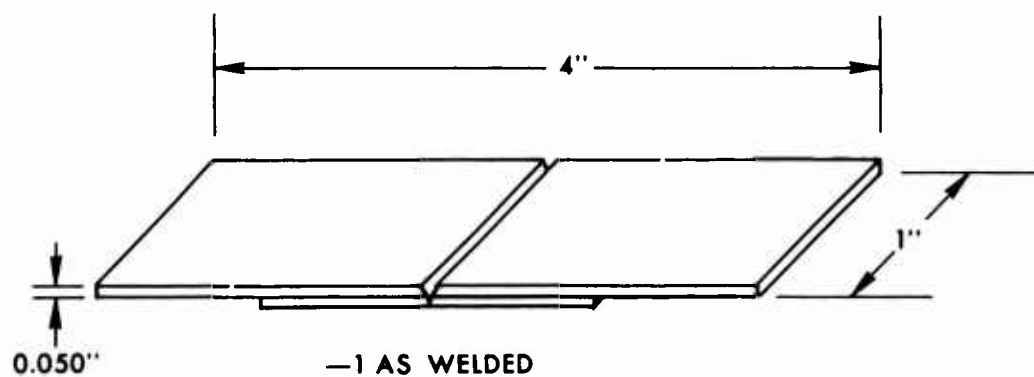Section 5.2.3.

—1 AS WELDED

—2 READY FOR TEST

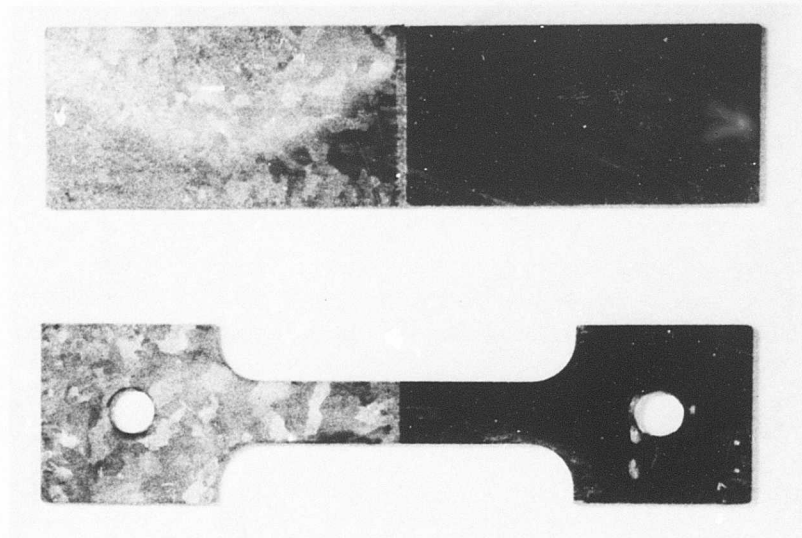Figure 50.   Electron-Beam-Welding
Test Specimens.

Figure 51. Electron-Beam-Welding Specimen
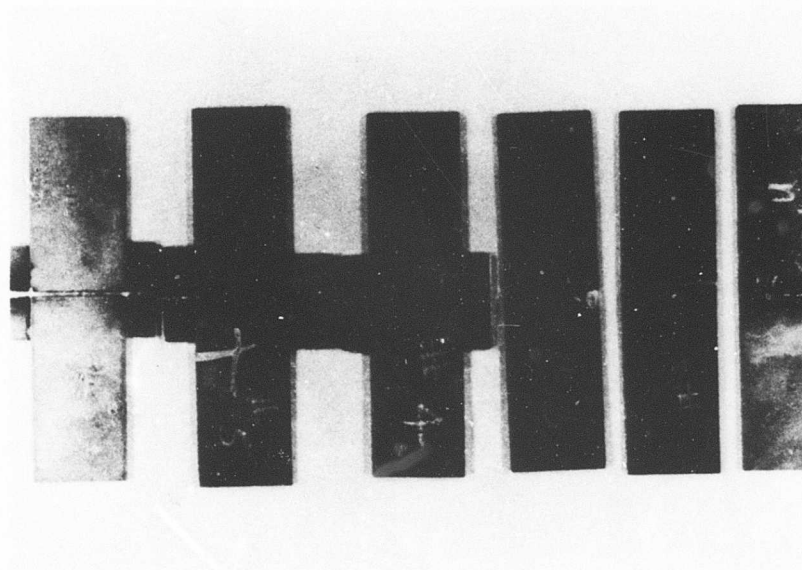After Welding and After Final
Machining.

Figure 52. Preliminary Electron-Beam-
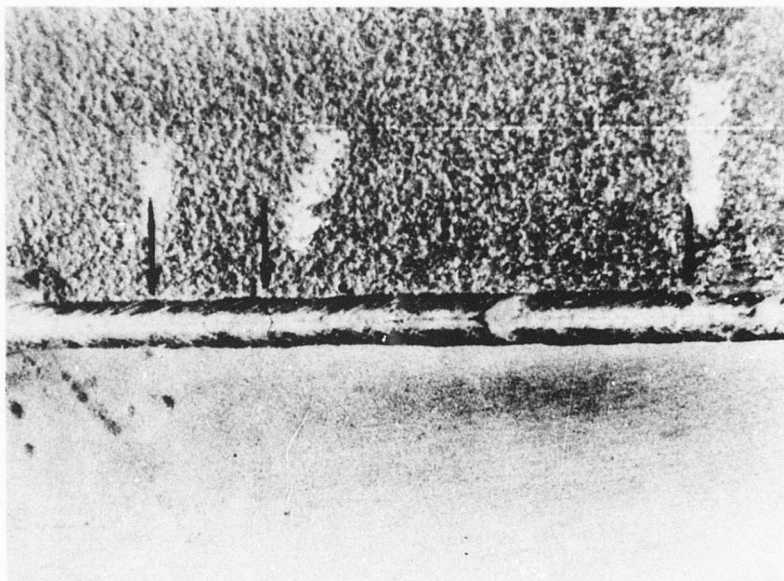Welding Specimens (Half-
Size).

99

Figure 53. Typical Cracks in Electron-Beam
Welds Joinint AF2-1DA to
MAR-M 246 (X10).

Specimen No.	Specimen Description	Heat-Treatment After Welding ⓐ	Test Temp ('F)	Yield (psi)	Ult (psi)	Elong (%)	Section Fractured
				TABLE XVI. TENSILE TEST RESULTS OF ELECTRON-BEAM-WELDED SPECIMENS			

Specimen No.	Specimen Description	Heat-Treatment After Welding ⓐ	Test Temp ('F)	Yield (psi)	Ult (psi)	Elong (%)	Section Fractured
35	Inconel 718 MAR-M 246	H.T. 5071	Room	123,100	133,100	2.5 ⓑ	MAR-M 246
36	Inconel 718 Mar-M 246	H.T. 5071	Room	130,800	133,500	ⓒ	MAR-M 246
37	Inconel 718 MAR-M 246	H.T. 5071	Room	129,000	133,100	3.0	MAR-M 246
38	Inconel 718 MAR-M 246	H.T. 5071	Room	58,000	58,600	ⓑ	MAR-M 246
31	Inconel 718 Mar-M 246	H.T. 5071	1200	130,500	144,700	3.0	MAR-M 246
32	Inconel 718 MAR-M 246	H.T. 5071	1200	125,500	144,300	3.0	MAR-M 246
33	Inconel 718 MAR-M 246	H.T. 5071	1200	131,000	143,000	4.5	MAR-M 246
34	Inconel 718 MAR-M 246	H.T. 5071	1200	132,000	149,000	4.5	MAR-M 246
40	Waspaloy MAR-M 246	AMS 5544	Room	128,000	129,500	0.5	MAR-M 246
41	Waspaloy MAR-M 246	AMS 5544	Room	135,000	140,000	**	MAR-M 246
42	Waspaloy MAR-M 246	AMS 5544	Room	161,000	162,000	1.0	MAR-M 246
39	Waspaloy MAR-M 246	AMS 5544	Room	54,200	64,000	1.0	MAR-M 246
6	Waspaloy MAR-M 246	None	Room	64,000	120,100	41	Waspaloy
7	Waspaloy MAR-M 246	None	Room	68,400	123,400	37	Waspaloy
8	Waspaloy MAR-M 246	None	Room	66,500	125,000	43	Waspaloy
43	Waspaloy MAR-M 246	AMS 5544	1200	125,000	169,000	3.5	MAR-M 246
44	Waspaloy MAR-M 246	AMS 5544	1200	137,200	163,200	4.5	MAR-M 246
45	Waspaloy MAR-M 246	AMS 5544	1200	126,000	156,200	2.0	MAR-M 246
46	Waspalov MAR-M 246	AMS 5544	1200	109,900	138,200	2.5	MAR-M 246
3	Waspaloy MAR-M 246	None	1200	58,400	104,100	31	Waspaloy
4	Waspaloy MAR-M 246	None	1200	58,000	101,500	36	Waspaloy
5	Waspaloy MAR-M 246	None	1200	57,400	100,000	34	Waspaloy
14	Waspaloy AF2-1DA	None	Room	70,400	123,400	43	Waspaloy
15	Waspaloy AF2-1DA	None	Room	68,400	119,600	42	Waspaloy

101

		TABLE XVI - Continued					
Specimen No.	Specimen Description	Heat-Treatment After Welding	Test Temp (°F)	Yield (psi)	Ult (psi)	Elong (%)	Section Fractured
16	Waspaloy/ AF2-1DA	None	Room	66,500	109,500	12	Weld
11	Waspaloy/ AF2-1DA	None	1200	62,500	101,800	30	Waspaloy
12	Waspaloy/ AF2-1DA	None	1200	55,300	103,000	28	Waspaloy
13	Waspaloy/ AF2-1DA	None	1200	58,400	102,000	36	Weld Waspaloy
21	AF2-1DA/ MAR-M 246	None	Room	105,600	135,500	4	MAR-M 246
27	AF2-1DA/ MAR-M 246	None	Room	105,000	138,200	4	MAR-M 246
29	AF2-1DA/ MAR-M 246	None	Room	127,000	128,500	ⓒ	MAR-M 246
30	AF2-1DA/ MAR-M 246	None	Room	ⓓ	136,400	55	MAR-M 246
25	AF2-1DA/ MAR-M 246	None	1200	111,000	126,000	7	MAR-M 246
26	AF2-1DA/ MAR-M 246	None	1200	114,000	137,000	3	Weld
28	AF2-1DA/ MAR-M 246	None	1200	95,200	105,600	3	Weld
17	AF2-1DA/ AF2-1DA	None	Room	96,000	168,000	18 ⓑ	AF2-1DA
18	AF2-1DA/ AF2-1DA	None	Room	99,000	162,800	14 ⓑ	AF2-1DA
19	AF2-1DA/ AF2-1DA	None	Room	92,800	162,000	13 ⓑ	AF2-1DA
20	AF2-1DA/ AF2-1DA	None	1200	109,000	140,000	10	AF2-1DA
22	AF2-1DA/ AF2-1DA	None	1200	106,000	138,000	8	AF2-1DA

ⓐ Heat Treatments
H.T. 5071 - (Inconel 718 aging treatment)
1300°F/8 hours to 1150°F in 2 hours and hold for 8 hours at 1150°F.

AMS5544 - (Waspaloy aging treatment)
1550°F/4 hours; 1400°F/16 hours.

ⓑ Broke in punch marks
ⓒ Broke outside gauge length
ⓓ Unavailable

TABLE XVII. SUMMARY OF TENSILE-TEST RESULTS ON ELECTRON-BEAM-WELDED SPECIMENS

Material Combination	Post-Weld Heat Treatment	Test Temp (°F)	Mean Yield Strength (psi)	Mean Ultimate Strength (psi)	Mean Elongation (%)	Section Fractured
Inconel 718/ MAR-M 246	H.T. 5071	Room	127,633	133,233	2.8	MAR-M 246
Inconel 718/ MAR-M 246	H.T. 5071	1200	129,750	145,250	3.8	MAR-M 246
Waspaloy/ MAR-M 246	AMS5544	Room	141,33	143,833	0.8	MAR-M 246
Waspaloy/ MAR-M 246	AMS5544	1200	124,525	156,650	3.1	MAR-M 246
Waspaloy/ MAR-M 246	None	Room	66,300	122,833	40.0	Waspaloy
Waspaloy/ MAR-M 246	None	1200	57,933	101,866	33.7	Waspaloy
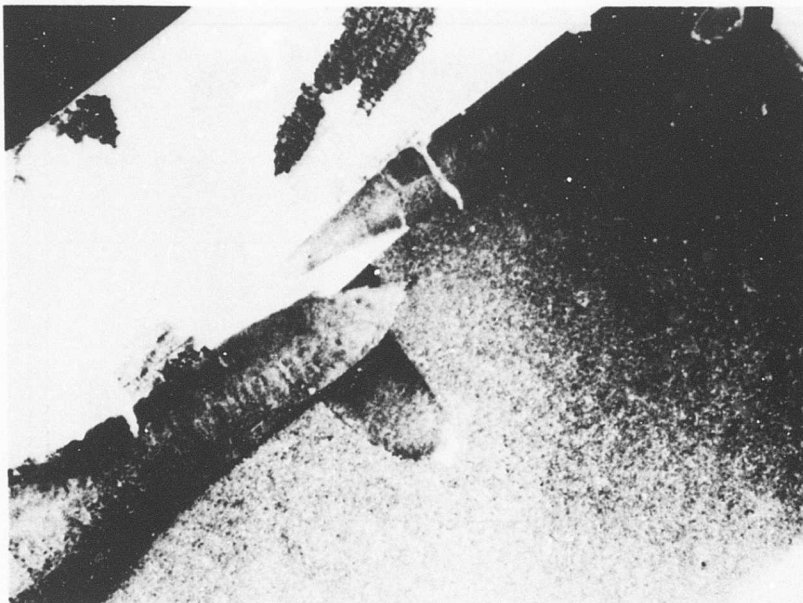
Figure 54.   Electron–Beam–Welded Joint Produced by
             Welding From Both Sides. (Total Thickness
             is 0.790 Inch. Note the Mismatch of the
             Two Weld Spikes.)
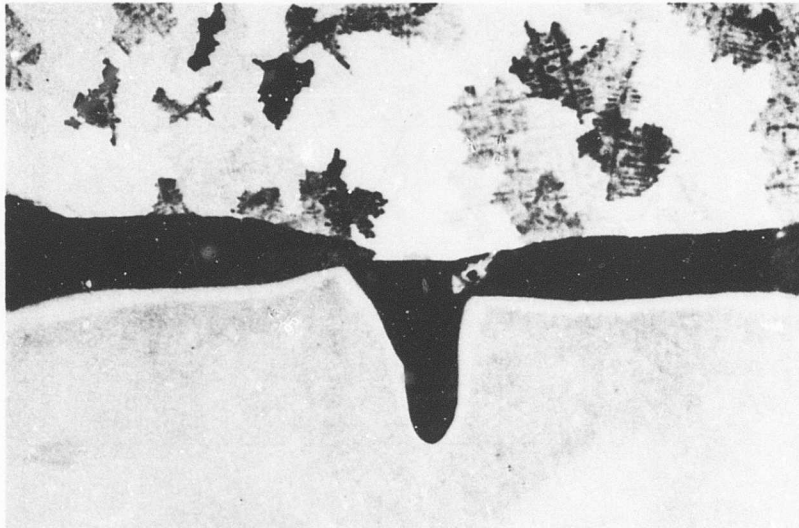
Figure 55.   Electron–Beam–Welded Joint Produced by
             Welding From Both Sides. (Total Thickness
             is 0.790 Inch. Note the Void at the
             Weld Overlap Area.)
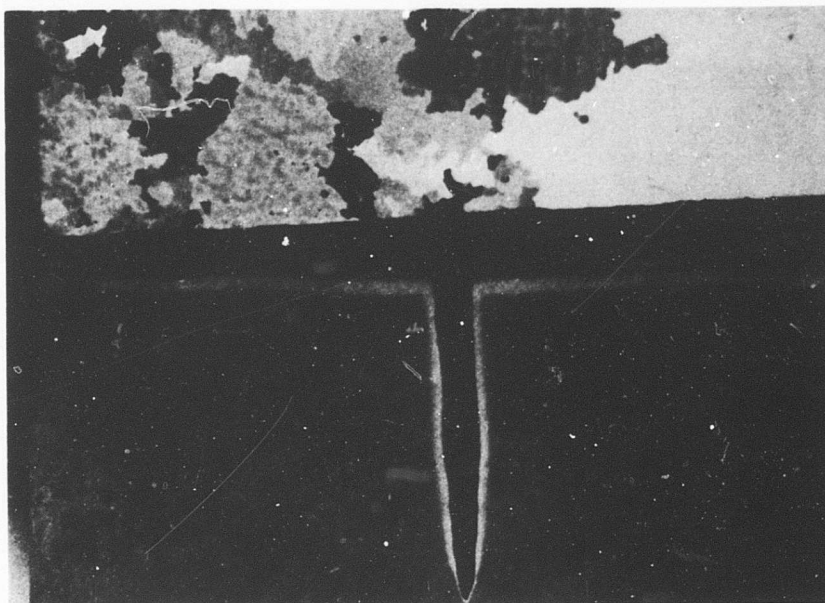
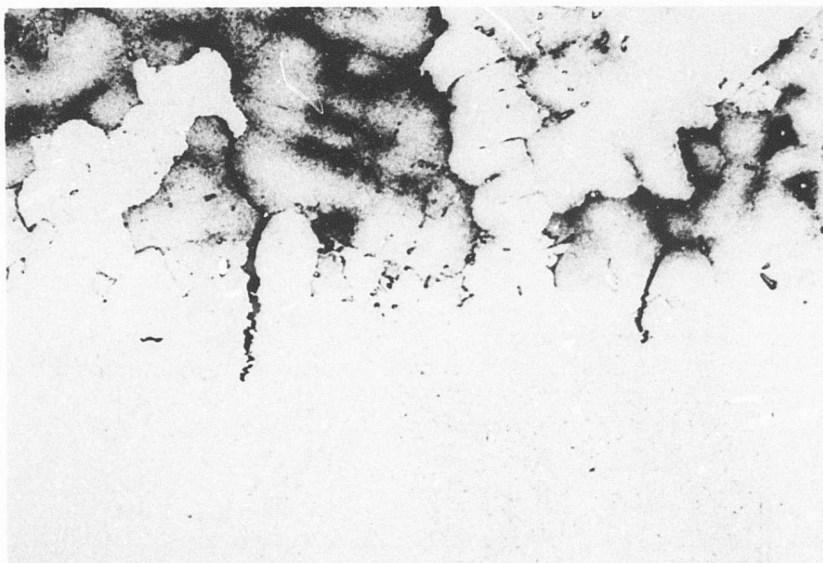Figure 56.   Single-Pass Electron-Beam-Welded
             Joint Developed for the Final
             Weld Specimens (X5).

Figure 57.   Example of the Minimum Amount of Cracking
             Achieved in Specimens Simulating Final
             Test Specimens.   The Material Combination
             is MAR-M 246/Waspaloy (X100).

105

4.2.4 Cast Bonding

The technique of casting one material against a second material to form a metallurgical bond was evaluated as a candidate means for strut/shell joining. The intent in this case was to form the blade from sheet material, place the blade into a die, preheat, and cast the molten strut material into the sheet metal blade. In this manner the strut would be cast and joined to the shell in the same operation. In the final design, cooling-air passages could be formed by preplacing refractory-metal wires against the shell prior to casting of the strut. Once the casting was complete, the wires could be oxidized out, leaving passages in the cast material through which cooling air could be channeled.

4.2.4.1 Experimental Procedure

To evaluate this technique, a die was designed in which one material could be cast against a second material to form an overlap joint which, in turn, could be tested for shear strength. An example of the die and final specimen is shown in Figure 58. The bonding procedure consisted of placing a piece of sheet material into the die and casting the second material against it. Parameters considered were melt pouring temperature, die preheat temperature, sheet specimen surface finish, and casting atmosphere. After the initial investigation to evaluate the potential for forming a bond, molybdenum wires were preplaced on the sheet specimen, as shown in Figure 59. These wires were successfully oxidized out to form simulated cooling-air passages.

Melting and casting were performed in the vacuum induction furnace shown in Figure 60. The furnace contained two independent induction coils—one to heat the crucible for melting of the charge and one to heat the mold so that the sheet metal could be preheated. Casting procedure consisted of evacuating the furnace to a vacuum of 10^{-4} microns and then backfilling with argon to a pressure of 10 psia. During the evacuating operation the mold and crucible were heated slowly to allow outgassing. Once backfilling was complete, the melted and preplaced sheet metal were brought to the desired temperatures, as indicated by optical measurements. The molten metal was then cast against the sheet and allowed to furnace-cool in the argon atmosphere.

106

Shear strengths of the bonds were evaluated by use of the test
apparatus that was used for the diffusion bonding shear test
of Section 4.2.1.1, (see Figure 38). This device held the
overlap specimen in such a manner that the shear strength
could be determined by using a Riehle tensile testing machine
to apply a shear load to the specimen.

Once the fabrication parameters and test data were determined,
a series of specimens was prepared with preplaced molybdenum
wires (0.040 inch in diameter) on the sheet material. After
casting, the wires were removed by alternate exposures to an
oxidizing atmosphere (1500°F) and to a potassium hydroxide
solution, which left simulated cooling-air passages. These
specimens were subsequently shear tested.

4.2.4.2   Test Results and Conclusions

Initial attempts to form a cast bond consisted of casting
MAR-M 246 against AiResist 213 with use of a melt temperature
of 2650°F and a die temperature (temperature of the AiResist
213 sheet) of 1200°F. The sheet specimen was prepared by
polishing through 600-grit followed by a cleaning operation.
These parameters produced only a superficial bond. A series
of specimens was then prepared with use of a melt temperature
of 2750°F and a mold temperature of 1650°F. Although a good
bond was produced under these conditions, metallographic
examination indicated some cracking in the cast material, as
shown in Figure 61. An increase in mold temperature to 2000°F
resulted in good bonds; thus, the final bonding parameters
selected were a 2750°F melt temperature and a 2000°F mold tem-
perature. Two examples of joints produced under these condi-
tions are shown in Figure 62. The apparent differences in the
joints indicate the amount of variability possible from joint
to joint.

Results of shear testing are summarized in Table XVIII. Al-
though good shear strengths were achieved in some cases, the
large variation in strengths indicates some lack of reproduci-
bility. However, the feasibility of this technique was demon-
strated. Additional development effort could well prove it to
be an effective method of forming intricate cooling passages
in a cooled blade. However, the evaluation was terminated at
this point since the principal attachment effort was directed
toward the strut/disk joint rather than the sheet metal shell/
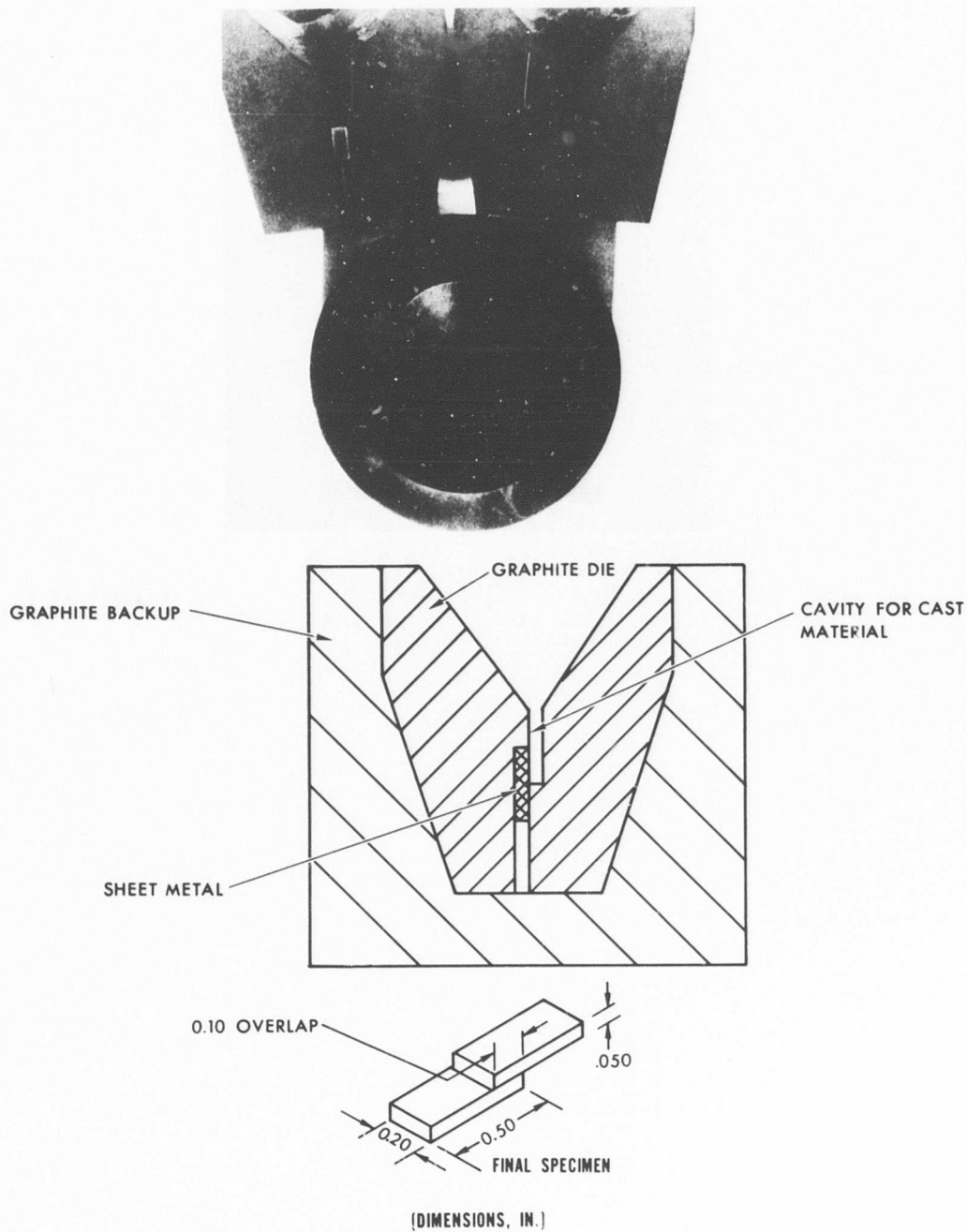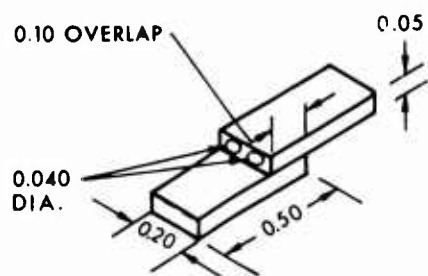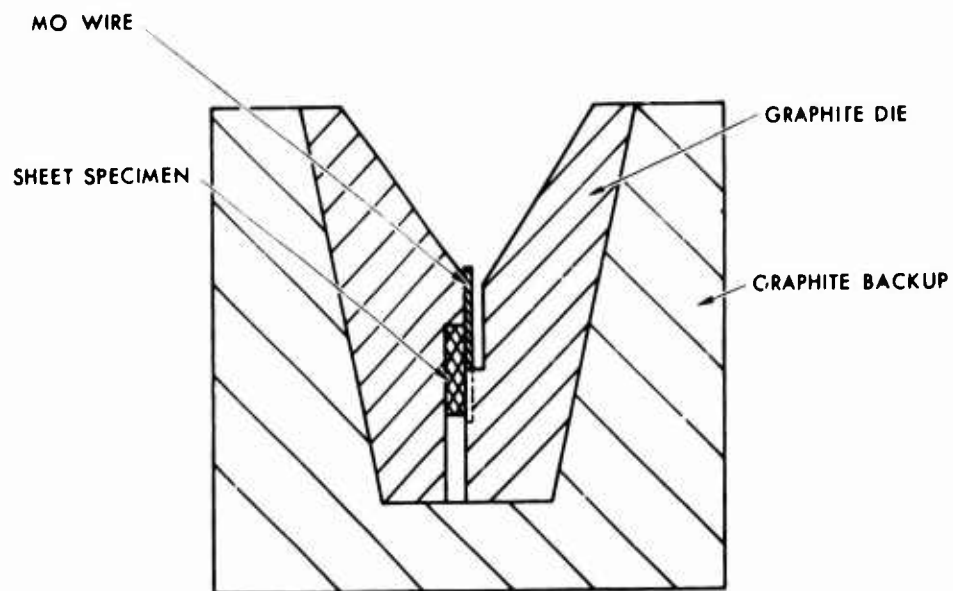strut joint.

07

GRAPHITE DIE

GRAPHITE BACKUP

CAVITY FOR CAST MATERIAL

SHEET METAL

0.10 OVERLAP

.050

0.20

0.50

FINAL SPECIMEN

(DIMENSIONS, IN.)

Figure 58. Die Arrangement for Forming Cast-
Bonding Test Specimens.

MO WIRE

SHEET SPECIMEN

GRAPHITE DIE

GRAPHITE BACKUP

0.10 OVERLAP

0.05

0.040
DIA.

0.20

0.50

FINAL SPECIMEN

(DIMENSIONS, IN.)

Figure 59. Die Arrangement and Specimen
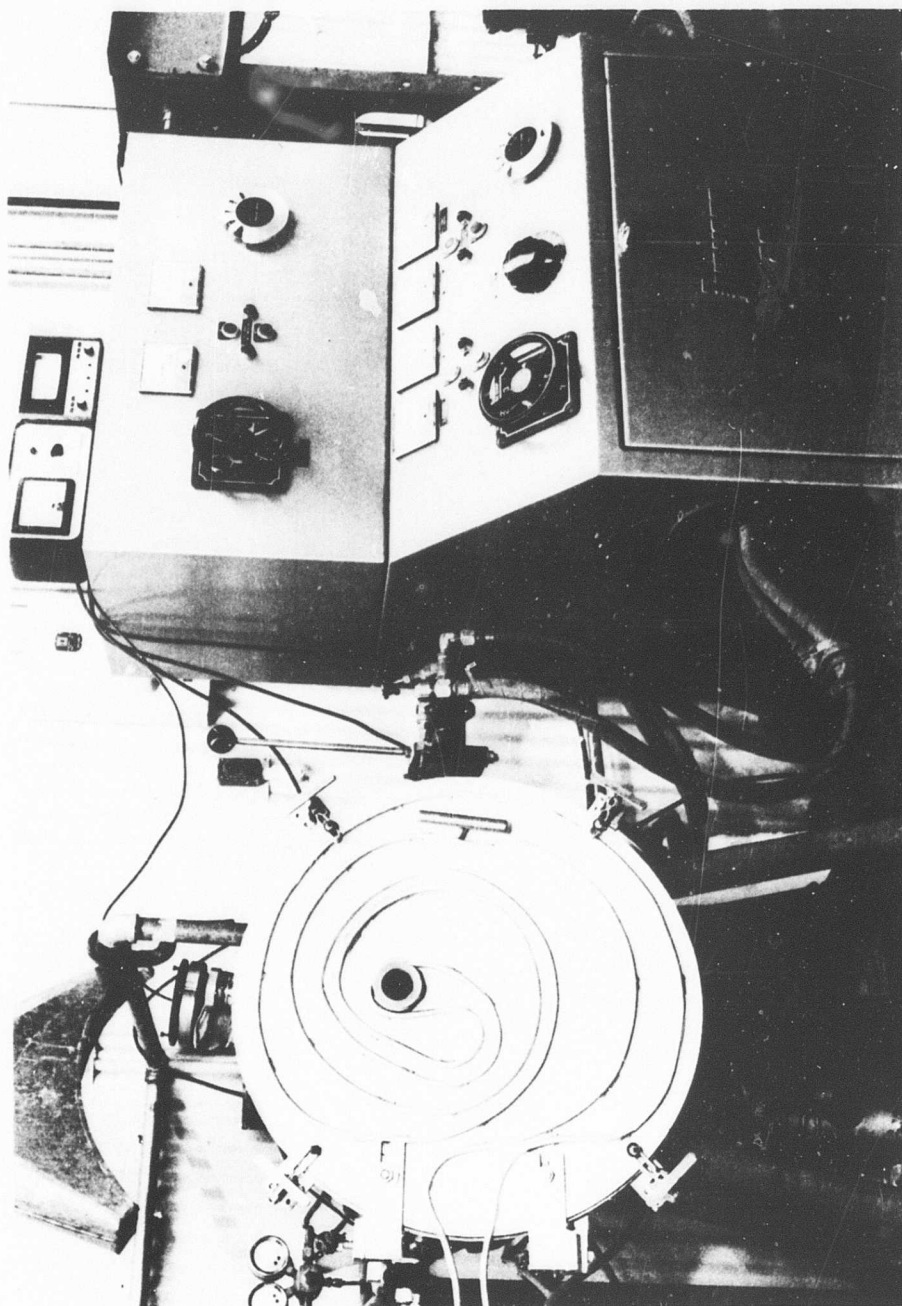Produced by Cast Bonding With
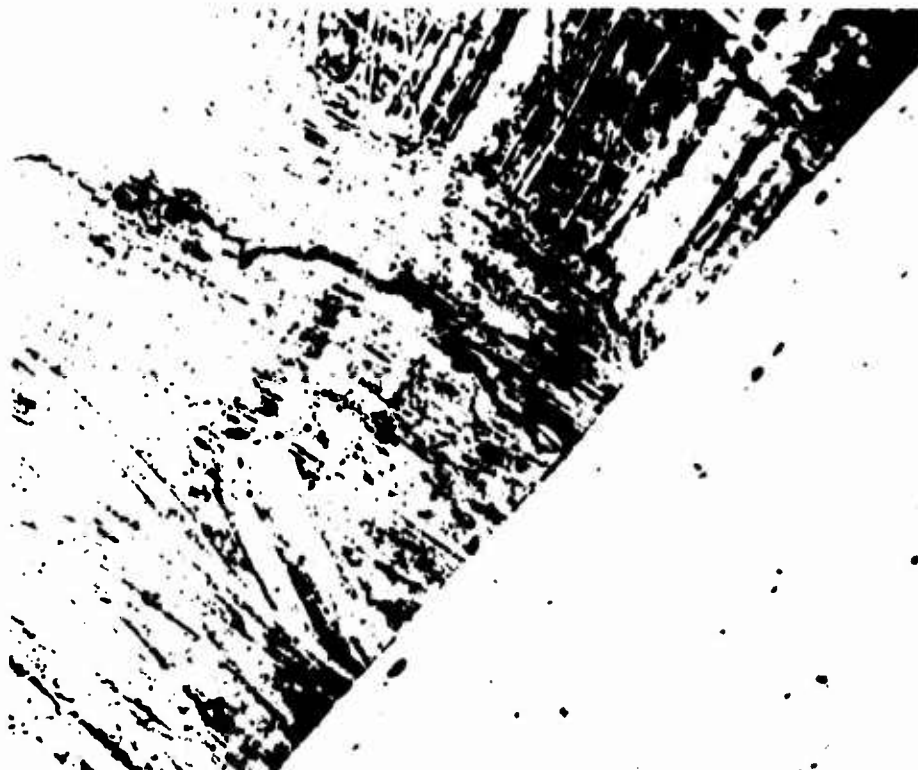Preplaced Molybdenum Wires.

Figure 60. Vacuum Induction Furnace.

110

Figure 61. Photomicrograph of the Interface of
a Cast Bond Showing Cracking in the
Cast Material Typical of That
Resulting From Insufficient Preheat
of the Sheet Material (X200).
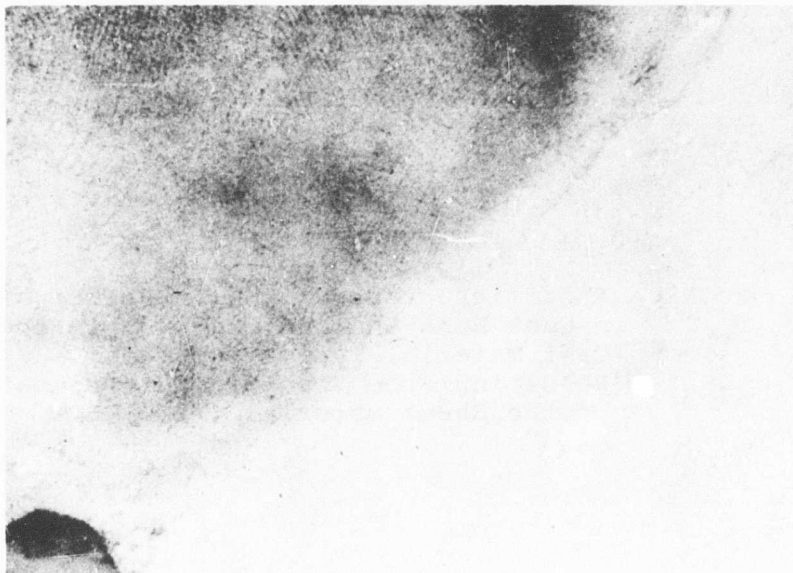
Figure 62. Examples of Cast-Bonded Joint
Produced Using Final Casting
Parameters (X50).

112

TABLE XVIII. RESULTS OF SHEAR TESTING CAST-TO-SHEET BONDED SPECIMENS

Specimen No.	Specimen Description	Bonding Conditions Mold Temp/Melt Temp	Apparent Shear Stress (psi)
C-1	MAR-M 246/AiR* 213	2000°F/2700°F	57,800
C-2	MAR-M 246/Rene' 41	2000°F/2750°F	19,300
C-8	MAR-M 246/AiR 213	2000°F/2750°F	19,500
C-9A	MAR-M 246/AiR 213	2000°F/2750°F	5700
C-9B	MAR-M 246/AiR 213	2000°F/2750°F	21,400
C-10	**MAR-M 246/AiR 213	2000°F/2750°F	64,200
C-11	**MAR-M 246/AiR 213	2000°F/2750°F	51,300
C-12	**MAR-M 246/AiR 213	2000°F/2750°F	31,900
C-13	**MAR-M 246/Rene' 41	2000°F/2750°F	13,200
C-14	**MAR-M 246/Rene' 41	2000°F/2750°F	68,500

*AiR - AiResist

**Preplaced Mo Wire (0.040-in. diam) removed chemically.

113

4.3 SELECTION OF FINAL CANDIDATE JOINING PROCESSES

4.3.1 Strut/Disk Attachment

The candidate joining processes and associated material com-
binations selected for final testing are listed below:

1. Diffusion bonding with blade material of
   MAR-M 246 and disk material of Inconel 718.

2. Brazing with blade material of MAR-M 246
   and disk material of Waspaloy.

3. Electron-beam welding with blade material
   of MAR-M 246 and disk material of Waspaloy.

4.3.2 Shell/Strut Attachment (Feasibility Study)

The preliminary joining evaluation for the shell/strut attach-
ment indicated the following:

1. Diffusion bonding was shown to be a feasible
   technique. However, additional development
   would be required to achieve bonding in the
   component geometries required for a blade.

2. Shell/strut joining could be accomplished by
   brazing. However, this type of joint is con-
   sidered unattractive because of the relatively
   low stress-rupture life of the braze alloys at
   the operating temperature of the shell/strut
   joint.

3. The cast-bonding technique offered a potential
   means of forming the strut and shell/strut
   bonding in one operation. Use of preplaced
   wires that can be subsequently removed to
   form cooling-air passages was shown to be
   a feasible approach. However, additional
   development of the cast-bonding technique is
   required to produce scale-size specimens.

5. FINAL SPECIMEN FABRICATION AND TESTING

This section describes the final specimen design, fabrication, and testing activities that concluded the blade/disk fabrication program.

The objectives of this program phase were to design, fabricate, inspect, test, and evaluate the test results of the final specimens. These specimens (diffusion-bonded, brazed, and electron-beam-welded) were configured to closely simulate the actual requirements for a turbine rotor.

5.1 SPECIMEN DESIGN

The final specimen design was based on the accumulated technology and experience gained from the aerothermodynamic design, mechanical design, and fabrication technology development efforts described in Sections 2, 3, and 4. The specimens were designed to simulate as closely as possible the geometry that would be required for the blade-disk attachment of an actual turbine rotor.

Subsequent subparagraphs describe the design for the diffusion bonded, brazed, and electron-beam-welded specimens, respectively.

5.1.1 Diffusion-Bonded Specimen Design

The specimen that was designed to simulate the diffusion-bonded attachment design concept is shown in Figure 63. The threaded end of the illustrated specimen simulates the blade pedestal element of the attachment. The pin-joint end simulates the two disk halves. The geometry of the final specimen design differed from that of the diffusion-bonded rotor design (Figure 24) as follows:

1. The bonded surfaces of the final specimen are defined by a rectangle rather than by the trapezoidal configuration of the diffusion-bonded rotor design.

2. No cooling-air entry holes were included in the final specimen design. Considerations of bond joint strength versus the load-carrying ability of the blade pedestal element of the attachment showed that the holes would have negligible effect upon the strength of the attachment.
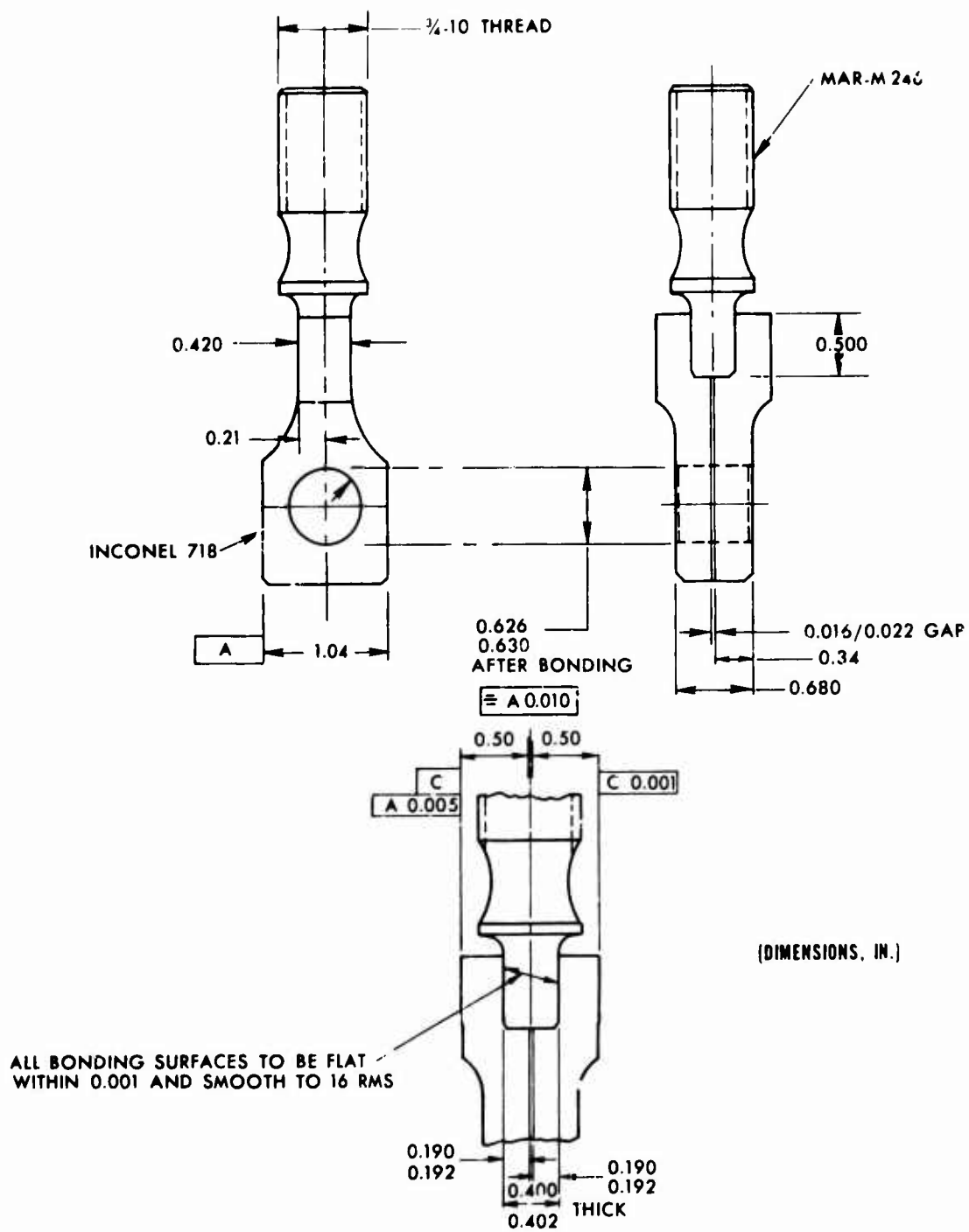
115

¾-10 THREAD

MAR-M 246

0.420

0.500

0.21

INCONEL 718

A

1.04

0.626
0.630
AFTER BONDING

A 0.010

0.016/0.022 GAP

0.34

0.680

0.50   0.50

C

C 0.001

A 0.005

(DIMENSIONS, IN.)

ALL BONDING SURFACES TO BE FLAT
WITHIN 0.001 AND SMOOTH TO 16 RMS

0.190
0.192

0.190
0.192

0.400
0.402

THICK

Figure 63. Diffusion-Bonded Final
Specimen Design.

116

3. The disk elements of the final specimen were not designed to include simulation of the holes that relieve stress concentrations in the rotor assembly. Considerations of bond joint strength versus the load-carrying ability of the disk elements of the final specimen showed that the holes would have negligible effect upon the strength of the attachment.

5.1.2 Brazed Specimen Design

The specimen that was designed to simulate the brazed attachment concept is shown in Figure 64. The female component of the illustrated specimen simulates the blade pedestal element of the attachment, and the male component simulates the disk. The geometry of the final specimen design differed from that of the brazed-joint rotor design (Figure 25) as follows:

1. No cooling-air entry holes were included in the final specimen design. Analysis of the design indicated that these holes would have a negligible effect upon the strength of the attachment.

2. A full radius was provided at the bottom of the slotted blade pedestal of the final specimen rather than the two-radius configuration shown for the brazed-joint rotor design in an attempt to minimize stress concentrations.

5.1.3 Electron-Beam-Welded Specimen Design

The specimen that was designed to simulate the electron-beam-welded attachment concept is shown in Figure 65. The upper component simulates the blade pedestal element of the attachment. The other component simulates the disk. No differences from the geometry of the electron-beam-welded rotor design (Figure 26) were allowed in this final specimen design. The reason for this complete compliance is that the geometry of the joint, including the cooling-air entry passage, is considered to have a strong effect upon low-cycle-fatigue and stress-rupture-life characteristics of the attachment. Additionally, it was believed that welding the specimens individually would not provide a true simulation of the welding requirements associated with fabrication of a complete rotor assembly. Therefore, the specimens were welded in groups of six to more nearly simulate the attachment of blades to a rotor disk.
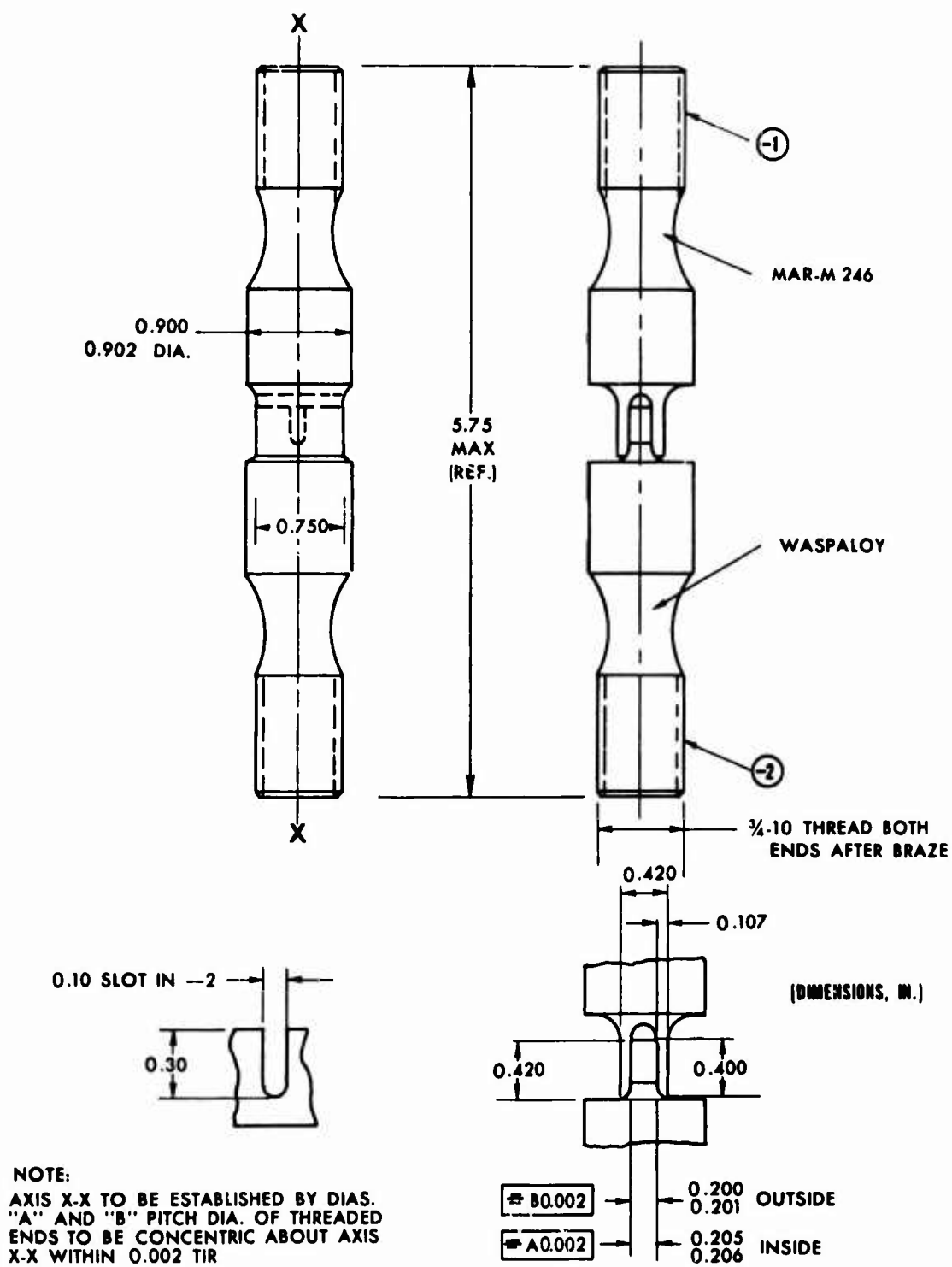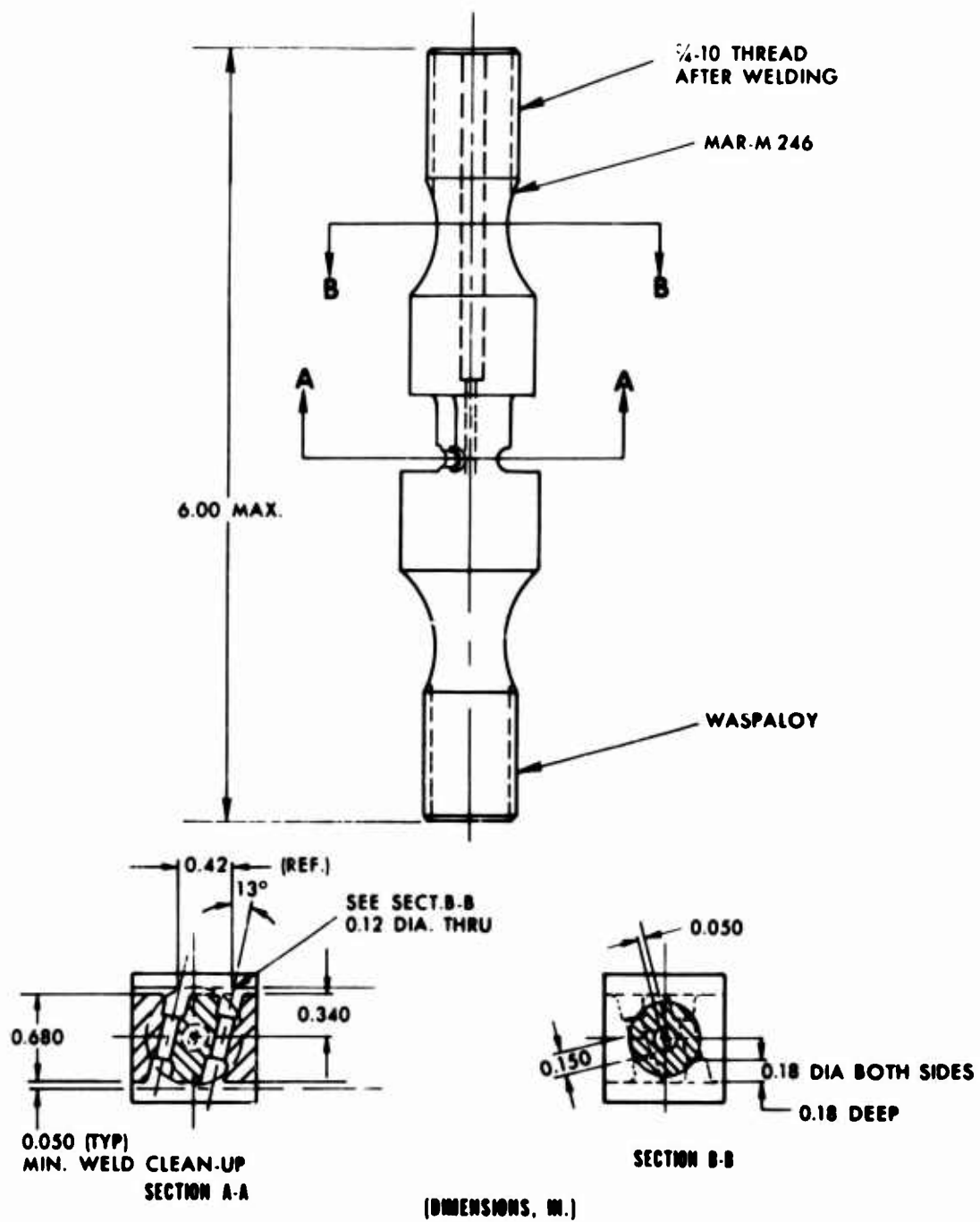
117

Figure 64. Brazed Final Specimen Design.

Figure 65. Electron-Beam-Welded Final
            Specimen Design.

119

5.2 SPECIMEN FABRICATION

Three alloys were required for fabrication of the final speci-
mens: Inconel 718, Waspaloy, and MAR-M 246. The wrought
materials (Inconel 718 and Waspaloy) were purchased in the
form of bars 1.25 by 3.25 inches in cross section and 1 foot
in length. The Inconel 718 was purchased to specification
AMS 5662B in the solution heat-treated condition, and the
Waspaloy material was purchased to Specification AMS 5707B
in the precipitation heat-treated condition and was solution
heat-treated (1850°F for 4 hours) prior to machining. The
MAR-M 246 material was purchased in the form of cast blocks
1.25 by 1.25 by 3 inches in size. Casting was performed
in inoculated molds in an attempt to produce the small grain
size considered desirable for welding.

Certified compositions for each of these three types of mate-
rial are listed in Table XIX.

Subsequent subparagraphs describe the fabrication sequence
for the diffusion-bonded, brazed, and electron-beam-welded
specimens.

TABLE XIX. CERTIFIED COMPOSITIONS FOR MATERIALS USED IN THE FINAL TEST SPECIMENS			
Element	Inconel 718	Waspaloy	MAR-M 246
C	0.043	0.038	0.14
Mn	0.10	0.03	0.10
P	0.008	0.007	-
S	0.006	0.004	0.003
Si	0.16	0.10	0.10
Cr	18.60	19.91	8.76
Ni	52.40	Bal.	Bal.
Cu	0.03	0.02	-
Mo	3.18	4.27	2.42
Ti	0.89	3.00	1.40
Cb/Ta	5.10	-	1.55
Al	0.55	1.31	5.50
Co	-	14.23	9.90
Zr	-	0.06	0.03
Fe	-	0.70	0.10
B	-	0.006	0.011
W	-	-	9.98

5.2.1 Diffusion-Bonded Specimen Fabrication

The fabrication sequence for the diffusion-bonded specimens is shown in Figures 66 through 70. Figure 66 shows the component parts of the specimen after preliminary machining. The center piece (threaded) was of MAR-M 246 to simulate the blade pedestal element, and the top and bottom pieces were machined from Inconel 718, simulating the disk. Although the preliminary test specimens described in Section 4.2.1.1 were polished to a No. 3 finish, the final specimens were left "as ground" with a surface finish of approximately 16 rms. This value was considered to be the practical limit for surface finish that could be tolerated in economically feasible designs of this type. An interface diffusion aid, consisting of 0.0005-inch nickel plating applied to the MAR-M 246 surfaces, was utilized for the diffusion-bonded attachment.

Figures 67 and 68 show the final specimen as assembled and as tack-welded prior to the bonding operation. Tack welding was required to ensure the maintenance of alignment during assembly of the specimen into the pressing die. These welds were superficial and in all cases were broken upon the application of bonding pressure, since some deformation occurred in the components. The final specimens were assembled with a shim in place, as shown in Figure 67, in order to maintain a small gap at the end and thus allow for some deformation without contact on surfaces that were not to be bonded.

The assembled and tack-welded final specimens were bonded in the graphite die shown in Figure 69. The specimens were placed in the die in such a way that the total load applied by the press was carried across the surfaces to be bonded. Equipment and procedures used for bonding were identical with those used for the diffusion-bonding preliminary test evaluations of Section 4.2.1. The die assembled with the final specimen in place was positioned in the pressing furnace, and the furnace chamber was evacuated to less than 1 micron pressure. As in the preliminary test, heating of the specimen to 1800°F was accomplished by induction heating of the graphite die, and the temperature was measured by a thermocouple positioned in the die wall. Once the required temperature was reached, the pressure was increased to 12,900 psi at the bonding interfaces and held for 30 minutes. These conditions resulted in the small amount of deformation of the specimen during the bonding that is required to help ensure a more complete joint contact. However, additional temperature or pressure application would have resulted in excessive deformation.

122

Upon completion of the bonding operation, the final specimens were final-machined as shown in Figure 70. Final machining was followed by heat treatment to develop full properties of the Inconel 718 material. The 1800°F temperature used for bonding was in the solution-heat-treating range for the Inconel 718 material; therefore, only the precipitation heat treatment was required. This consisted of 1325°F for 8 hours, cooling at 100°F per hour to 1150°F, and holding for 8 hours.

After completion of heat treatment, the specimens were ready for inspection and test. A clevis-type holder was prepared, as shown in Figure 71, for use on the pin joint end of the specimen during testing.
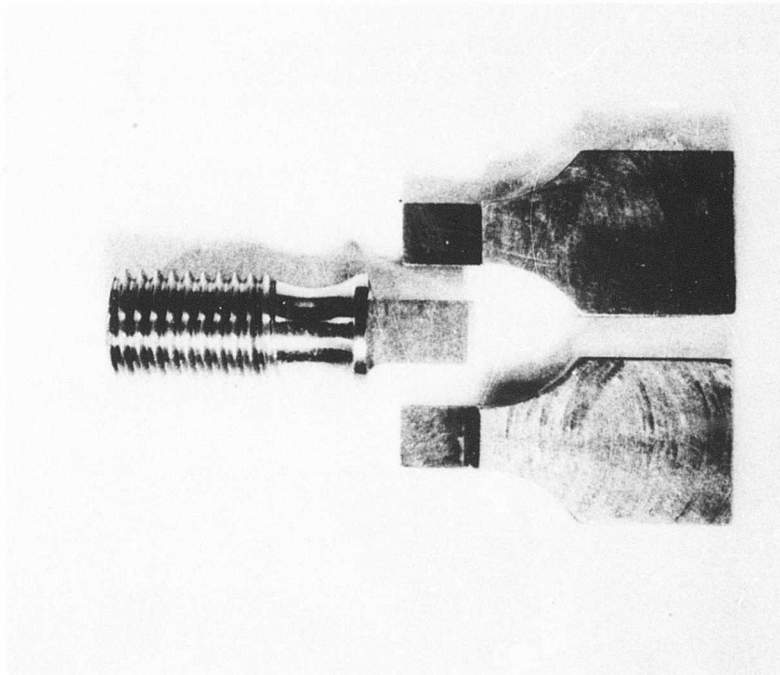
Figure 66.   Machined Diffusion-Bonded Final Specimen Elements Before Assembly.
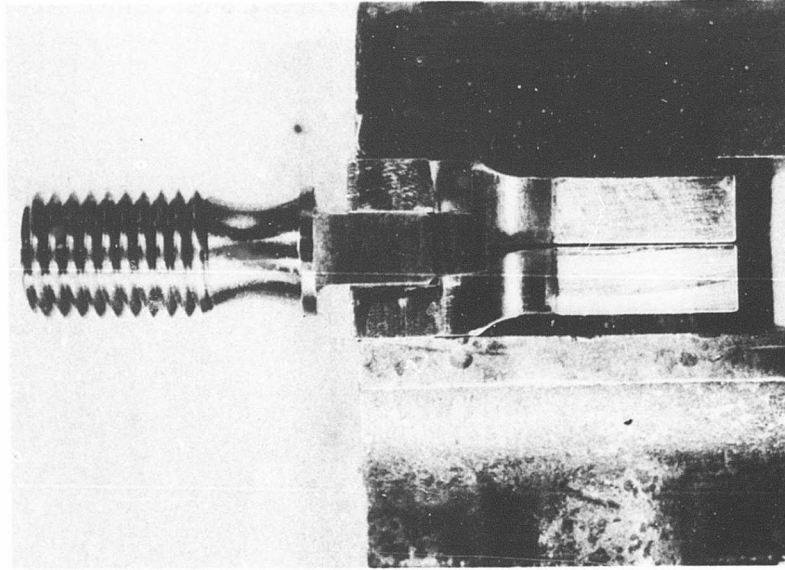
Figure 67. Diffusion–Bonded Final Specimen
Assembled in Vice With Shim
Installed Prior to Tack Welding.
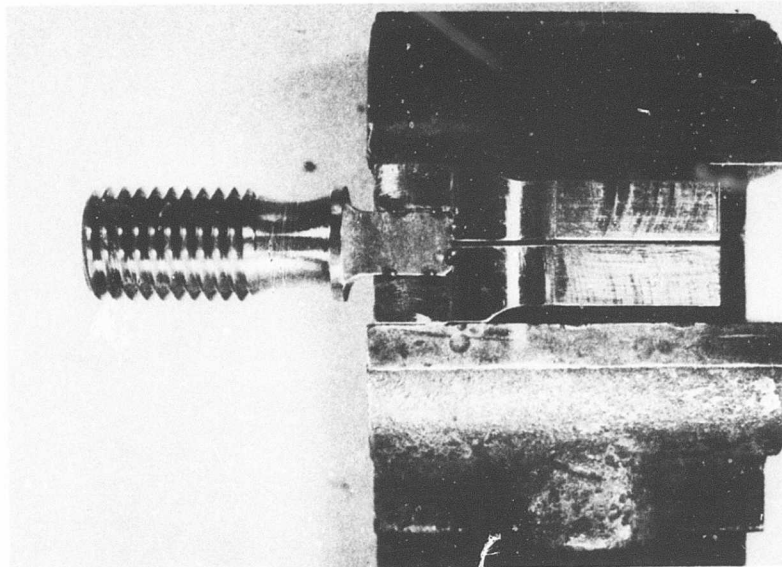
Figure 68. Diffusion–Bonded Final Specimen
With Shim Removed and Tack
Welding Complete.

124
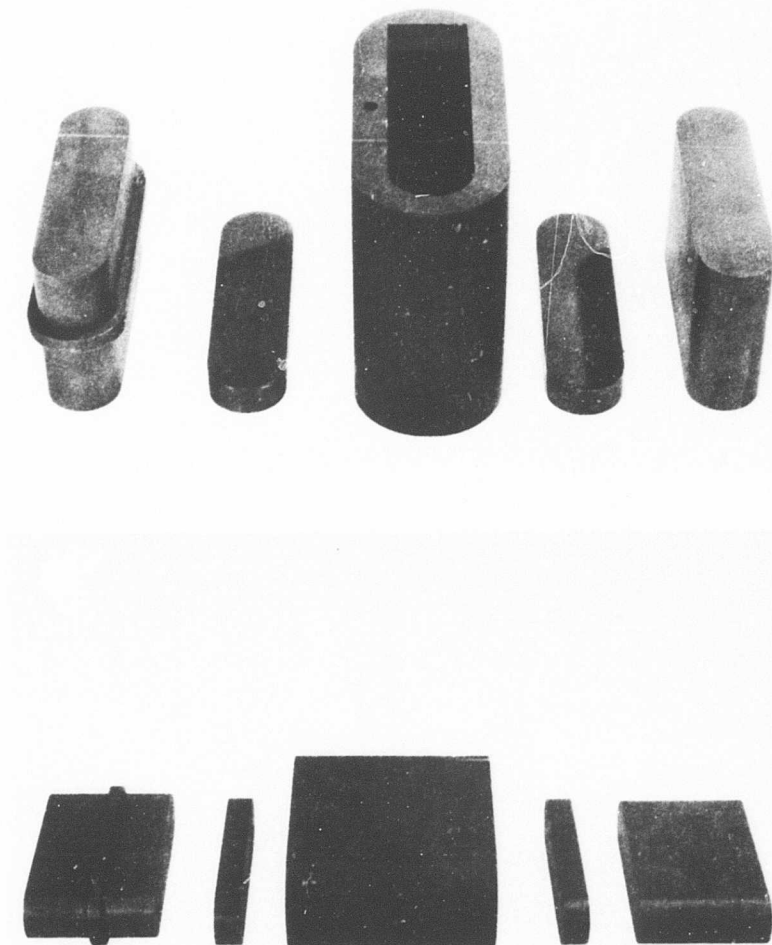
Figure 69. Two Views of the Graphite Die Assembly
Used During the Diffusion Bonding
Operation on the Final Specimen.

125
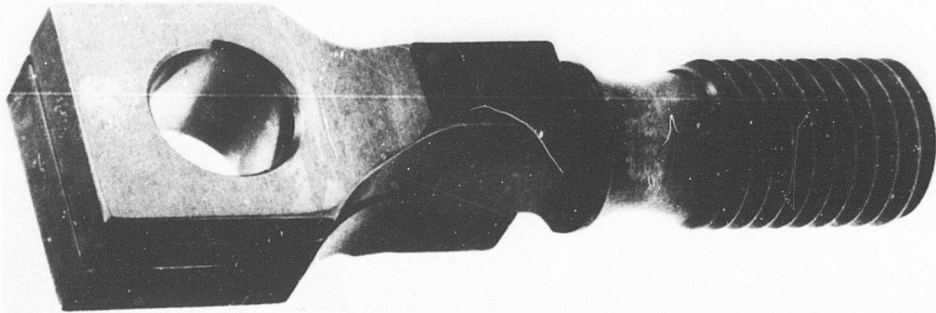
Figure 70. Diffusion-Bonded Final Specimen
After Completion of Bonding Operation
and Final Machining.
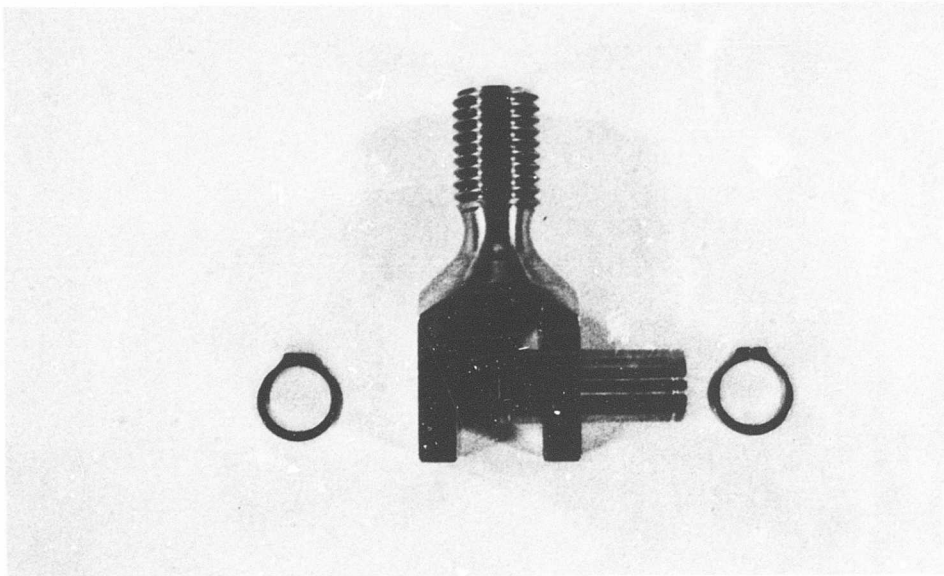
Figure 71. Clevis Assembly Used for Testing
of the Diffusion-Bonded Specimens.

126

5.2.2 Brazed Specimen Fabrication

The fabrication sequence for the brazed specimens is shown in Figures 72 through 76. Figure 72 shows the component parts of the specimen after preliminary machining. Materials used were MAR-M 246 to simulate the blade pedestal element and Waspaloy to simulate the disk. The portions of the final specimens upon which brazing flow was required were nickel-plated (0.0004 inch) to ensure adequate wetting of the surfaces. Nicrobraz 30 brazing powder in a paste form was preplaced on the final specimens prior to assembly in a jig.

The jig (Figure 73) consisted of a V-block on which the two parts could be clamped and held in proper alignment during the tack welding of spacers, as shown in Figure 74. These spacers served to maintain specimen alignment and gap during the brazing operation. Prior to brazing, a small excess of powder was placed in the fillet area to allow "feeding" of the joint during the brazing cycle.

As in the preliminary test evaluations of 4.2.2, brazing was performed in a vacuum furnace at a pressure of 0.5 micron and with a cycle of 2150° ±10°F for 20 minutes. An example of an as-brazed specimen is shown in Figure 75. Following the brazing cycle, specimens were heat-treated to develop full properties in the Waspaloy material. This treatment consisted of a stabilization treatment at 1550°F for 4 hours (air-cool) followed by a precipitation heat treatment at 1400°F for 16 hours (air-cool). Spacers were then cut, as shown in Figure 76, and the specimens were ready for test.
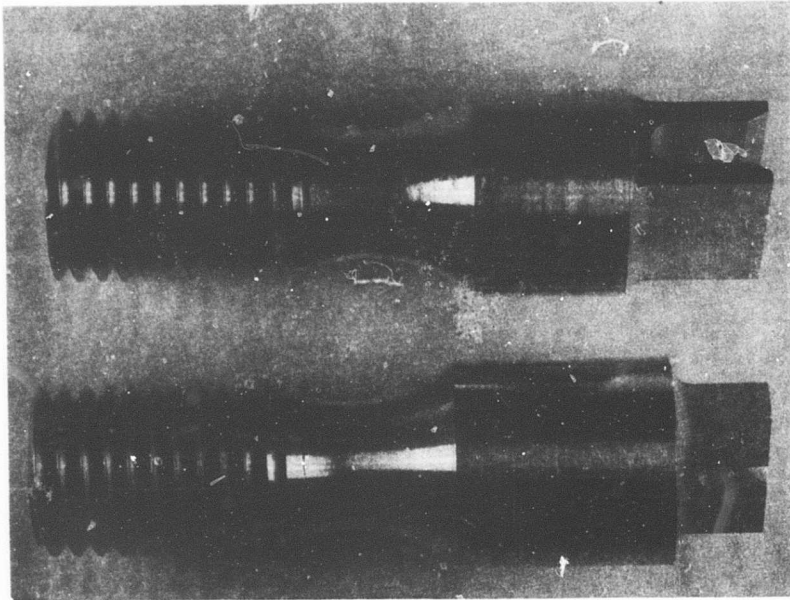
127

Figure 72.   Component Parts of the Brazed
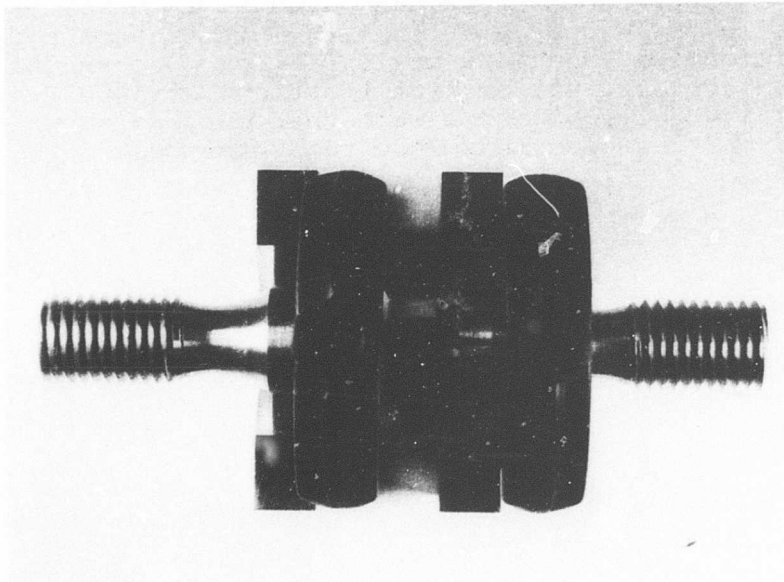Final Specimen After Final
Machining.

Figure 73.   Assembly Jig With the Brazed
Final Specimen in Place.
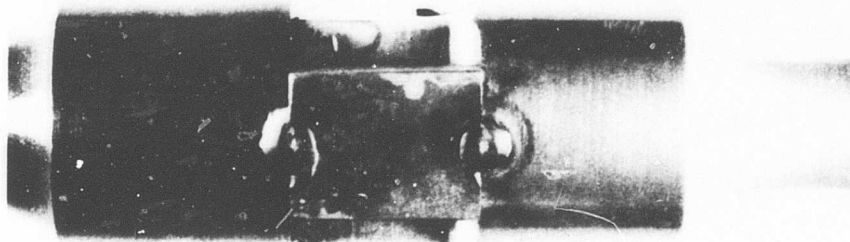
128

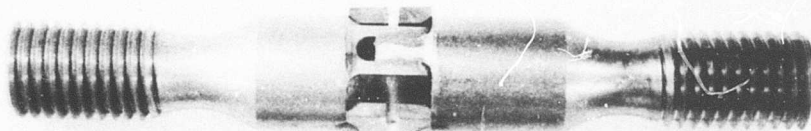Figure 74. Spacers Tack-Welded in Place on
Brazed Final Specimen.

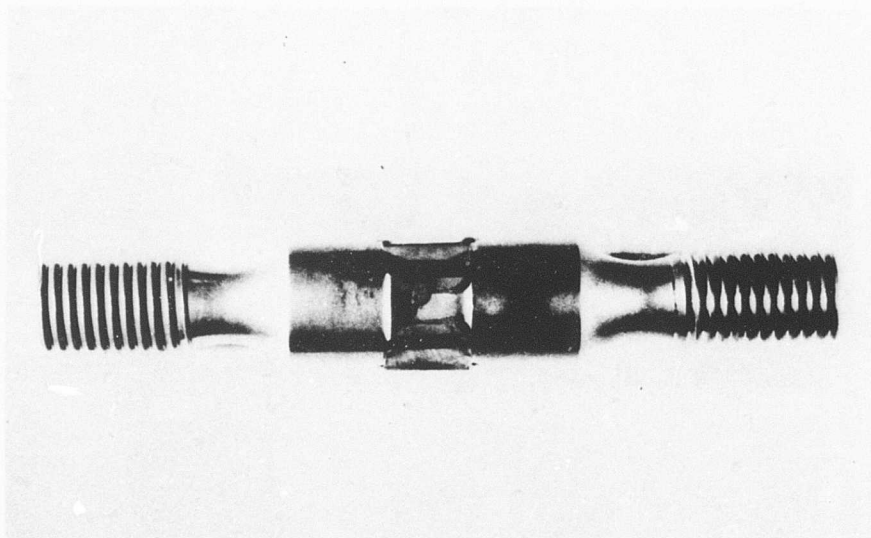Figure 75. Final Specimen After Completion
of Brazing Operation.

129

Figure 76. Brazed Final Specimen Ready for
Testing (Spacers Have Been Cut).

130

5.2.3 Electron-Beam-Welded Specimen Fabrication

The fabrication sequence for the electron-beam-welded speci-
mens is shown in Figures 77 through 85. Figure 77 shows the
machined Waspaloy block that simulated the disk material. As
shown in the figure, a single-pass weld was run the length of
the block to simulate the weld that would be required to join
the two halves of the disk together. A section through this
weld is shown in Figure 78. Blocks of the alloy MAR-M 246
(blade pedestal material) were given a heat treatment of 2000°F
for 2 hours prior to machining into the geometry shown in Fig-
ure 79. Experience gained during the electron-beam-welding pre-
liminary test evaluations had shown that such a heat
treatment tended to reduce the severity of weld cracking in
the MAR-M 246.

Machined MAR-M 246 blade pedestal blocks, with MAR-M 246 alloy
spacers, were assembled with the large Waspaloy disk block as
shown in Figure 79 and were clamped into the welding jig as
shown in Figure 80. The jig was designed to hold six of the
MAR-M 246 alloy blade pedestal blocks against a Waspaloy disk
block (Figure 77) during the welding operation. Due to the
geometry of the blade pedestal blocks, spacers were required
between each of the six blocks at the "root-end" to permit an
uninterrupted single-pass weld. A slight relief was machined
in the "root-end" of the spacer at the spacer/pedestal inter-
face. This relief was machined to help simulate an actual
rotor configuration where the blades are spaced 0.003 to 0.005
inch apart.

The assembled blocks (in the welding fixture) were welded by
a single-pass electron-beam weld with use of the parameters
listed in Table XX. In order to ensure complete and uniform
penetration, a weld backup strip was used, as shown in Figure
81. Figures 82 and 83 show front and back views, respectively
of a final specimen with the weld backup strip removed. The
welded assemblies were given a stress-relieving heat treatment
consisting of:

1. Heat to 1000°F and hold 30 minutes.

2. Heat to 1840°F rapidly and hold for 2 hours.

3. Argon-fan-cool in furnace to achieve as rapid
    a cooling rate as possible.

The stress-relieving heat treatment served to relieve welding
stresses and to solution the Waspaloy material so that it
could respond to subsequent heat treatment.

131

The assemblies were then cut apart, and individual specimens, as shown in Figure 84, were final-machined, including the hole through the blade pedestal base, to simulate a cooling-air passage. The final step in specimen preparation was the heat treatment of the specimen to develop full properties in the Waspaloy material. This treatment consisted of:

Stabilization   1550°F for 4 hours and
                               air-cool

Precipitation treatment   1400°F for 16 hours and
                               air-cool

Following this final heat treatment the specimens were ready for test. Figures 85 and 86 show front and back views of the joint-test section of an electron-beam-welded final specimen.

| TABLE XX. ELECTRON-BEAM WELDING PARAMETERS USED FOR FINAL TEST SPECIMENS		
Material – Waspaloy/MAR-M 246		Vacuum – 1 x 10 torr
Penetration – 0.790 inch		Operator Name – R. Custer
E. B. Machine Serial No. – H.S. 335		Gun Type – R-40
Accelerating Voltage – KV 140		Gun to Work Distance – 6"
Beam Current – ma	35	Beam Deflection – None
Travel Speed – I.P.M.	25	Joint Type – Butt/backup
Pot Setting – Speed	215	
SPECIAL TECHNIQUES: Spot-tack each blade and spacer.		
140 Kv		
3 ma		
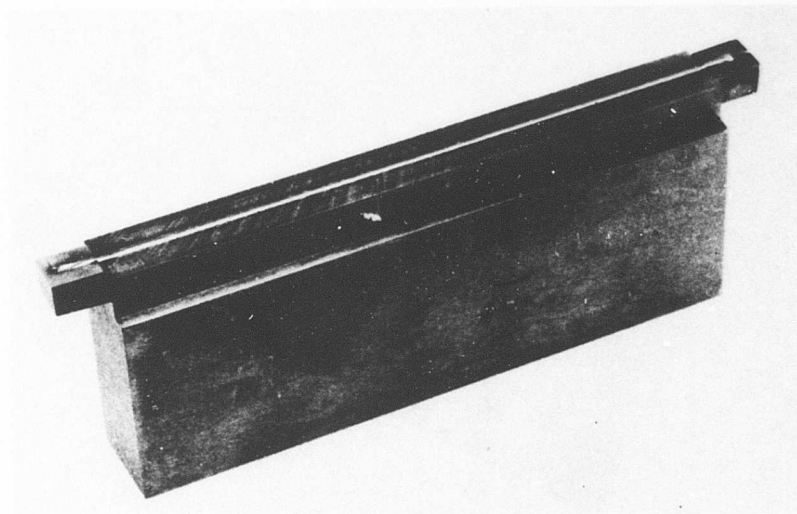
Figure 77.   Machined Waspaloy Block That
Simulated the Disk Element of the
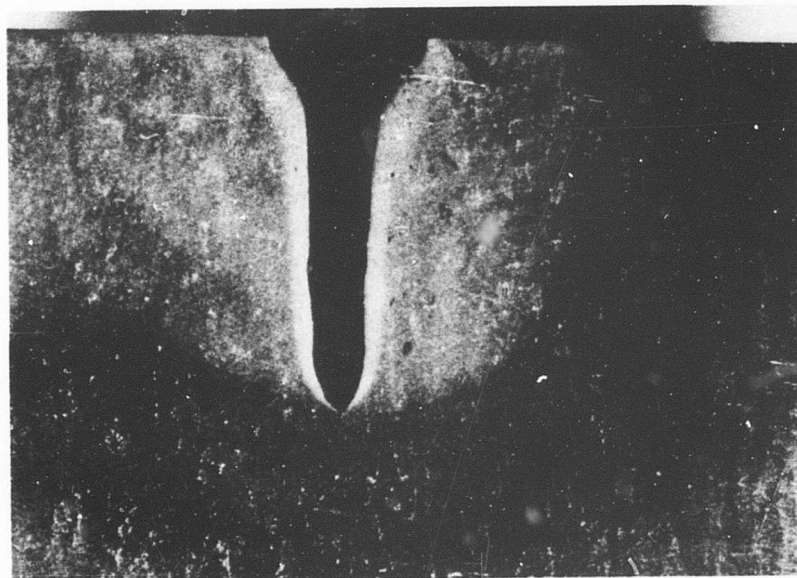Electron-Beam-Welded Final Specimen.

Figure 78.   Section Through Single-Pass
Weld of Electron-Beam-Welded
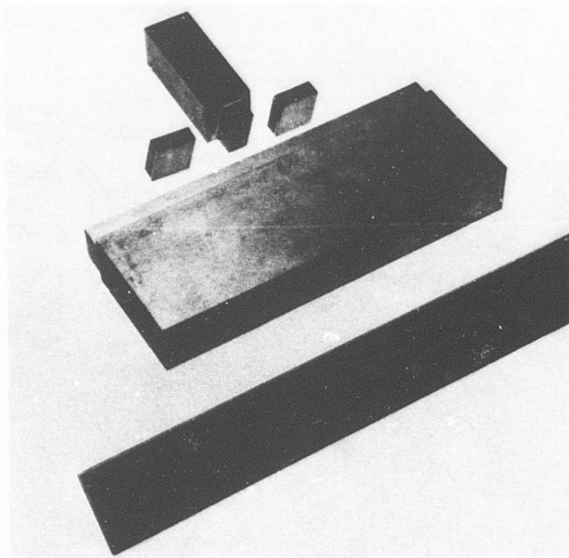Final Specimen Disk Element.

133

Figure 79. Elements of Electron-Beam-Welded
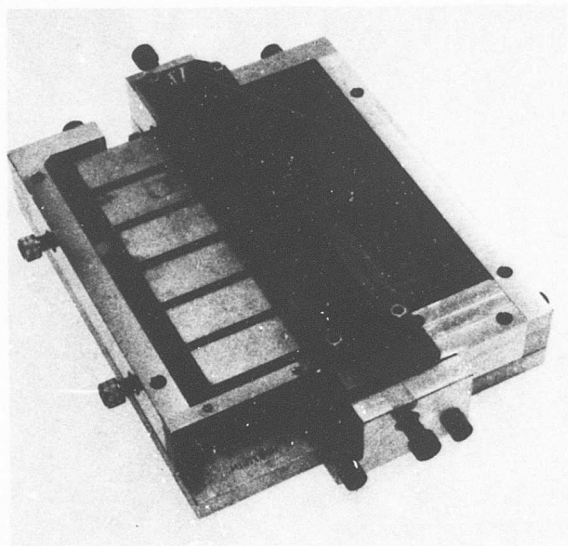Final Specimens Prior to Joining.

Figure 80. Elements of Electron-Beam-Welded
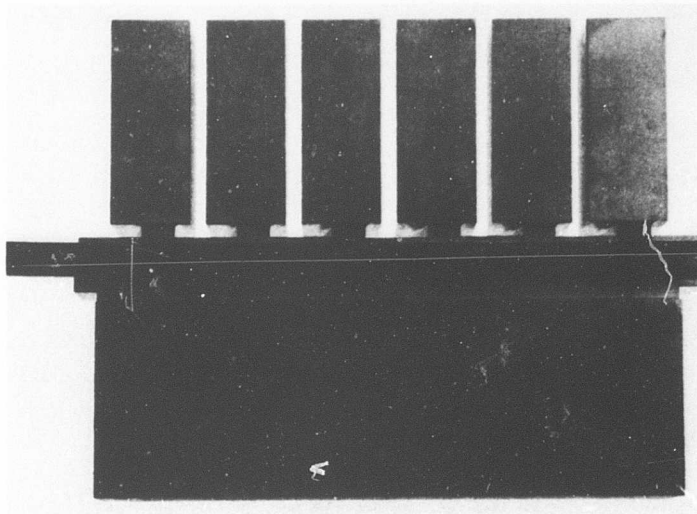Final Specimens Clamped in
Welding Jig.

134

Figure 81. Electron-Beam-Welded Final Specimen
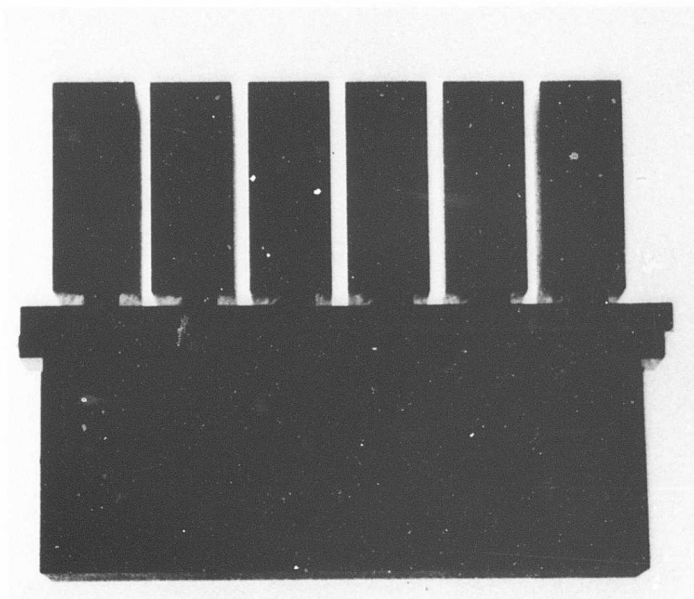With Backup Strip in Place.

Figure 82. Front View of an Electron-Beam-
Welded Final Specimen With Weld
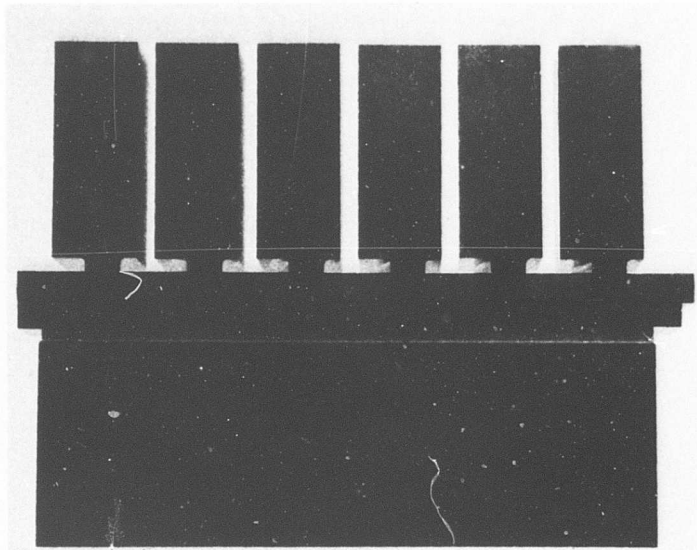Backup Strip Removed.

135

Figure 83. Back View of an Electron-Beam-Welded
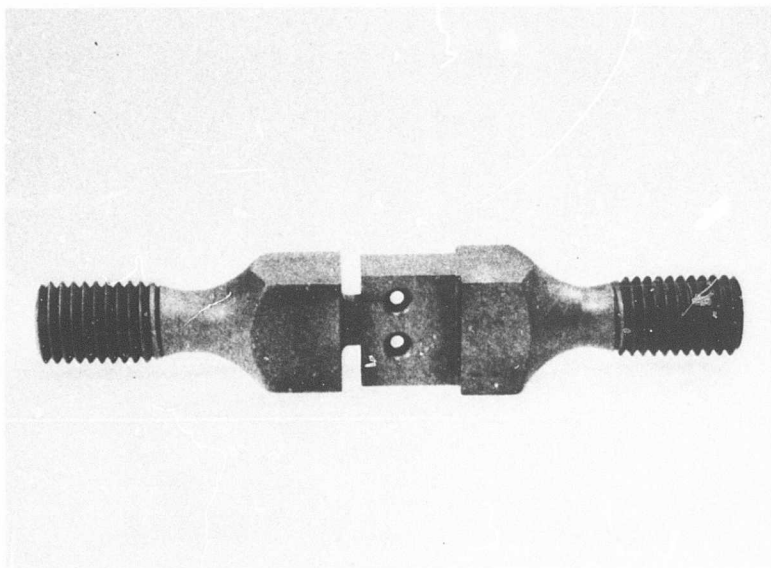Final Specimen With Weld Backup
Strip Removed.

Figure 84. Electron-Beam-Welded Final Specimen
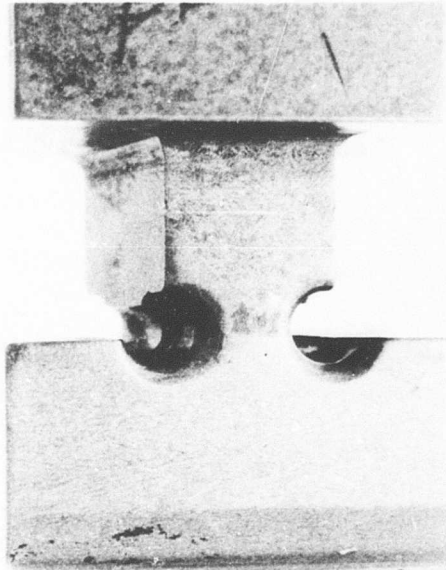After Completion of Final Machining.

Figure 85.   Front View of Joint-Test Section
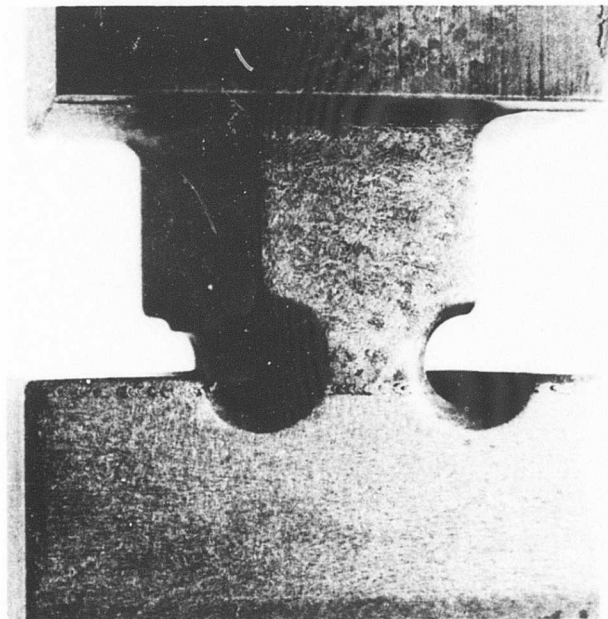of an Electron-Beam-Welded Final
Specimen.

Figure 86.   Back View of Joint-Test Section
of an Electron-Beam-Welded Final
Specimen.

137

5.3   INSPECTION OF FINAL SPECIMENS

All three types of the final specimens were macroscopically
examined 'for defects prior to testing to determine the effec-
tiveness of inspection procedures. In addition, selected
specimens of each type were sectioned and inspected micro-
scopically. Subsequent subparagraphs present the inspection
results for the diffusion-bonded, brazed, and electron-beam-
welded specimens, respectively.

5.3.1   Diffusion-Bonded Specimens

The diffusion-bonded specimens could not be readily inspected
for quality of the bond. The best control check was found to
be a micrometer measurement of the width of the two Inconel
718 portions of the specimen transverse to the direction of
loading and in the bonded region. In this area, on a specimen
subjected to the proper bonding conditions, the Inconel 718
material yielded in compression and bulged to give a maximum
measurable width of from 0.005 to 0.010 inch greater than the
prebonded width. Both of the Inconel 718 pieces were measured
on each specimen, and the specimen was rejected if the defor-
mation was not within the required limits on each side.

Metallographic examination of typical joints indicated two
possible bond conditions, as shown in Figures 87 and 88. A
good bond is shown in Figure 87, as evidenced by apparent
complete diffusion of the nickel interface material and a bond
line showing essentially no defects such as voids or inclu-
sions. Figure 88 shows a less desirable bond condition; the
bond line is somewhat discontinuous due to small voids. It
was not possible to nondestructively inspect the joint to
evaluate the bond quality, and it was also found that a single
bond might, at various points, show both acceptable and non-
acceptable bond conditions.

5.3.2   Brazed Specimens

Brazed specimens were examined visually for braze flow, and
selected specimens were sectioned for metallographic examina-
tion. A typical brazed joint is shown in Figure 89. The
specimens examined metallographically indicated the brazed
joints to be of uniform and consistent quality.
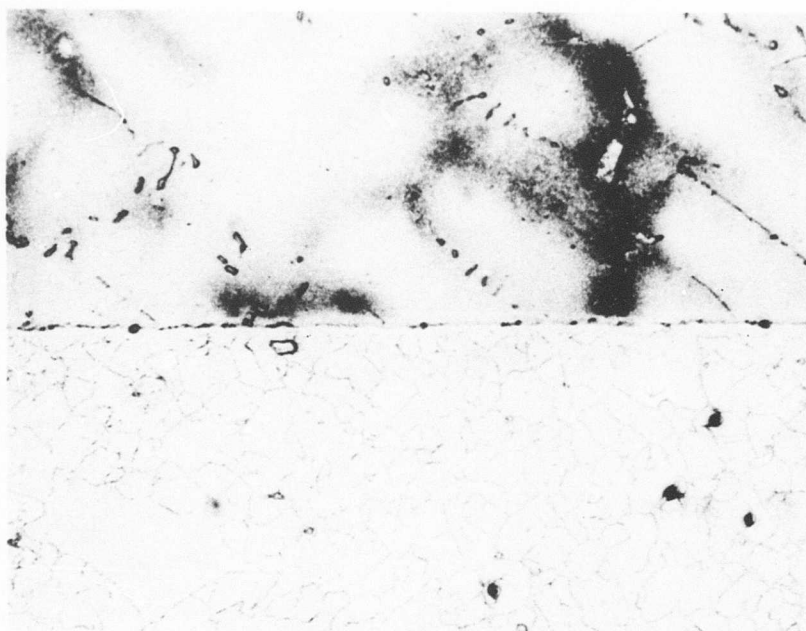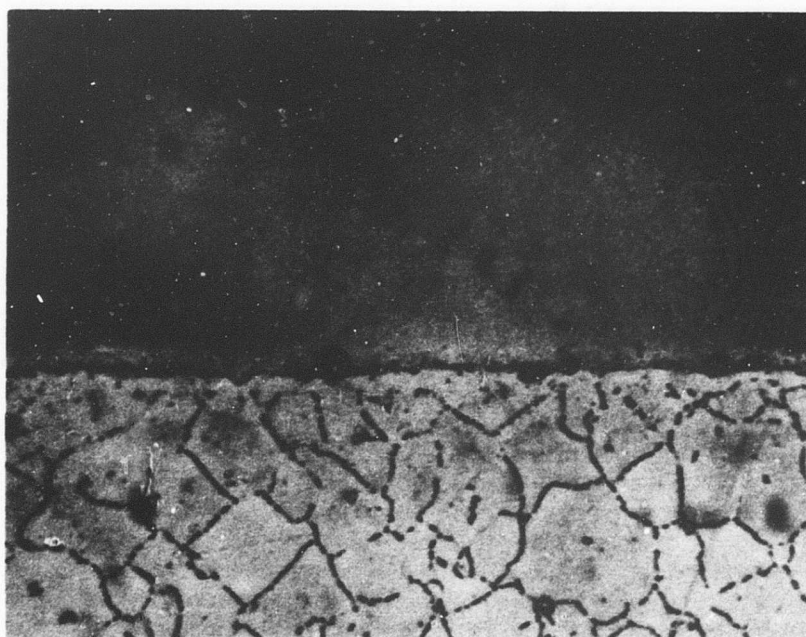
138
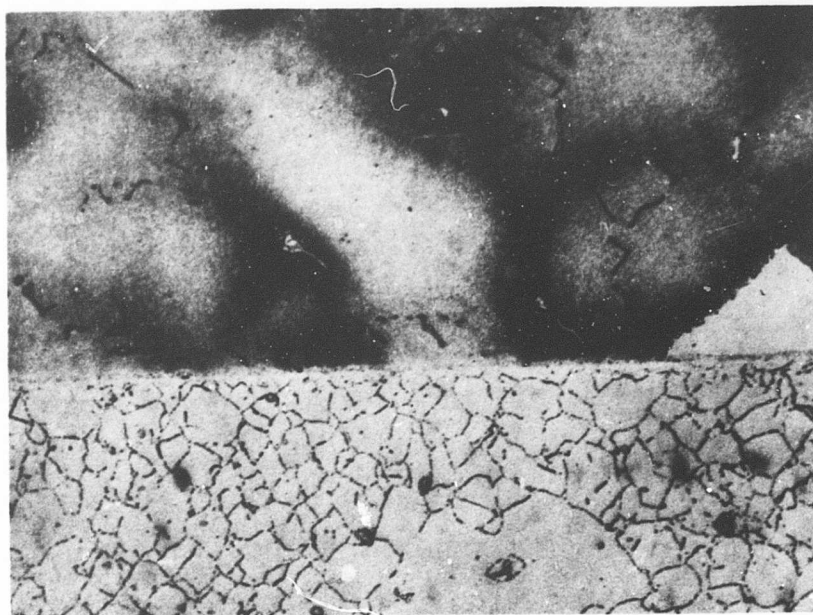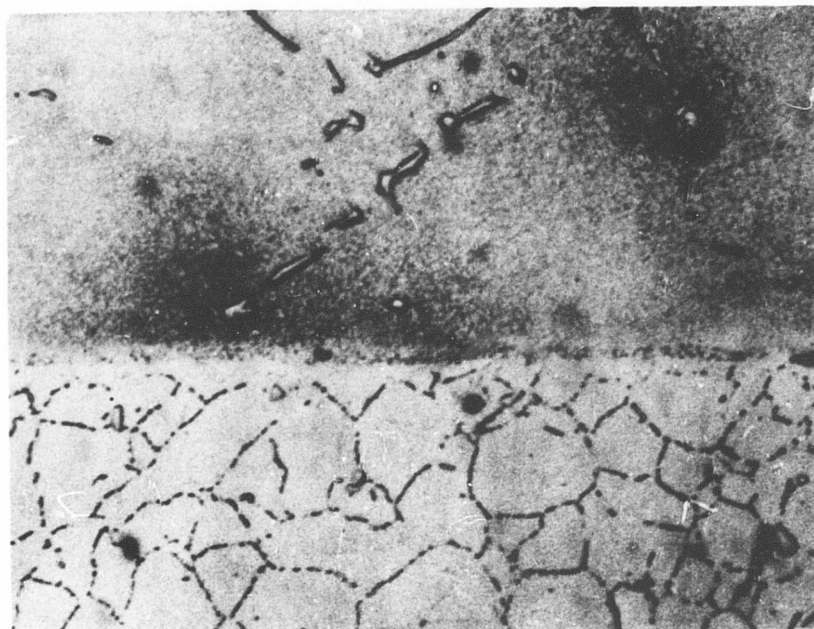
X200

X500

Figure 87. Photomicrographs of a Typical
Bonded Joint of a Diffusion-Bonded
Final Specimen Showing No Defects.

139

X200

X500

Figure 88. Photomicrographs of a Typical Bonded
Joint of a Diffusion-Bonded Final
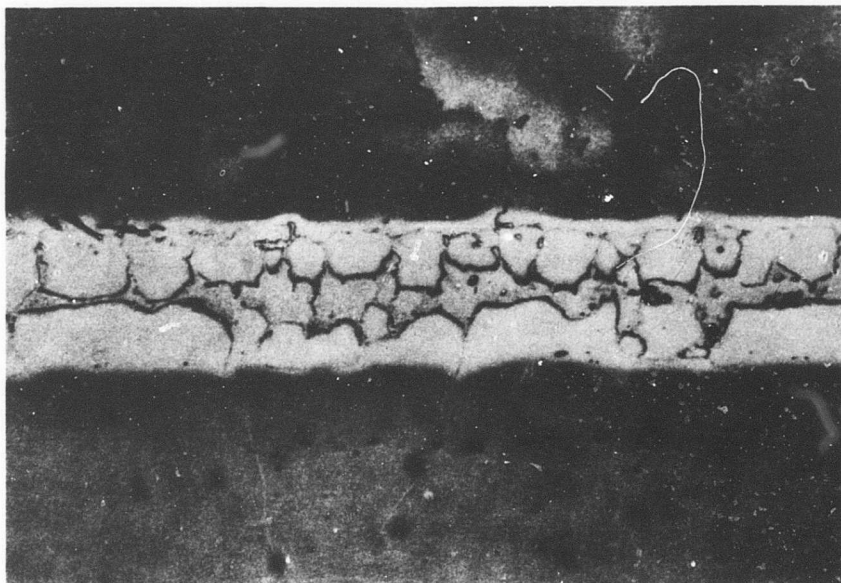Specimen Showing Defects.

140

Figure 89. Photomicrograph of a Typical
Joint of a Brazed Final Specimen
(X200).

5.3.3 Electron-Beam-Welded Specimens

Each of the electron-beam-welded specimens was inspected by
the use of dye-penetrant methods, and selected specimens were
sectioned for metallographic examination. All specimens were
found to have at least minor indications in the region of the
rivet holes when examined by penetrant techniques. Examples
of the indications and of the discontinuities producing them
are shown in Figure 90.

Figure 91 is a photomicrograph of a typical weld spike produced
in the final specimens. Cracking at the interface of the weld
zone and the MAR-M 246 material, as shown in Figure 92, was
expected. This type of cracking, although now minimized by ad-
justing welding parameters, was present in the large size
electron-beam-welded specimens of the preliminary test evalua-
tion described in Section 4.2.3. The most severe cracking
found in the final specimens is shown in Figure 93.

141
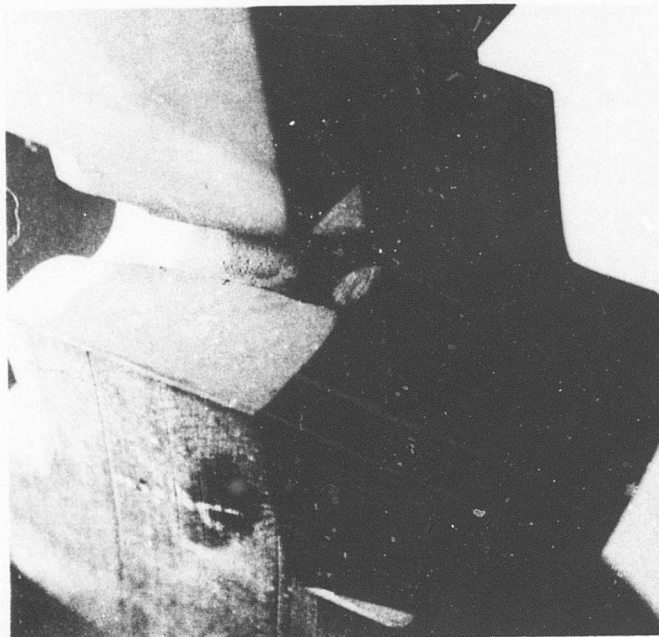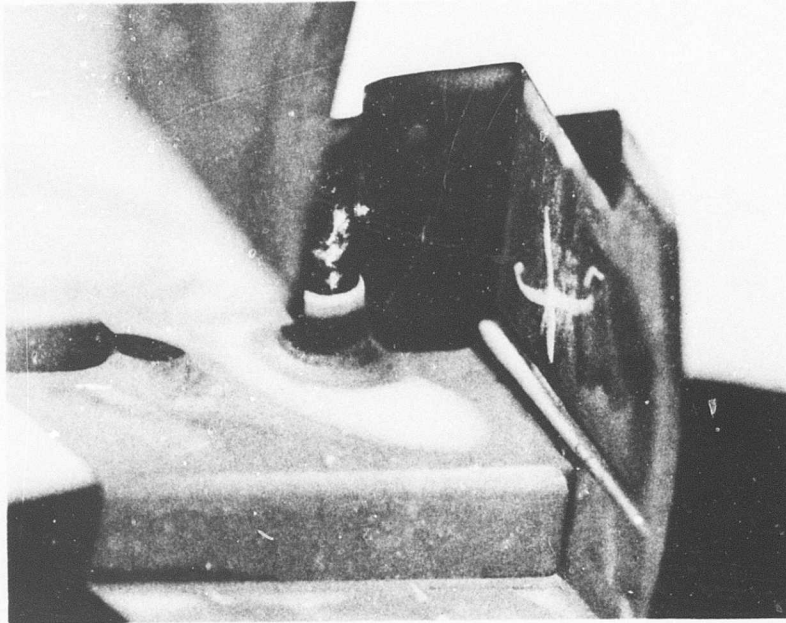
Figure 90.   Example of Indications Revealed by
             Dye-Penetrant Inspection of an
             Electron-Beam-Welded Final Specimen.

142
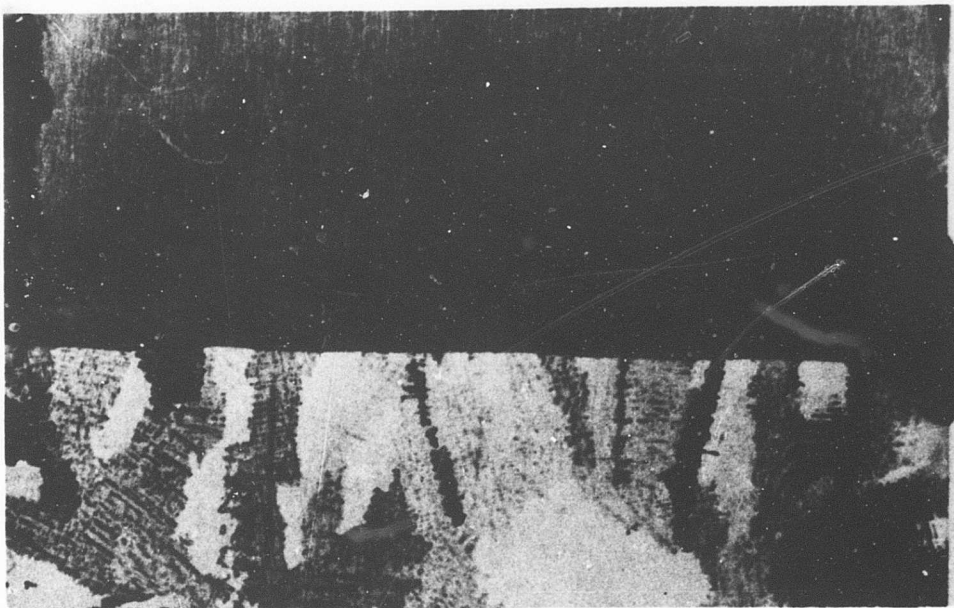
Figure 91.   Typical Weld Spike Produced in an
             Electron-Beam-Welded Final Specimen
             (Depth Penetration 0.790 Inch).

Figure 92.   Typical Cracking at the Weld Zone
             Interface of an Electron-Beam-Welded
             Final Specimen.

143
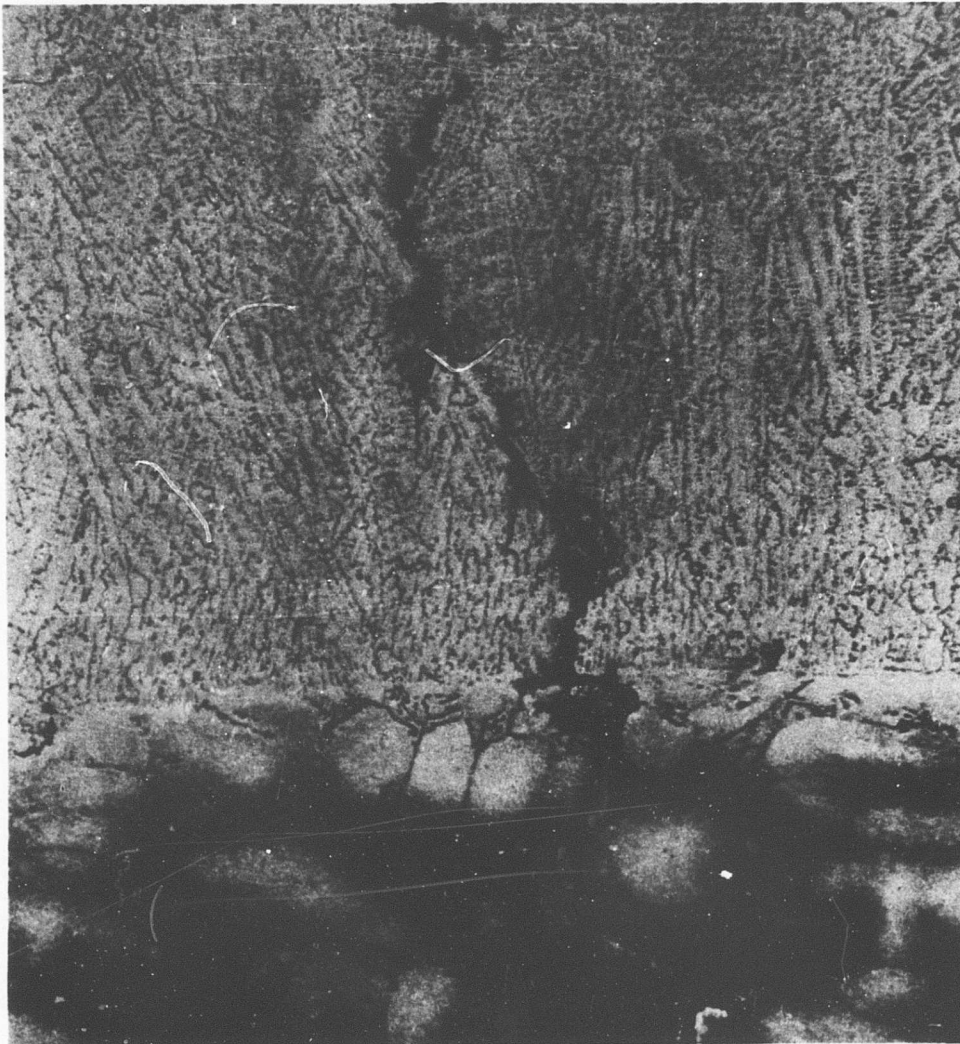
Figure 93. Photomicrograph of the Most Severe
Cracking Found in an Electron-Beam-
Welded Final Specimen (X100).

5.4 FINAL SPECIMEN TESTING

The final specimens were subjected to a test program that com-
prised tensile, stress-rupture, and low-cycle fatigue type
testing at 1200°F. A description of the test procedures and a
comparison of the acquired test data from the diffusion-
bonded, brazed, and electron-beam-welded test specimens are
presented for each type of testing in subsequent subparagraphs.

5.4.1 Tensile Testing

All tensile tests were performed in air at 1200°F by use of
conventional test techniques. Specimens were brought to tem-
perature and allowed to soak for 20 minutes prior to testing.
Load was applied at a rate of 0.04 inch per minute.

Test results for the three types of final specimens are shown
in Table XXI. The data indicate that the strength developed
per unit of joint area is greatest for the electron-beam-
welded joint and least for the diffusion-bonded joint. Total
load capability was essentially equivalent for the brazed and
the electron-beam-welded joints and was poorest for the
diffusion-bonded joints. Both the diffusion-bonded and the
brazed joints failed by shearing at the joining surfaces, as
shown in Figures 94 and 95, respectively.

The electron-beam-welded specimens failed in the MAR-M 246
material adjacent to the weld zone. Figure 96 shows two
typical failed electron-beam-welded specimens, and Figure 97
shows two types of fracture surfaces observed and also shows
the location of the simulated cooling-air passages.

| TABLE XXI. TENSILE TEST RESULTS				
Joining Technique	Specimen No.	Test Temp. (°F)	Ultimate Load (lb)	Ultimate Stress (psi)
Diffusion bonding	2	1200	8350	22,100
Diffusion bonding	6	1200	5680	15,800
Diffusion bonding	9	1200	5550	15,200
Diffusion bonding	11	1200	6900	19,100
Brazing	1	1200	18,475	44,600
Brazing	2	1200	16,200	39,000
Brazing	11	1200	17,150	41,300
Brazing	20	1200	14,875	35,800
Electron-beam welding	2-3	1200	17,300	105,000
Electron-beam welding	3-3	1200	16,100	97,800
Electron-beam welding	3-4	1200	19,750	119,500
Electron-beam welding	4-6	1200	18,050	109,400
Electron-beam welding	5-5	1200	15,200	92,300
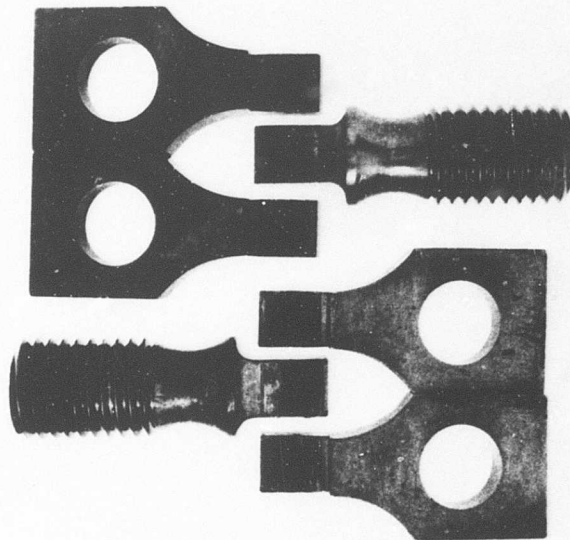
Figure 94. Tensile Failure of a Diffusion-
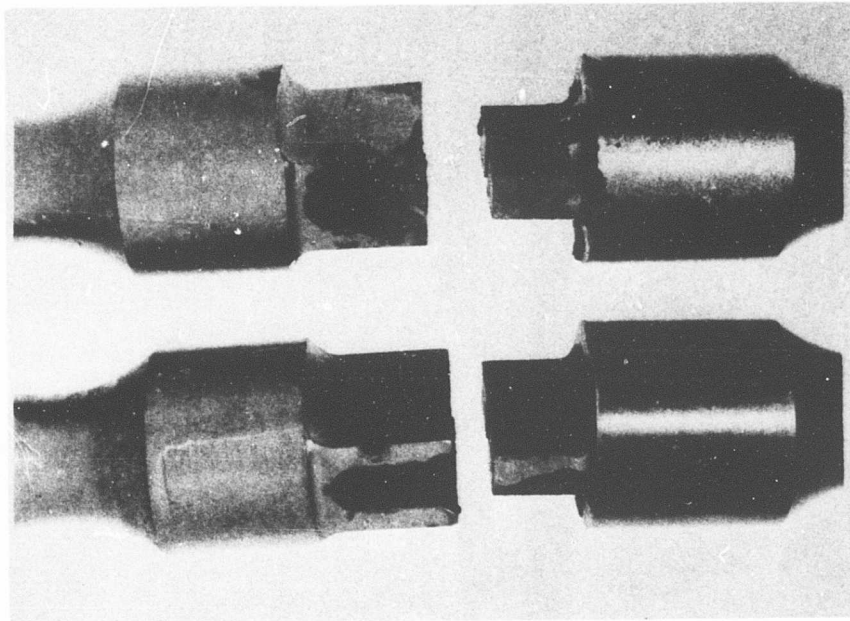Bonded Final Specimen.

Figure 95. Tensile Failure of a Brazed
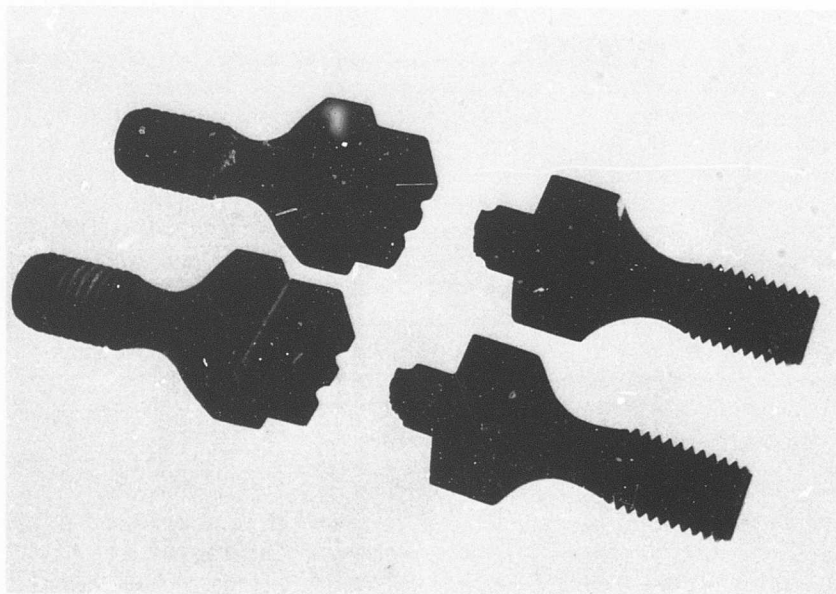Final Specimen.

147

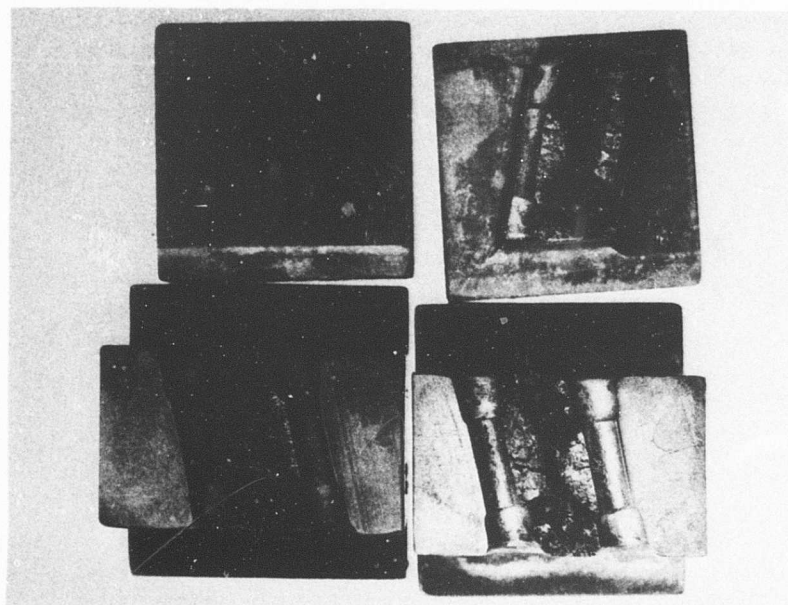Figure 96. Tensile Failure of Electron-Beam-
Welded Final Specimen.

Figure 97. Fracture Surfaces of Two Electron-
Beam-Welded Final Specimens Showing
Variation of Fracture Appearance
in Tensile Failure.

148

5.4.2 Stress-Rupture Testing

Stress-rupture testing was performed at 1200°F by use of conventional test techniques. Test results are tabulated in Table XXII and shown graphically in Figures 98 and 99. Figure 98 indicates that the stress-rupture strength per unit of joint area is greatest for the electron-beam-welded specimens and least for the diffusion-bonded specimens. Table XXII, however, shows the greatest inconsistency in test data to be in the electron-beam-welded data, which indicates some lack of reproducibility. The same data are plotted in Figure 99 on the basis of specimen load rather than stress. The data of Figure 99 illustrates that, for the specific specimen designs used, the welded and the brazed specimens were very nearly equivalent in their load-carrying capacity and were superior to the diffusion-bonded specimens.

Failure modes for the diffusion-bonded and the brazed specimens were identical with those observed in the tensile test specimens of Section 5.4.1. The diffusion-bonded specimens failed by shearing at the bond interface and the brazed specimens by shearing through the brazed material.

The electron-beam-welded specimens, however, showed a fracture mode differing from that observed either in the tensile or fatigue testing. Figure 100 shows an example of the typical fracture surfaces resulting from stress-rupture failures. Portions of the fracture face had a smooth appearance, with the smooth region corresponding to the Waspaloy/weld zone interface, as shown in Figure 101. This type of fracture occurred on all stress-rupture electron-beam-welded specimens regardless of the welded block from which they were machined. This indicates that the fracture was a general characteristic of the welded specimens and of the testing mode rather than of individual specimen differences.

At the test temperature of 1200°F, the MAR-M 246 material had a greater stress-rupture strength than the Waspaloy material, thus tending to force failure to occur in the Waspaloy. As a result, the actual failure appears to have originated in the heat-affected zone of the Waspaloy. The fracture followed the interface between the Waspaloy and the weld zone until it intercepted transverse cracks through the weld, after which it progressed across the weld and into the MAR-M 246 material where fracture was completed. In addition, transverse cracks terminating at the Waspaloy interface could contribute to crack initiation. This analysis indicates that the limiting factors in utilization of the electron-beam welding technique are (a) the stress-rupture strength which can be achieved in the heat-affected zone of the Waspaloy and (b) the extent that the weld cracking can be minimized.

149

TABLE XXII. STRESS-RUPTURE TEST RESULTS					
Joining Technique	Specimen No.	Test Temp. (°F)	Load (lb)	Stress (psi)	Life (hr)
Diffusion bonding	19	1200	2500	6900	422.4+
Diffusion bonding	13	1200	3000	8300	23.0
Diffusion bonding	14	1200	3000	8300	*
Diffusion bonding	15	1200	3000	8300	*
Diffusion bonding	18	1200	3440	9500	133.0
Diffusion bonding	16	1200	4000	11,000	2.6
Brazing	6	1200	8100	15,600	400.0+
Brazing	12	1200	8240	19,900	92.6
Brazing	8	1200	7920	20,200	283.0
Brazing	19	1200	9400	22,200	91.0
Brazing	5	1200	10,300	24,800	22.3
Brazing	9	1200	11,400	27,500	14.0
Brazing	10	1200	11,400	27,500	*
Electron-beam welding	3-6	1200	13,000	78,900	18.1
Electron-beam welding	4-4	1200	13,000	78,900	900.0+
Electron-beam welding	2-6	1200	15,000	91,000	278.3
Electron-beam welding	4-3	1200	16,000	97,000	1.1
Electron-beam welding	5-4	1200	16,000	97,000	2.1**
Electron-beam welding	5-3	1200	17,000	101,500	*

*Broke on loading.
**Failed in MAR-M 246 material away from test section.
+Test discontinued---no failure.
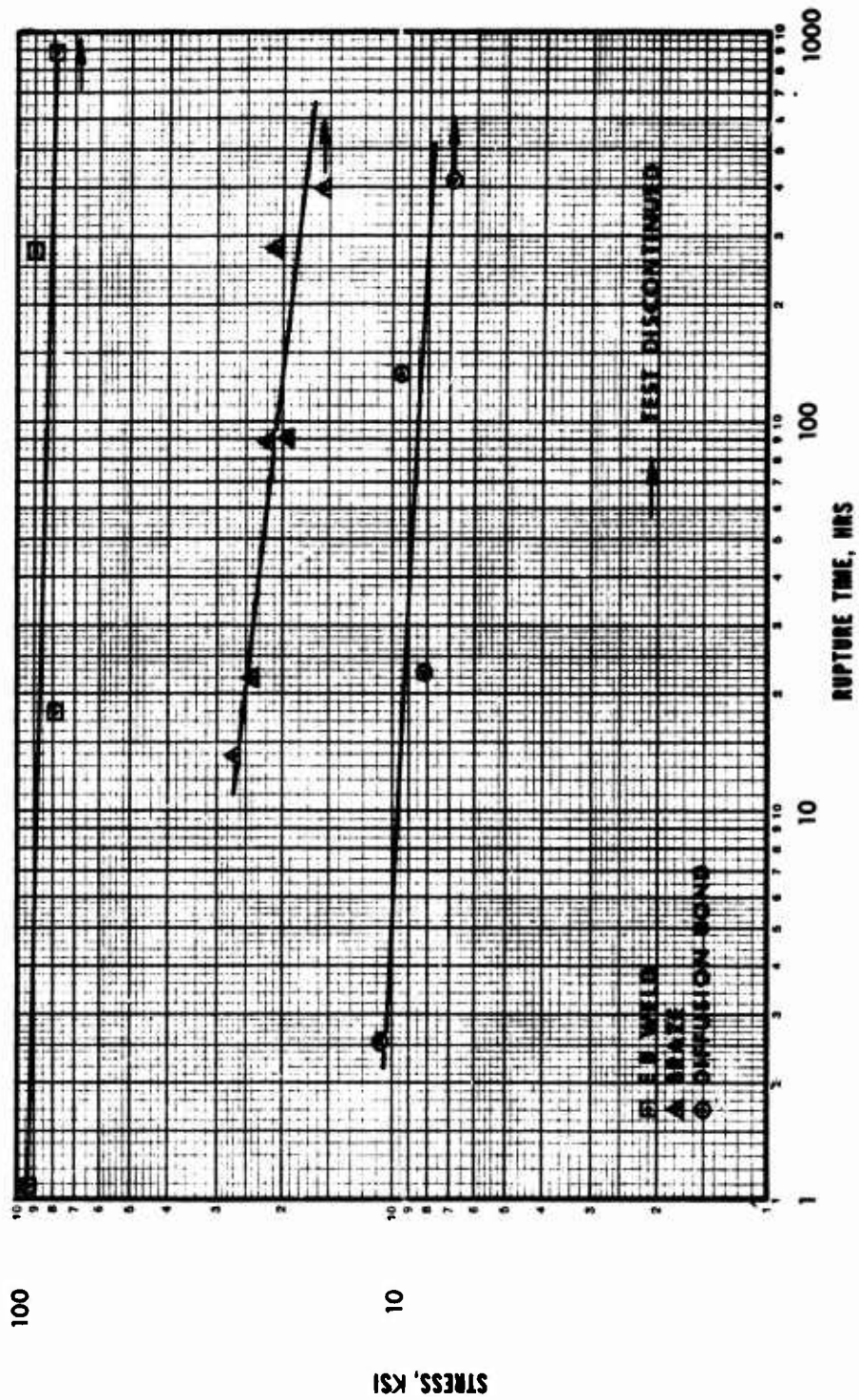
Figure 98. Stress-Rupture Data Plotted as Stress Versus Rupture Time.
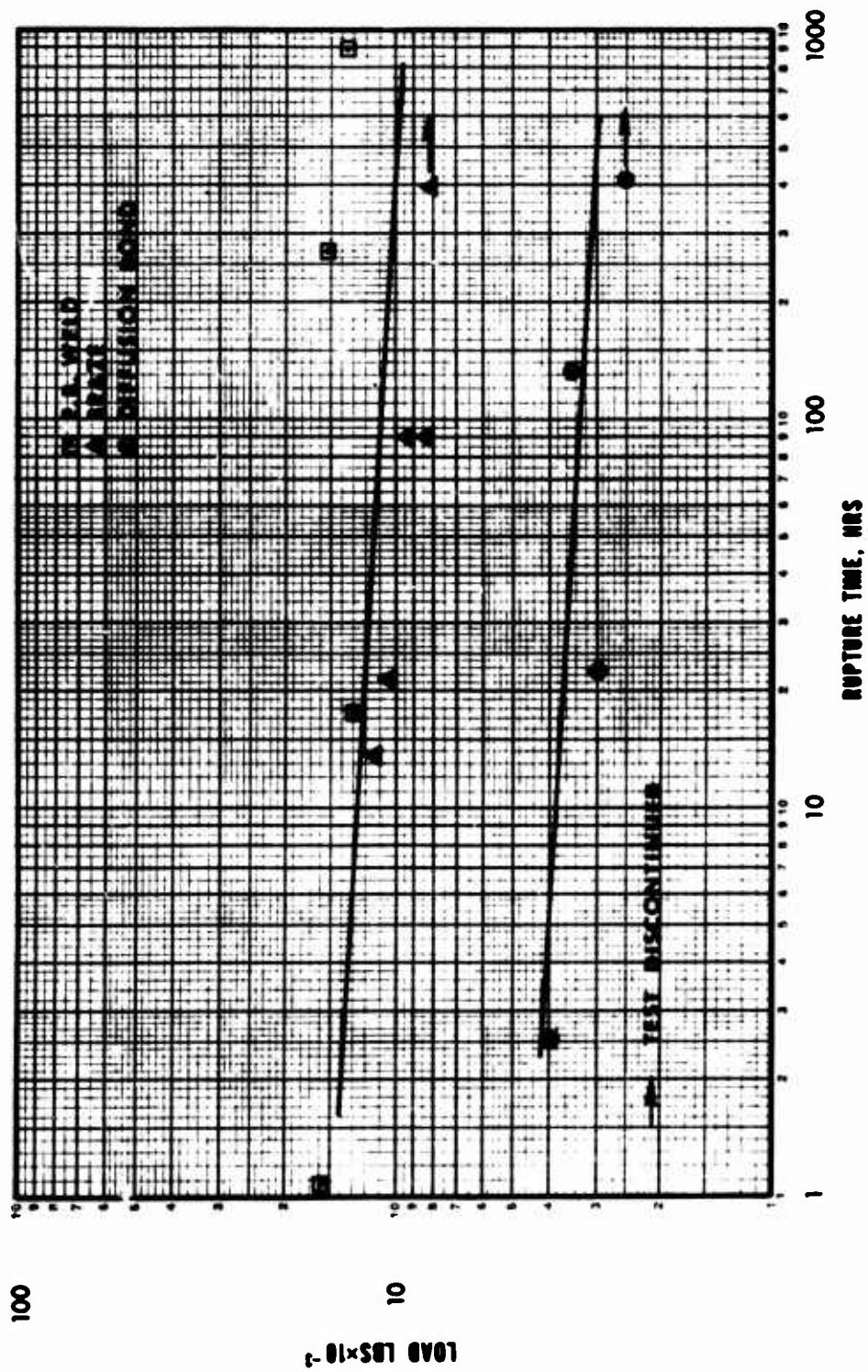
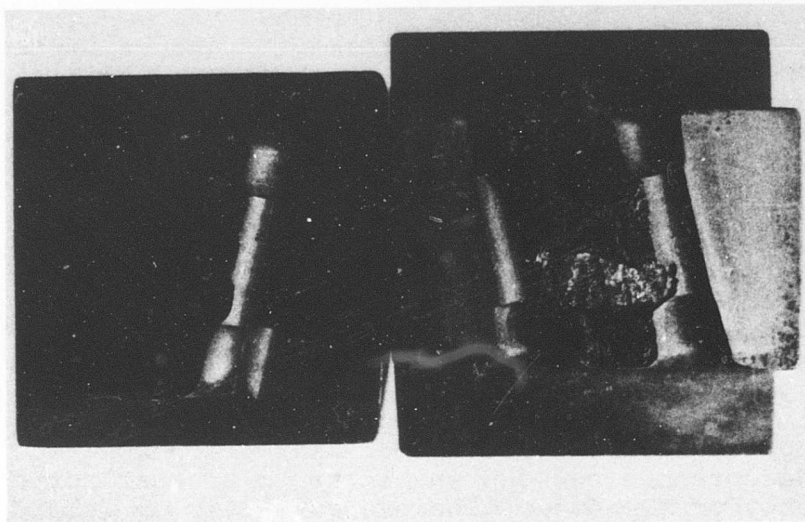Figure 99. Stress-Rupture Data Plotted as Load Versus Rupture Time.

152

Figure 100. Typical Example of Fracture Surfaces
Resulting From Stress Rupture Failure
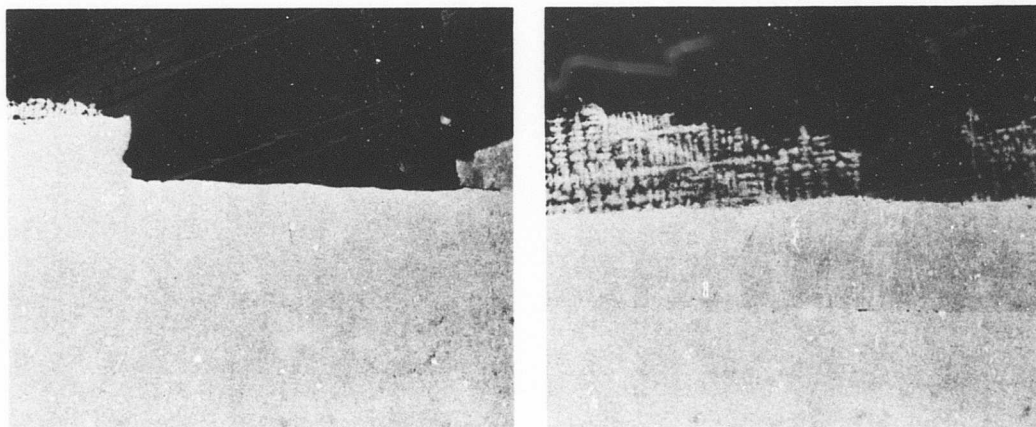of Electron-Beam-Welded Final
Specimen.

Figure 101. Stress-Rupture Failure of Electron-
Beam-Welded Final Specimen Showing
Smooth Fracture Face Corresponding
to Waspaloy/Weld Zone Interface (X15).

153

5.4.3 Low-Cycle Fatigue Testing

Low-cycle fatigue testing was performed at 1200°F by the use of a closed-loop electrohydraulic test system. All loading was in tension with cycling from zero stress to the maximum stress desired and back to zero at a rate of 1000 cycles per minute.

Test data are shown in Table XXIII and are plotted in Figure 102. The best fatigue strength was shown by the electron-beam-welded specimens and the poorest by the diffusion-bonded specimens. Figure 102 shows the poor correlation of the diffusion-bonded specimens, which indicates a possible lack of reproducibility in bonding.

Failure in the diffusion-bonded specimens occurred by shearing at the bonded interface. Post-test inspection revealed no apparent differences between specimens to account for the inconsistency of the data. The brazed specimens failed, as shown in Figure 103, by fracture across either one or both of the MAR-M 246 alloy portions of the specimen. When failure occurred across only one portion, the other joining surface sheared through the braze.

In the electron-beam-welded specimens, failure occurred in the MAR-M 246 material adjacent to the weld zone. As in the case of the electron-beam-welded specimens that failed in tension, two types of fracture surfaces were observed. Figure 104 shows a relatively smooth failure as opposed to a more coarse fracture surface. No correlation could be made as to the relative strengths of specimens displaying the different fracture appearances.

154

TABLE XXIII.	FATIGUE TEST DATA				
Joining Technique	Specimen No.	Test Temp (°F)	Maximum Load (lb)	Maximum Stress (psi)	Cycles to Failure
Diffusion bonding	3	1200	4000	11,100	10,000+
Diffusion bonding	4	1200	5000	13,800	23,400
Diffusion bonding	20	1200	5250	14,500	3
Diffusion bonding	12	1200	5500	15,200	24
Diffusion bonding	5	1200	6000	16,600	107
Diffusion bonding	10	1200	6000	16,600	123
Brazing	4	1200	7500	18,000	6750
Brazing	18	1200	8000	19,200	10,400
Brazing	3	1200	8500	20,500	5265
Brazing	7	1200	9000	21,600	5175
Brazing	14	1200	10,000	24,200	3200
Brazing	13	1200	12,000	28,900	2630
Brazing	15	1200	12,500	30,200	1410
Electron-beam welding	3-2	1200	9000	54,500	36,400
Electron-beam welding	4-2	1200	9500	57,500	13,450
Electron-beam welding	2-4	1200	10,000	61,000	4600
Electron-beam welding	4-5	1200	10,500	63,800	3250
Electron-beam welding	3-5	1200	11,000	66,800	15,570
Electron-beam welding	2-5	1200	12,000	73,000	1350

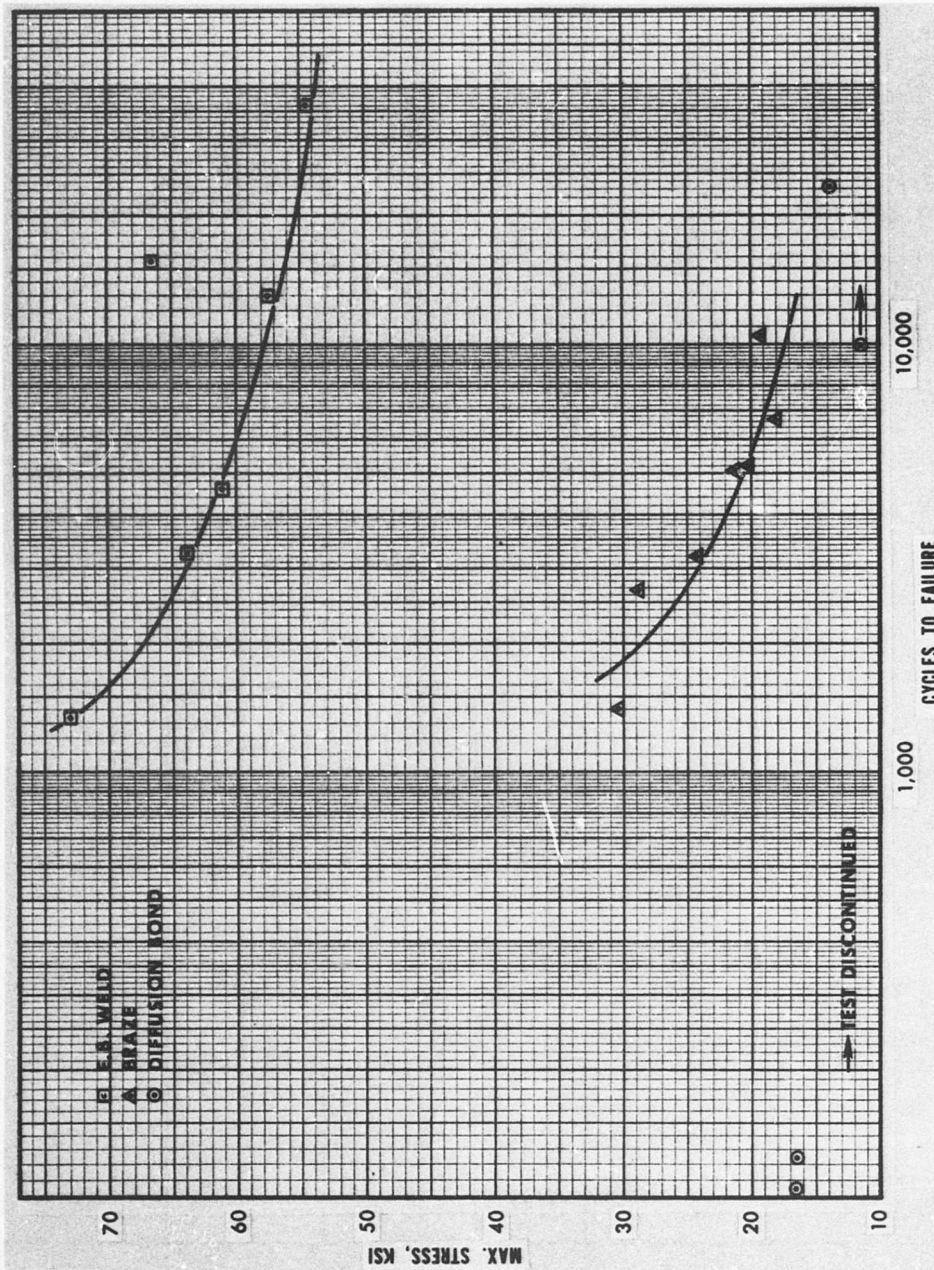+Test discontinued--no failure.

Figure 102. Low-Cycle Fatigue Failure Data for Three Types of Final Specimens.
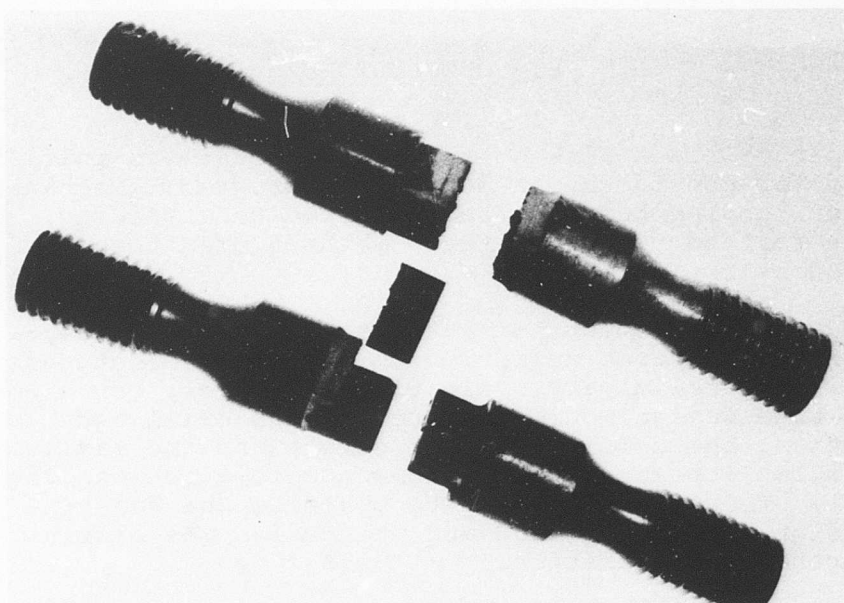
156

Figure 103. Two Modes of Low-Cycle Fatigue
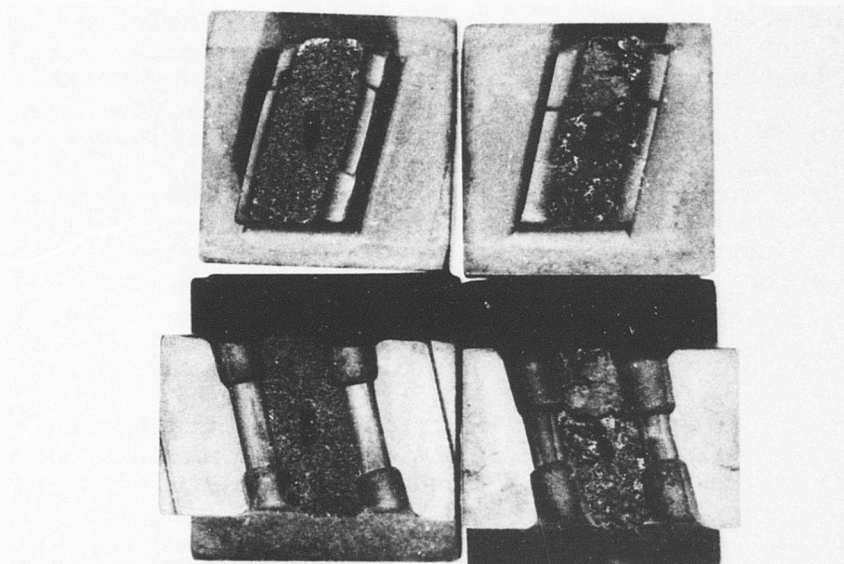Failure of Brazed Final Specimens.

Figure 104. Low-Cycle Fatigue Failure of Electron-
Beam-Welded Final Specimen--Smooth
Fracture Surface is Shown on Left and
Coarse Fracture Surface is Shown on
Right.

6. CONCLUSIONS

Four types of blade/disk attachment methods were initially
selected for consideration during the program: Mechanical,
diffusion bonding, brazing, and electron-beam welding. Con-
clusions reached regarding these methods of attachment are
presented below.

Several mechanical means of attachment were examined, and the
conventional fir-tree attachment method was selected for con-
sideration. Preliminary evaluations, however, revealed that
the fir-tree design would require a large axial width disk.
In addition, the combined fillet stress and the maximum com-
bined fillet stress of the attachment elements made the design
marginal. Therefore, efforts to optimize the fir-tree attach-
ment design were terminated and the design was eliminated
from further consideration.

Development and evaluation of the diffusion-bonding attachment
method were pursued throughout the program. Materials used
in the diffusion-bonded final test specimens were MAR-M 246
to simulate the blade pedestal element and Inconel 718 to
simulate the disk. Although the diffusion-bonding attachment
method offered certain advantages, it was concluded from re-
sults of the final specimen low-cycle fatigue and stress-
rupture testing that this method of blade/disk attachment is
inadequate. A design shear stress level of 35,000 psi ap-
peared to be achievable on the basis of preliminary tests, but
the low-cycle fatigue and stress-rupture test results indicate
that only a much lower strength level could be expected. Al-
though some probabilities exist that the 16-rms surface finish
of the diffusion-bonded final specimens (selected out of
consideration to the economical feasibility of the design)
contributed to the reduced joint-strength properties, the
low strength level of the diffusion-bonded joint and the
relatively heavy disk make this approach unattractive.

Development and evaluation of the brazing attachment method
were also pursued throughout the program. Materials used in
the brazed final test specimens were MAR-M 246 to simulate
the blade pedestal element and Waspaloy to simulate the disk.
It was concluded from results of the final specimen low-cycle
fatigue and stress-rupture tests that this joining method is
eligible for consideration as a candidate for rotational test
evaluation. Although the final tests did not reveal any
dramatic improvements over the preliminary test values, the
results did show that the design shear stress level of 17,500
psi is not unrealistic for the larger bonding area. At this
stress, the Larson-Miller parameter (with use of a constant

158

of 20) would be approximately 37.5. At the maximum joint temperature of 1200°F, the corresponding rupture life would be 400 hours.

While the design goal of 1000 hours was not met, a reduction in stress level from 17,500 psi to approximately 15,000 psi would meet the design-life objective. Low-cycle fatigue life would also be satisfied, since the assumption of one start per hour (1000 starts total) could be met by a stress as high as 20,000 psi. This design concept may be modified to provide a lower shear stress in the joint by extending the joint surfaces radially inward. However, modifications of this type would add to the load carried by the disk and would further increase the axial disk dimensions. It is believed that development of a stronger brazing alloy would produce greater improvement in this design concept than geometric modifications would achieve.

Development and evaluation of the electron-beam-welding attachment method were pursued throughout the program. Materials used in the electron-beam-welded final test specimens were MAR-M 246 to simulate the blade pedestal element and Waspaloy to simulate the disk. It was concluded from results of the final specimen low-cycle fatigue and stress-rupture tests that this joining method produced a joint strength that exceeded design requirements. However, elimination of the weld joint microcracking would be necessary before this joining method could be considered for rotational test evaluation. It is possible that the stress required to propagate the cracks would be above the applied stress in a practical design; however, further testing would be required for verification. It is concluded that the design stress level in the joint of this attachment method is sufficiently below the average failure stress at 1000 hours to indicate feasibility of the design.

As a secondary effort to the blade/disk attachment activities, a preliminary evaluation was made to study the feasibility of developing a strut-supported sheet metal blade (shell/strut attachment). Joining methods that were examined included diffusion bonding, brazing, and cast bonding. Conclusions reached during the preliminary evaluation are presented below.

The diffusion-bonding concept of joining was shown to be a feasible method for consideration in shell/strut attachment. The degree of success that might be achieved by using this process would depend strongly upon the development of a bonding procedure, such as gas-pressure bonding, that would allow application of an isostatic load over the blade surface to be bonded.

159

The brazing concept of joining was not shown to be a desirable method for consideration in shell/strut attachment. The relatively low stress-rupture life of the existing braze alloys corresponding to the operating temperatures of the shell/strut joint make this method of joining unattractive for development considerations.

The cast-bonding concept was shown to be a feasible method for consideration in the development of a strut-supported sheet metal blade. By this method, the strut and shell/strut bonding are formed in one operation. Use of preplaced wires or cores that can be subsequently removed chemically to form cooling-air passages was shown to be a reasonable approach to pursue. Additional development would be required before this method could be used to produce scale-size specimens.

7. RECOMMENDATIONS

It is recommended that additional development and test efforts
be considered for both the brazing and electron-beam-welding
methods of blade/disk attachment.

For the brazing process, rotational testing of full-scale
rotors is recommended to substantiate the joint strength ob-
tained in the final specimen testing. Ultimate tensile
strength can best be determined by rotor-overspeed destruc-
tive testing in a whirlpit. The low-cycle fatigue strength
can be determined by rotor cyclic testing in a whirlpit.
Determination of the joint-stress-rupture life can best be
obtained by sectioning the rotor and subjecting the specimens
to testing in a conventional creep-test machine.

For the electron-beam-welding process, research efforts to
eliminate the weld joint microcracking are recommended. It is
believed that this refinement would result in a substantial
improvement in attachment reliability, particularly with
respect to stress-rupture strength. Also, additional stress-
rupture testing at reduced stress levels is recommended. If
results from the additional testing revealed an improvement
in the consistency of joint strength data, then full-scale
rotors should be fabricated and evaluated by rotational test-
ing as described in the preceding paragraph.

LITERATURE CITED

1. Stewart, Warner L., Whitney, Warren J., and Wong, Robert Y., A STUDY OF BOUNDARY LAYER CHARACTERISTICS OF TURBO-MACHINE BLADE ROWS AND THEIR RELATION TO OVERALL BLADE LOSS, ASME Trans., J. of Basic Engr., Paper No. 59-A-23, 1959.

2. Stewart, Warner L., Glassman, Arthur J., and Vanco, Michael R., EXAMINATION OF AXIAL-FLOW TURBINE BLADE-LOADING CHARACTERISTICS USING DIFFUSION PARAMETERS, ASME PAPER 67-WA/GT-8, March 1967.

3. Zweifel, O., THE SPACING OF TURBOMACHINE BLADING, ESPECIALLY WITH LARGE ANGULAR DEFLECTION, The Brown Boveri Review, Vol. 436, Decimal Index 621-226.2, December 1945.

4. Whitney, Warren J., Stewart, Warner L., and Miser, J.W., EXPERIMENTAL INVESTIGATION OF TURBINE-STATOR-BLADE OUTLET BOUNDARY LAYER CHARACTERISTICS AND COMPARISON WITH THEORETICAL RESULTS, NACA RM E55K24, Washington, D.C., March 1956.

5. Monson, S.S., DIRECT METHOD OF DESIGN AND STRESS ANALYSIS OF ROTATING DISKS WITH TEMPERATURE GRADIENT, NACA Report 952, Washington, D.C., 1950.

APPENDIX
LITERATURE SURVEY

A survey was made of Government agencies and technical
literature to review existing blade/disk attachment methods
and to evaluate current technology apropos to: (a) material
types and property strength of superalloys, (b) rotor fabri-
cation technology, (c) mechanical attachment methods, and
(d) material joining processes, including welding techniques,
brazing, and diffusion bonding. The survey was conducted in
parallel with the aerothermodynamic design activity.

Recent activities devoted specifically to blade attachment
problems were found to be primarily concerned with space
power applications. The inherent design differences of the
space power components from the subject turbine are such that
most of the technology evaluated was not useful to the blade/
disk problems encountered in this program.

A considerable amount of technical literature was found that
described fabrication techniques, various joining processes,
and methods of joint strength testing. This information was
useful in the mechanical design, fabrication, and test
activities of this program.

Some of the more pertinent publications directly applicable
to the diffusion-bonding, brazing, and electron-beam-welding
attachment methods that were evaluated during this program
are listed by category on the following pages.

DIFFUSION BONDING

Kaarlela W. T., and Margolis, W. S., ALLOY EFFECTS IN THE LOW
PRESSURE DIFFUSION BONDING OF SUPERALLOYS, General Dynamics
Corporation, Fort Worth, Texas; Welding Journal 48th, Detroit,
Michigan, April 1967, Supplement Vol. 46, June 1967, pp 282-
288.

King, J. P. Jr., Roberlotto, R. B., and Dillingham, A. C. Jr.,
DIFFUSION BONDING OF TITANIUM AND BERYLLIUM, North American
Rockwell Corporation; Air Force Systems Command, Wright-
Patterson Air Force Base, Ohio, Technical Report AFML-TR-67-
388, December 1967.

Cogan, R. M., DEVELOPMENT OF A MANUFACTURING PROCESS FOR FABRICATED DIFFUSION HOLLOW BLADES, Aircraft Engine Group, General Electric Company, Cincinnati, Ohio; Advanced Fabrication Techniques Branch, Manufacturing Technology Division, Air Force Materials Laboratory, Air Force Systems Command, Wright Patterson Air Force Base, Ohio, Contract AF33615-68-C-1215, Project No. IR-883-8(1), February and May 1968.

Meiners, Kenneth E., GAS-PRESSURE AND THERMONAC DIFFUSION BONDING AT BATTELLE COLUMBUS LABORATORIES, Materials Development Division, Battelle Memorial Institute, unpublished.

Crane, C. H., and Lovell, D. F., DIFFUSION WELDING OF DISSIMILAR METALS, Welding Journal, Vol. 46, No. 1, January 1967.

Obrrut, J. J., DIFFUSION WELDING--THE QUEST FOR PERFECT JOINTS, Iron Age Metalworking, Vol. 4, No. 8, August 1965.

Orrok, Neale E., APPLICATION OF DIFFUSION BONDING, Metal Progress Vol. 89, No. 6, June 1966.

BRAZING

Smeltzer, D. E., Malik, R. K., Hammer, A. N., and Compton, W. A., DEVELOPMENT OF JOINING PROCESSES FOR TITANIUM FOILS, Solar Division of International Harvester Company; Air Force Materials Laboratory, Research and Technology Division, Air Force Systems Command, Wright-Patterson Air Force Base, Ohio, Technical Report AFML-TR-67-305, Vols. I and II, September 1967.

BRAZING AND BRAZING ALLOYS, A Report Bibliography, NASA SP-5026, Washington, D. C., 1967.

Schwartz, M. M., BRAZING BREAKTHROUGH JOINS REFRACTORY HONEYCOMB, Tool Manufacturing Engineer, Vol. 58, No. 3, March 1967, pp 33-35.

King, E. J., EFFECT OF GE 8100 BRAZE ALLOY ON THE PROPERTIES OF HAYNES 25 AND INCONEL 702, Bell Aerosystem Laboratory Report BLR 63-4(M), Buffalo, N. Y., March 1963.

THE SOUNDNESS AND STRENGTH OF HIGH-TEMPERATURE VACUUM-BRAZED JOINTS, The British Non-Ferrous Metals Research Association, Report A.1249, London, England, September 1959.

HIGH-TEMPERATURE STRESS-TO-RUPTURE PROPERTIES OF BRAZED JOINTS IN HEAT-RESISTING ALLOYS, The British Non-Ferrous Metals Research Association, Report A.1250, London, England, September 1959.

BRAZE LAP JOINTS AT HIGH TEMPERATURE, A Report Bibliography, ARB NO. 067955, Arlington, Virginia, 1967.

ELECTRON-BEAM WELDING

Beer, R., FABRICATION OF LIGHTWEIGHT TURBINE COMPONENTS USING ELECTRON BEAM WELDING FOR THE ATTACHMENT OF SHEET METAL BLADES TO DISKS AND SHROUDS, Aerojet-General Corporation, Sacramento, California, Report No. NASA CR-54814, AGC8800-49, Contract No. NAS3-2555, Washington, D. C., October 1966.

Lubin, Barry T., A CORRELATION OF ELECTRON BEAM WELDING PARAMETERS, Dynatech Corp., Cambridge, Massachusetts, ASME Paper 66-WA/MET-18, 1967.

Engguist, R. D., PARAMETERS AFFECTING ELECTRON BEAM WELDING, ASM Metals Park, Ohio, Tech. Report No. C7-19.2, 1967.

Miller, K. J., ELECTRON AND LASER BEAM WELDING, ASM Metals Park, Ohio, ASTME WES-54, 1967.

Wiffen, E. L., ELECTRON BEAM WELDING, Mach and Tool Blue Book, Vol. 61, December 1966, pp 109-111.

Fletcher, M. J., ELECTRON BEAM WELDING, Engl. Elect. J., Vol. 20, No. 5, September-October 1965, pp 15-20.

BRAZE LAP JOINTS AT HIGH TEMPERATURE, A Report Bibliography,
ARB NO. 067955, Arlington, Virginia, 1967.

ELECTRON-BEAM WELDING

Beer, R., FABRICATION OF LIGHTWEIGHT TURBINE COMPONENTS USING
ELECTRON BEAM WELDING FOR THE ATTACHMENT OF SHEET METAL BLADES
TO DISKS AND SHROUDS, Aerojet-General Corporation, Sacramento,
California, Report No. NASA CR-54814, AGC8800-49, Contract No.
NAS3-2555, Washington, D. C., October 1966.

Lubin, Barry T., A CORRELATION OF ELECTRON BEAM WELDING
PARAMETERS, Dynatech Corp., Cambridge, Massachusetts, ASME
Paper 66-WA/MET-18, 1967.

Engguist, R. D., PARAMETERS AFFECTING ELECTRON BEAM WELDING,
ASM Metals Park, Ohio, Tech. Report No. C7-19.2, 1967.

Miller, K. J., ELECTRON AND LASER BEAM WELDING, ASM Metals
Park, Ohio, ASTME WES-54, 1967.

Wiffen, E. L., ELECTRON BEAM WELDING, Mach and Tool Blue Book,
Vol. 61, December 1966, pp 109-111.

Fletcher, M. J., ELECTRON BEAM WELDING, Engl. Elect. J.,
Vol. 20, No. 5, September-October 1965, pp 15-20.

DOCUMENT CONTROL DATA - R & D

(Security classification of title, body of abstract and indexing annotation must be entered when the overall report is classified)

1. ORIGINATING ACTIVITY *(Corporate author)*	2a. REPORT SECURITY CLASSIFICATION
The AiResearch Manufacturing Company of Arizona, 402 S. 36 St. Phoenix, Arizona	Unclassified
	2b. GROUP

3. REPORT TITLE

AN INVESTIGATION OF TURBINE BLADE/DISK ATTACHMENT METHODS FOR SMALL, COOLED GAS TURBINES

4. DESCRIPTIVE NOTES *(Type of report and inclusive dates)*

Final Report

5. AUTHOR(S) *(First name, middle initial, last name)*

J. L. Helmbrecht, R. F. Kirby, and F. Weber

6. REPORT DATE	7a. TOTAL NO. OF PAGES	7b. NO. OF REFS
January 1970	184	5

8a. CONTRACT OR GRANT NO.	9a. ORIGINATOR'S REPORT NUMBER(S)
DAAJ02-68-C-0119	USAAVLABS Technical Report
b. PROJECT NO.	69-91
Task 1G162203D14413	
c.	9b. OTHER REPORT NO(S) *(Any other numbers that may be assigned this report)*
d.	AiResearch assigned number, PE-8031-R

10. DISTRIBUTION STATEMENT

This document is subject to special export controls, and each transmittal to foreign governments or foreign nationals may be made only with prior approval of US Army Aviation Materiel Laboratories, Fort Eustis, Virginia 23604.

11. SUPPLEMENTARY NOTES	12. SPONSORING MILITARY ACTIVITY
	US Army Aviation Materiel Laboratories Fort Eustis, Virginia

13. ABSTRACT

This report describes the analytical, experimental, and developmental efforts that were conducted to design, fabricate, test, and evaluate turbine-rotor blade to rotor disk (blade/disk) attachment methods for an air-cooled turbine rotor in a small gas turbine engine. This investigation was launched because the combination of factors that are necessary to satisfy the design requirements of a small cooled gas turbine has made it increasingly difficult to utilize conventional blade attachment means. Specifically, the program was directed toward achieving a suitable attachment method for an axial turbine with an inlet temperature of 2400°F, an airflow rate of 4.0 lb/sec, a tip speed of 1500 ft/sec, and matched to a compressor having a 10:1 pressure ratio.

Detail aerothermodynamic design activities were conducted to determine a turbine design that would provide optimum specific fuel consumption (SFC) and specific horsepower (sp hp). The design included an optimization study to obtain the best compromise of turbine efficiency, cooling geometry, blade and disk stress effects, and fabrication considerations.

Detailed mechanical design activities were conducted in parallel with fabrication technology development efforts to establish the materials, designs, joining methods, and fabrication techniques necessary to determine feasible means of blade disk attachment. Results of these activities showed that diffusion-bonding, brazing, and electron-beam-welding blade/disk attachment methods possess the greatest potential for application in the subject turbine design.

A secondary purpose of the mechanical design and fabrication development activities was to study the feasibility of developing the strut-supported sheet metal blade (shell/strut attachment) that was revealed by the aerodynamic optimization study to be the most effective blade cooling configuration. Full evaluation of the shell/strut attachment was beyond the scope of this program; however, it was determined that both diffusion-bonding and cast-bonding concepts of joining could be considered as feasible methods to develop for the purpose of shell/strut attachment.

A final fabrication and test activity was conducted to complete evaluations of the three blade/disk attachment methods. Final specimens were designed, fabricated, inspected, and subjected to tensile, stress-rupture, and low-cycle fatigue testing at 1200°F.

Evaluation of the final specimen test results revealed that (a) the diffusion-bonding method of joining was unsatisfactory for blade/disk attachment due to insufficient joint strength, (b) the brazing method of joining produced a joint strength approaching design requirements and could be considered as a candidate method for rotational test evaluation, and (c) the electron-beam-welding method of joining produced a joint strength that exceeded design requirements. Further evaluation will be necessary to resolve microcracking in the weld joint before rotational test evaluations can be considered.

DD FORM **1473** NOV 68 REPLACES DD FORM 1473, 1 JAN 64, WHICH IS OBSOLETE FOR ARMY USE.

14. KEY WORDS	LINK A		LINK B		LINK C	
	ROLE	WT	ROLE	WT	ROLE	WT
Turbine Blade/Disk Attachment Brazing Diffusion Bonding Electron-Beam Welding Sheet Metal Blade/Strut Attachment Cast Bonding						